Glass-free lightweight PV building elements: solutions to minimize weight and maximize durability

Thèse N° 9149

ANA CRISTINA OLIVEIRA MARTINS

2019

ÉCOLE POLYTECHNIQUE
FÉDÉRALE DE LAUSANNE

Abstract

In densely populated countries, little free land is available for the deployment of photovoltaics (PV) in field installations. In addition, 40% of the world's demand for electricity is related to buildings. These facts provide a strong argument for the accelerated development of building-integrated PV (BIPV), as it enables electricity production with a minimal impact on free land. However, BIPV elements currently on the market show some limitations, which includes their relatively high prices, as most products are custom-made and produced in small volumes. Moreover, the relatively high weight ($\approx$ 15–20 kg/m^2) of these products may preclude their use in the potentially promising market of renovations of older buildings, for which excessive load could be a serious constraint.

With the aim of limiting the module weight while preserving excellent mechanical stability and durability, we demonstrate that, with careful material selection and a proper adaptation of the manufacturing processes, we are able to manufacture lightweight modules with a weight of $\leq$ 6 kg/m^2. The weight reduction is achieved by replacing the backsheet, conventionally glass or polymer, with a rigid composite sandwich structure and by replacing the front cover glass with a thin polymer foil. In our approach, the conventional liquid epoxy used to glue skins and core is substituted with a thermoplastic adhesive foil (polyolefin) that ensures a good adhesion and stress transfer between the sandwich components. By associating this adhesive with a high-thermal-conductivity honeycomb core (aluminum), we can employ conventional lamination processes used in the PV industry to manufacture the backsheet and the full solar module stack simultaneously during a single process. These modules show an excellent resistance and stability when subjected to mechanical, climatic and electrical stress tests used in the solar industry. In fact, these solutions show a reduced power loss ($\leq$-5%), no major visual changes and preserve a good insulation resistance. These results demonstrate the potential of our design to successfully comply with the relevant PV qualification standards (e.g. *IEC 61215*).

We further demonstrate that our lightweight modules can successfully pass hail tests without cracked cells by tuning the mechanical properties of the frontsheet and backsheet simultaneously. The design of the lightweight PV modules is successfully scaled up to a sixteen-cell 0.81×0.81 m^2 module.

Abstract

Furthermore, the BIPV elements need to comply not only with PV standards but also with construction and safety standards, e.g. fire resistance. Preliminary results indicate that the proposed design in this thesis may successfully pass the relevant fire tests used for building elements (*CEN/TS 1187*). These first results also give indications on how to optimize the product further.

Finally, to reach a commercial market, some challenges must still be addressed: we must scale up to standard module sizes (1.6 m^2), and we must develop an ideal mounting solution for a good integration of the modules into the building.

Key words: Renewable energy; Solar energy; Photovoltaics; Solar module; Building-integrated photovoltaics (BIPV); Solar cell; Reliability; Accelerated-aging test; Failure modes; Lightweight; Composite sandwich structures; Skins; Honeycomb core; Adhesive; Bending stiffness; Young's modulus

Résumé

Dans pays densément peuplés, l'espace au sol disponible ne permet pas d'envisager de grandes centrales de production photovoltaïque (PV). De plus, 40% de la demande mondiale en électricité est liée à la consommation des bâtiments. Ces faits fournissent un argument solid pour le développement des solutions PV directement intégrées au bâtiments (BIPV), car il permet la production d'électricité avec un impact minimal sur l'espace au sol. Certains éléments existent déjà sur le marché, mais ils présentent encore de limitations, notamment au niveau du prix, trop élevé, la plupart des produits étant fabriqués sur mesure et en petite volume. De plus, le poids relativement élevé ($\approx$ 15–20 kg/m^2) des produits existantes pourrait leur barrer l'accès au marché, potentiellement prometteur, de la rénovation de bâtiments anciens, en raison de contraintes sur la charge admissible.

Pour réduire le poids des modules tout en conservant d'excellentes propriétés de stabilité mécanique et de durabilité, nous démontrons qu'une sélection rigoureuse des matériaux et l'adaptation des méthodes de fabrication sont exigées. Dans le cadre de ce travail, des modules légers ≤ 6 kg/m^2 ont ainsi pu être développés. La réduction de poids est obtenue en remplaçant la feuille arrière, traditionnellement en verre ou en polymère, par une structure sandwich composite rigide et en remplaçant le verre avant par une mince feuille de polymère. Dans notre approche, l'époxy liquide normalement utilisée pour l'adhérence des différentes couches du sandwich est remplacée par une feuille adhésive thermoplastique rigide (polyoléfine) assurant une bonne adhésion et un bon transfert des contraintes. En associant cet adhésif à un cœur en nid d'abeille de haute conductivité thermique (aluminium), nous pouvons utiliser les processus de fabrication PV classiques pour fabriquer des modules légers en une seul étape. Les modules ainsi conçus présentent une résistance et une stabilité excellentes lorsqu'ils sont soumis aux tests de contrainte mécanique, climatique et électrique utilisés dans l'industrie solaire. Ils affichant en effet une perte de puissance minime (≤-5%), aucune modification visuelle majeure et une bonne isolation électrique. Ces résultats très prometteurs ouvrent la voie à une possible certification des modules au regard des normes de qualification en vigueur dans l'industrie PV (par exemple, la *IEC 61215*).

Nous démontrons, en outre, que les modules ultra-légers développés peuvent satisfaire les tests de grêle, avec aucune cellule solaire fissurée, en optimisant simultanément la rigidité des

couches arrière et avant. Des modules ultra-légers de seize cellules ont ainsi été développés, représentant une taille de 0.81×0.81 m^2.

Il faut néanmoins signaler que les éléments BIPV doivent non seulement satisfaire l'ensemble des normes pour le PV mais également certaines normes de construction et de sécurité, par exemple celles liés à la résistance au feu. Or, nos résultats préliminaires indiquent que le design original proposé dans cette thèse est également adéquat pour satisfaire les tests au feu utilisés pour les éléments de construction (*CEN/TS 1187*). De plus, ces premiers résultats fournissent des indications très utiles sur la manière d'optimiser davantage le produit.

Finalement, en vue de l'exploitation commerciale, certains défis doivent encore être résolus : une accroissement de la taille pour atteindre celle des modules standards (1.6 m^2) et le développement d'un système de fixation dédié pour une parfaite intégration au bâtiment.

Mots clefs : Énergie renouvelables ; Énergie solaire ; Photovoltaïque ; Module solaire ; Photovoltaïque intégré au bâtiment (BIPV) ; Cellule solaire ; Fiabilité ; Test de vieillissement accélérés ; Léger ; Structure sandwich composite ; Peau ; Cœur en nid d'abeilles ; Adhésif ; Rigidité de flexion ; Module de Young

Contents

Contents

Contents

List of abbreviations and symbols

Symbol	Definition	Unit
A	Cross sectional area	mm^2
B	Width of sample	mm
CTE	Coefficient of thermal expansion	°K^{-1}
d	Distance between centroids of the sandwich faces t_f+t_c	mm
D	Bending stiffness of a sandwich beam	N·m^2
e	Position of the neutral axis	mm
E	Young's modulus	N/mm^2
E_c	Young's modulus of sandwich core	N/mm^2
E_f	Young's modulus of sandwich skin	N/mm^2
E_{eq}	Equivalent Young's modulus of a sandwich beam	N/mm^2
$E*$	Complex modulus in bending	N/mm^2
E'	Storage modulus in bending	N/mm^2
E''	Loss modulus in bending	N/mm^2
F_{max}	Maximum load applied	N
FF	Fill factor	%
$G*$	Complex modulus in shear	N/mm^2
G'	Storage modulus in shear	N/mm^2
G''	Loss modulus in shear	N/mm^2
G_c	Shear modulus of the sandwich core	N/mm^2
h	Distance from neutral axis of the skin to surface of the skin	mm
I	Current	A
I_{sc}	Short circuit current	A
$I_{inertia}$	Inertia momentum	m^4
L_1	Span between inner loading points in four-point bending	mm
L_2	Span between outer loading points in four-point bending	mm

Contents

M	Bending momentum	$N \cdot mm$
p	Pressure	Pa
P	Applied load	N
P_y	Yield load	N
P_{max}	Maximum power point	W
P_s	Peel strength	N/cm
P_Y	Yield Load	N
R_s	Series resistance	$\Omega \cdot cm^2$
R_{sh}	Shunt resistance	$\Omega \cdot cm^2$
S	Shear stiffness of a sandwich beam	N
t	Time	s
t_c	Thickness of sandwich core	mm
t_f	Thickness of sandwich skin	mm
t_{th}	Thickness	mm
T	Temperature	°C
T_{cell}	Cell temperature	°C
T_g	Glass transition temperature	°C
T_m	Melting temperature	°C
T_{module}	Module temperature	°C
V	Voltage	V
V_{oc}	Open circuit voltage	V
X	Degree of cross-linking	%
w	Weight	kg/m^2
δ	Load point displacement	mm
δ_{comsol}	Module deflection simulated in comsol	mm
δ_{ML}	Module deflection measured in ML	mm
ΔP_{loss}	Power loss variation	%
ΔT	Temperature gradient	°C
γ_{lv}	Surface tension of liquid / vapor interface	N/m
γ_{sl}	Surface tension of solid / liquid interface	N/m
γ_{sv}	Surface tension of solid / vapor interface	N/m
η	Efficiency	%
λ	Wavelength	nm
ν	Poisson's ratio	
θ_{cur}	Angle of curvature radius measured in ML	°
θ	Contact angle	°
ρ	Density	kg/m^3
σ_{UTS}	Ultimate tensile strength	N/mm^2

Abbreviation	Definition
Al-BSF	Aluminum-back surface field

ALT	Accelerated-life test
BAPV	Building-applied photovoltaic
BIPV	Building-integrated photovoltaic
CLT	Classic laminate theory
c-Si	Crystalline-silicon
DH	Damp heat
DMA	Dynamic mechanical analysis
DSC	Differential scanning calorimetry
EL	Electroluminescence
EVA	Ethylene-vinyl acetate
FEM	Finite element modeling
FTIR	Fourier transform infrared spectroscopy
GFRP	Glass-fiber-reinforced polymer
HF	Humidity freeze
HT	Hail test
IEC	International Electrotechnical Commission
I-V	Current-voltage measurement
LVDT	Linear variable differential transformer
ML	Mechanical load
Na^+	Sodium ions
OT	Operating temperature
P_1	Position of sensor closer to the laminator's heating plate
P_2	Position of sensor far from the laminator's heating plate
PERC	Passivated emitter and rear cell
PET	Polyethylene terephthalate
PID	Potential-induced degradation
PMMA	Poly(methyl methacrylate)
PO	Polyolefin
PV	Photovoltaics
STC	Standard test conditions
TC	Thermal cycling
UD	Unidirectional
YI	Yellowness index

1 Introduction

Summary

The focus of the thesis is to study the challenges of designing lightweight photovoltaic (PV) modules based on crystalline-silicon technology, focusing on applications in the field of building-integrated photovoltaics (BIPV). This chapter starts by giving an overview of the market status of PV/BIPV and the potential of BIPV to become a key ingredient in the electricity generation mix. Then, it presents the state-of-the-art of module technology, processing and reliability issues. Finally, it presents the outline of this thesis and its main contributions to the field of long-term performance of lightweight PV modules.

1.1 Solar energy

1.1.1 Current status of solar photovoltaic energy

Global energy demand is continuously increasing [1]. In 2017, it grew by 2.1%, more than twice the growth rate in 2016, while energy-related CO_2 emissions rose by 1.4%, raising concerns about the world's ability to meet the goals of the Paris Agreement of 2015 on climate change [2].

Renewable energies are the key to offer energy with reduced environmental and health impacts. Solar power generation is one of the major energy sources of the renewable energy portfolio. Besides producing electricity, solar represents a sustainable carbon-free energy source that can slow down the pace of climate change and prevent further damage to the environment. PV technology is a unique and highly promising option that directly converts the incident energy from the Sun into electricity. From the 86×10^6 GW of power received by Earth from the Sun [3, 4], only one hour is needed to meet the annual energy needs of all people worldwide.

PV technology is the renewable energy that has, in particular, experienced the fastest growth in the last few decades. According to the International Energy Agency, the cumulative PV capacity has increased globally from 1.4 GW in 2000 to 400 GW in 2017 [5], with a record of 98 GW of newly added PV capacity in 2017. This fast market growth has happened mainly thanks to advances in technology (e.g., increased solar cell efficiencies), supportive policies [2] and a steady reduction of PV module costs [5]. Indeed, figure 1.1 shows the average PV module cost at an impressive level of 0.34 $/Wp in 2017 (dropping by approximately 80% since 2009). In addition to utility-scale ground-mounted solar farms, rooftop installations on residential, commercial, and industrial buildings constitute a significant part of solar electricity generation.
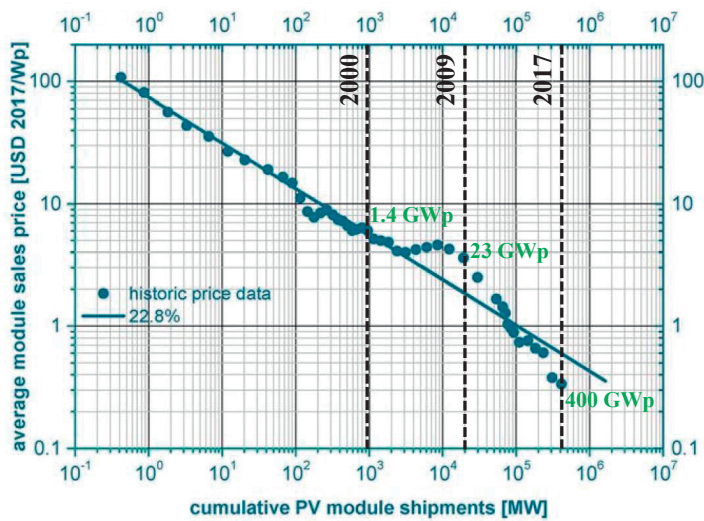
Figure 1.1 – Learning curve for module price as a function of cumulative shipments with reference to global cumulative PV capacity in 2000, 2009 and 2017 (figure adapted from [5]).

1.1.2 Photovoltaics in buildings: market status

Cities are responsible for generating 70% of greenhouse gas emissions [6]. Solar energy could positively contribute to their reduction. In several countries, only a few sites are available for large-scale field PV installations and the lack of availability of free land may constitute a bottleneck for the diffusion of solar electricity. Applying PV to buildings (see figure 1.2a) offers useful alternative, since more than one third of worldwide final energy consumption is attributed to buildings [7, 8]. For example, in countries like Switzerland already ≥ 98% of solar installations are installed in the built environment, and studies indicate that the use of well-oriented roofs and façades has the potential to meet up to 30% of the Swiss annual electricity demand (20 TWh) [9]. However, in urban environments, most PV installations are added to an existing roof, the so-called **building-added PV (BAPV)**. For aesthetic reasons, the use of BAPV in the urban environment is still controversial [10, 11].

(a) Traditional BAPV roof installation   (b) Partial BIPV installation
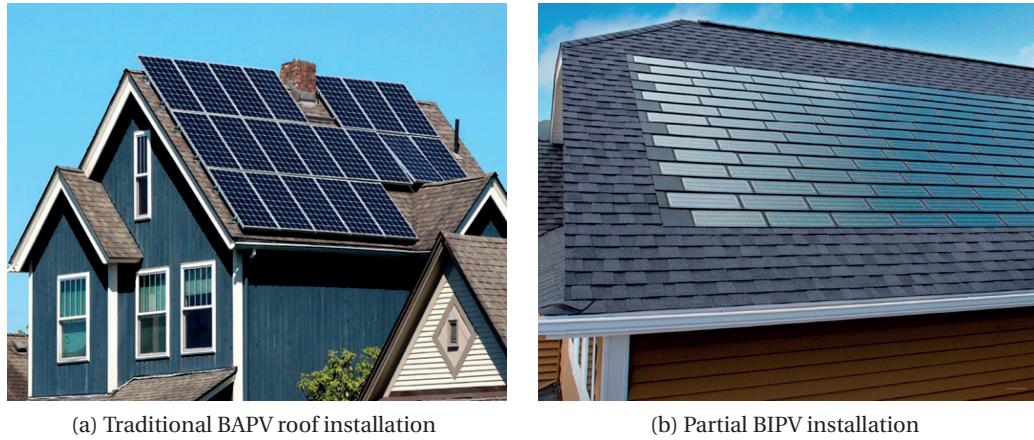
Figure 1.2 – Examples of (a) a typical building-added PV (BAPV) installation and (b) a partial roof building-integrated PV (BIPV) installation. Both cases use monocrystalline silicon solar cells laminated in a standard glass-backsheet configuration (figures taken from [12]).

Building-integrated photovoltaics (BIPV) can redefine the PV module as an architecturally relevant building component with an active energy-producing unit that also adds aesthetic value to the whole construction. The first BIPV elements were introduced at the end of the 1980s. However, at that time, BIPV was limited to rooftop integrations of relatively conventional PV modules. Figure 1.2b shows an example of standard BIPV integration based on crystalline silicon (c-Si) modules using a glass-backsheet configuration. BIPV solutions have improved for monocrystalline or multicrystalline silicon modules with a homogenized black appearance or modified cell color and thin-film modules that can provide some level of transparency [10, 13]. For a long time these products were seen as non-aesthetic solutions with low flexibility in design, not satisfying the needs of architects or builders.

In recent years, exemplary demonstration projects have been realized and exhibited the high potential of BIPV elements. As an example, figure 1.3a shows a full BIPV roof installed on a historical building situated in a protected zone by the Federal Inventory of Swiss Heritage Sites (ISOS), using PV modules composed of black monocrystalline silicon solar cells and special-sized dummy modules to ensure full roof coverage. Another impressive demonstration project, shown in figure 1.3b, is a 70 kWp façade integration composed of semi-transparent bifacial modules using c-Si heterojunction solar cells connected with SmartWire Technology [14]. Such projects highlight the double nature of BIPV solutions as electricity generators and construction material elements that have the potential to reach per-meter-square costs in the range of the materials they are substituted for [15]. Indeed, a study of the prices of PV rooftop systems in the residential sector undertaken by the National Renewable Energy Laboratory (NREL) demonstrated that the multifunctional features of BIPV elements offer a promising return on investment: BIPV has the potential to achieve system prices that are about 10% lower than rack-mounted PV systems, mainly due to the elimination of the cost of the hardware and the associated labor costs [16].

(a) Full-roof PV integration in a historical building   (b) Façade PV installation

Figure 1.3 – Examples of BIPV demonstration projects: (a) the full-roof renovation of a historical building using monocrystalline silicon modules (Switzerland) and (b) a façade installation at the Swiss Center for Electronics and Microelectronics (CSEM) using glass-glass modules with c-Si heterojunction bifacial modules (pictures adapted from [15]).

Today, thanks to the impressive reduction of c-Si solar cell costs and improvements in PV module reliability, many BIPV examples can be found all over the world, for example: the Stadtwerke Konstanz Customer Center (Konstanz, Germany), the Heron Tower (London, UK), the Roman Catholic Parish (Basel, Switzerland), the Tobias Grau Lightning (Hamburg, Germany), the Böwe CardTec building (Paderborn, Germany), the Historical Building in Affoltern (Affoltern, Switzerland) or the Xicui Entertainment Complex (Beijing, China). The largest part of these solutions is composed of c-Si solar cells embedded in a glass-glass configuration. Researchers have been continuously working on improving BIPV aesthetics by masking the interconnection between solar cells, by changing module color through adding coatings on the glass (inside or outside) to create homogeneous color effects [17] (figure 1.4a), and by developing films that can hide the cells while still allowing them to act as electrical energy generators. The white module from Solaxess[1] is an example of these BIPV aesthetic solutions: these modules absorb in the infrared spectral range to generate electricity and reflect the visible light to create a white appearance which is very attractive for façade installations. Thanks to all this technological progress, it is even possible today to include different images in the modules in low or high resolution [18] (figure 1.4b).

In the coming years, BIPV installations are expected to meet more than 22% of the expected 2030 electricity demand [7] mainly thanks to the adoption in several countries of new energy-efficiency codes, the high demand for renewable energy, and the "green building" movement in the construction sector. The *Energy Performance of Buildings Directive (EPBD)* [19] requires that all new buildings in Europe comply with the Nearly Zero-Energy Building standard by December 31st, 2020, which stipulates that the energy consumption of a building must be covered by renewable energy produced on-site [20]. This directive favors the direct integra-

---

[1]Company website: www.solaxess.ch/

(a) Colored BIPV modules based on front glass coating

(b) A high-resolution colorized BIPV module
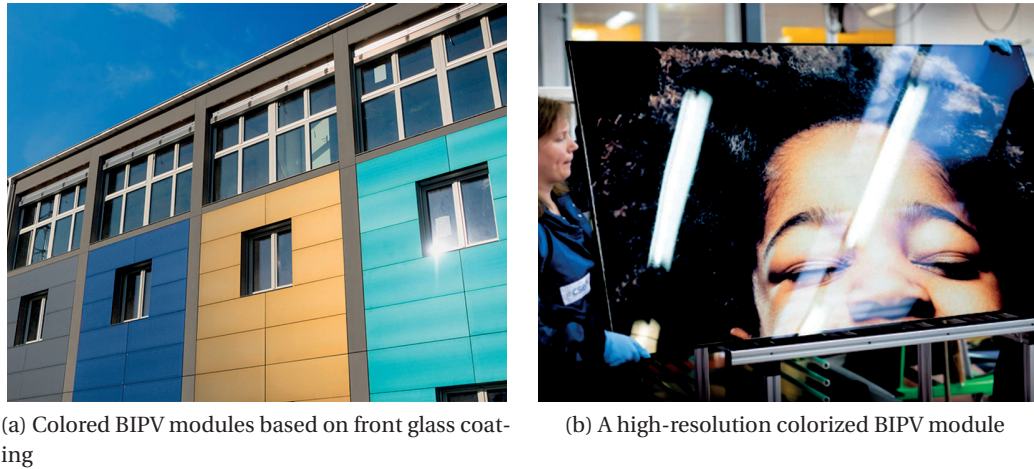
Figure 1.4 – Building-integrated elements with improved aesthetics: (a) colorful façade that uses glass-coating technology and (b) a BIPV panel that includes a high-resolution image. Both BIPV elements use c-Si solar cells (pictures taken from [18, 21]).

tion of decentralized energy sources in buildings, among which BIPV appears to be the most promising one [15].

BIPV limitations

One technical constraint of BIPV modules is the absence or non-uniformity of building codes and standards from country to country. Many researchers have thus been focusing on new regulations and building codes and, recently, a European norm was published, *EN 50583-1: PV in buildings - Part 1: BIPV modules* [22]. This norm addresses which codes from both building construction and electrical devices must be applied. However, this norm does not speak about performance or durability tests regarding the electricity production of a BIPV module, it does not consider whether the higher temperatures experienced by BIPV elements require different testing levels, and it still contains many references to "national requirements".

Another limitation is the fact that builders and architects are still not aware of the advantages of this type of technology and thus barely consider PV when designing new projects [15, 23]. Indeed, BIPV solutions are often considered at the end of a building's design or renovation. Most of the BIPV products currently on the market are based on standard c-Si module architectures, which have the drawback of a high weight due to the presence of one or several glass sheets [24, 25]. This conventional design satisfies many solar consumers' needs; however, for buildings with weight constraints and a high supply-chain cost, lightweight modules may be preferable. Table 1.1 shows standard module weights for c-Si modules. The high weight puts constraints on the building envelope and on the supporting structure, resulting in increased balance-of-system (BOS) costs and installation limitations, especially in the case of building refurbishment.

Table 1.1 – Typical module weights for c-Si PV modules in three configurations: standard glass-backsheet, glass-glass, and special glass-glass for BIPV applications [24, 26].

Module layup	Weight, w [kg/m^2]
Glass-Backsheet	12 – 16
Glass-Glass	14 – 17
Glass-Glass for BIPV	≥ 20

1.2   Lightweight PV modules

Often, particularly in the case of older buildings undergoing renovation, excessive loads are not well tolerated by roofs or other building structures [25, 27, 28]. In these cases, inclusion of traditional PV modules is abandoned. The idea of lightweight modules is very attractive and could favorably cover all these old buildings undergoing renovation. Moreover, these lightweight PV products can easily fit other industries, such as the marine and mobility industry (boats, car roofs, caravans) or the aerospace industry (planes, satellites). Because they are easily carried, they can even be attached to unusual places (tents, laptops, backpacks). Indeed, lightweight PV modules can be seen as portable devices, easily transported to remote areas, post-disaster or reconstruction scenarios (cases where electricity does not exist, e.g. due to natural disasters). In such applications, current PV modules cannot satisfy those needs due to their relative weight, complex transportation and the high risk of glass breakage. Having a lightweight unbreakable solution will increase the number of buildings or places that can receive PV modules, and reduce the installation cost and labor.

However, one of the challenges of lightweight PV module design is the questionable module resistance to environmental stress: a new structure design means that the durability and long-term performance are unknown, which results in market uncertainty. The issues of weight and durability are the focus of this thesis.

1.3   Photovoltaic modules

PV modules are made from a series of electrically interconnected solar cells sandwiched in a multilayer structure that provides mechanical and environmental stability against external elements [29]. Based on the manufacturing technology and on the absorber material used, PV modules are commonly classified into two major groups: c-Si modules and thin-film modules. PV modules based on c-Si are the most widespread technology, with up to 93% of the market share from the total PV installed capacity in 2017 [30]. Therefore, this thesis focuses on modules produced with this type of technology.

1.3.1 Structure of standard PV modules

Crystalline-silicon PV modules usually consist of a group of solar cells connected to form a string, which are then embedded in an encapsulating polymer foil that bonds them to the front and back cover layers. Figure 1.5 presents the most common PV module structure.
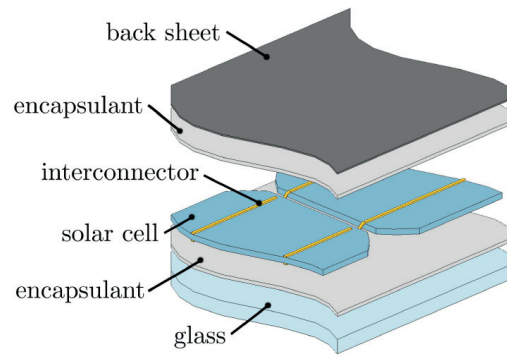
Figure 1.5 – The most common PV module structure for wafer-based c-Si modules: the glass-backsheet structure (figure taken from [31]).

The PV module capacity to convert direct energy from photons to electrons is realized by the active component, the **solar cell**. c-Si solar cells are processed from silicon crystalline wafers. Their processing steps include etching, doping, texturing, screen-printing and firing. The operating principle of the solar cells is based on a doped semiconductor to form a p-n junction: (1) the semiconductor material absorbs light (photons) and (2) the p-n junction forms an internal electrical field that separates charges. This energy conversion is called the "photovoltaic effect". A detailed description of the electrical working principles on the cell and module levels is given in [32, 33].

The **interconnections** electrically connect the different solar cells to form a string. They are made of copper coated with soldering material, and are approximately 130 μm thick and 1–2 mm wide [34]. Depending on the cell design, three, four or five interconnectors are generally soldered to the front and back side busbars of the solar cell. There is a market trend towards a higher number of interconnections.

The PV **encapsulant** works as an adhesive to bond the different layers of a PV module. A good candidate for a PV encapsulant should provide a high optical transparency, good adhesion to the module components, adequate thermo-mechanical compliance to accommodate stress induced by differences in thermal expansion coefficients, moisture and electrical barrier properties, etc. [35, 36]. The most commonly used PV encapsulants are based on ethylene-vinyl acetate (EVA) [37]. Polyvinyl butyral (PVB) is also used in PV modules mainly for BIPV applications due to its excellent long-term resistance to UV light and temperature stability, and because it fulfills the relevant safety standards for laminated safety glass (i.e. glass-glass structures) [38]. There are other encapsulant materials that have historically been used, such as ionomer, silicon or polyolefin.

The **front cover** of PV modules is typically tempered glass due to its strength and safety. The standard glass thickness is 3.2 mm or 4 mm but it can be as thick as 6 mm for BIPV applications for safety and stability reasons. The glass must ensure good transparency in the relevant wavelength, provide mechanical rigidity and impact resistance, block moisture ingression and have good outdoor weather-ability [35].

The **back cover** of PV modules (normally called the backsheet) can be either a multi-polymer layer or a second glass sheet. The main functions of the back cover are to provide electrical insulation, environmental protection and structural support. The advantage of PV modules with a polymer backsheet compared to those with a glass rear is their lower weight.

1.3.2   Structure of lightweight PV modules

In standard PV configurations, 60–70% of the weight of a module comes from the glass. Therefore, the primary way to reduce the weight of a solar module is to replace the PV modules' frontsheet and backsheet materials with a lighter material. There are three main types of lightweight PV modules:

- **Flexible PV –** Modules without glass have already been the focus of several developments, especially in the field of mobility (boats [39], cars, and caravans [40]). The preferred option for weight reduction is to process a flexible PV module that is fully composed of polymers. These lightweight solutions have weights ranging from 2–3 kg/m^2. The drawback of these products is related to the long-term performance. Most are developed for transportation applications, and thus the manufacture generally proposes a limited product warranty of 5–10 years without any product compliance with relevant PV standards.

- **Semi-rigid PV –** These lightweight modules are usually composed of polymer materials reinforced with fibers, having weights ranging from 5–7 kg/m^2. These solutions are normally used for special applications such as satellites [41] or solar planes [42–44]. For such applications, semi-rigid PV modules are advantageous because they provide additional mechanical stability under very harsh conditions. Some manufacturers claim compliance with the relevant PV standards. However, these solutions show degradation in performance and mechanical stability when submitted to some accelerated-aging tests. More details can be found in Chapter 3.

- **Rigid PV –** These lightweight modules are normally produced in two steps: first a (semi-) flexible PV module is produced with a standard lamination process and, in an additional processing step, it is integrated with a light composite sandwich structure, widely used in several industries such as aeronautics [45–47] or construction [48–50]. The additional processing steps for these modules add to their cost and make them less competitive.

Lightweight PV modules based on glass-glass technology do exist as few companies propose a

reduction of glass thickness from the standard 3.2 mm to as thin as 0.8 mm, achieving a weight of 6.5 kg/m^2 [51]. However, the cost of ultra-thin glass contributes to a considerable increase in PV module cost. They are also more susceptible to cracks; thus the market penetration is still very low. Some other companies, such as Yingli Solar, have been working on reducing the weight of PV modules, and have received many patents [52–56]. However, no lightweight PV modules from these companies are exploited commercially. Oreski et al. [57] have shown that another way to reduce the PV module weight consists of reducing the encapsulation material's thickness while keeping the required functional properties. However, a change in PV encapsulant foil would contribute only a little to the reduction of PV module weight. In 2017 the company 2CA proposed a composite lightweight PV module with integrated PV connectors. This solution has a final weight of 3.8 kg/m^2 and a power output of 150 W/m^2. The company claims compliance with relevant PV standards but, as of today, their modules are not commercially available [58–60].

1.3.3 Lamination

A PV module is manufactured using a lamination process. Once the module assembly is ready, it is laminated in a flat-bed vacuum bag laminator. The laminator is divided into two chambers and separated by a flexible rubber membrane. The bottom chamber is composed of a homogeneous heating plate, which heats the PV module stack, and of metal pins that can be moved up or down from the heating plate to adjust the heating rate of the module [61, 62]. During the lamination process, temperature, pressure and time are controlled to have the ideal lamination profile (T-p-t profile). In a standard PV lamination profile there are three main stages that can be adjusted depending on the type of encapsulant and module stack used (as represented in figure 1.6):

- **Preheating –** the module lies on top of the metal pins. The main purpose of this stage is to remove the air bubbles between the frontsheet and backsheet and to slowly melt the encapsulant to avoid cracked solar cells during the curing step.

- **Curing –** In a second step, the pins are retracted and the module is in direct contact with the heating plate. At the same time, air is allowed to fill the upper chamber up to a maximum atmospheric pressure (1 atm), pressing the rubber membrane to the module. The purpose is to remove any remaining bubbles present in the encapsulant and to allow the encapsulant to form a bond between the different module components. The temperature of this step is normally selected based on the type of the encapsulant foil used.

- **Cooling –** In a last (optional) step, the laminate is transferred to a second chamber where cold water flows on the tubes below the plate. At the same time, a rubber membrane applies a pressure of 1 atm to ensure that there will be no warping of the module stack. The main purpose is to minimize bowing and to prevent edge delamination.
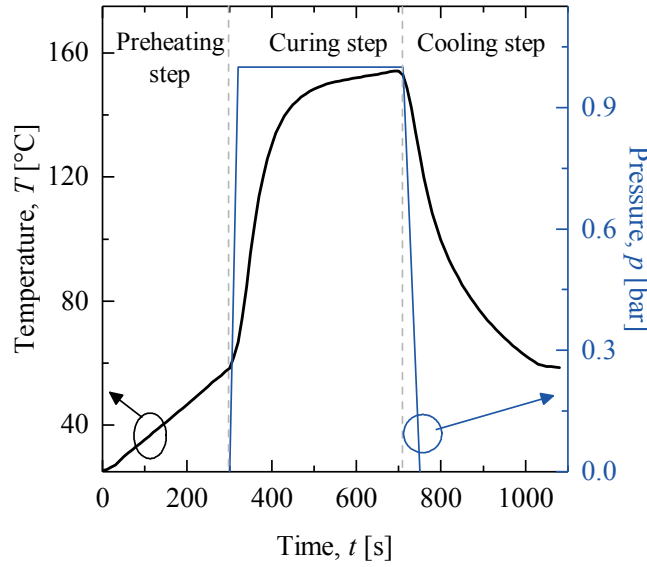
Figure 1.6 – Typical temperature-pressure-time (T-p-t) profile used in standard PV module lamination process. The figure shows the three different steps during a standard lamination process: preheating, curing, and cooling (optional).

1.4   Reliability of crystalline-silicon PV modules

Today's c-Si PV modules are sold with a double warranty that guarantees 90% of the nominal power for the first 10 years and 80% of the nominal power for 25 years of operation in the field. This warranty corresponds to an annual power degradation rate of 0.8%/year. The term "power degradation" corresponds to the decrease of the maximum power P_{max} (maximum power output of the module when measured at standard test conditions (STC)) with respect to the nominal power P_{nom} (initial maximum power of the module measured by the manufacturer). Today, some companies provide warranties that assume a linear degradation over time [63]. Module manufactures and researchers are continuously working towards even higher lifetimes to make PV power more cost-effective: the longer a module produces electricity in the field, the lower its cost per generated kWh. This warranty is given based on the reliability of PV modules.

Thanks to years of field installations and operations of PV plants in various climates, the PV community has gained considerable insights into the common failure modes of field-deployed PV modules [64, 65]. Figure 1.7 shows the more frequent failure modes appearing after long-term outdoor exposure, in which we can see that the dominant failure mode has changed over the years, as the technology has evolved. Different accelerated-aging tests are used as a feedback on module design stability under high stress. For c-Si PV modules, the set of qualification tests is proposed by the International Electrotechnical Commission (IEC) such as: *IEC 61215:2016 – Terrestrial PV modules-design qualification and type approval* [66] and *IEC 61730:2016 – PV module safety qualification: Requirements for construction* [67].
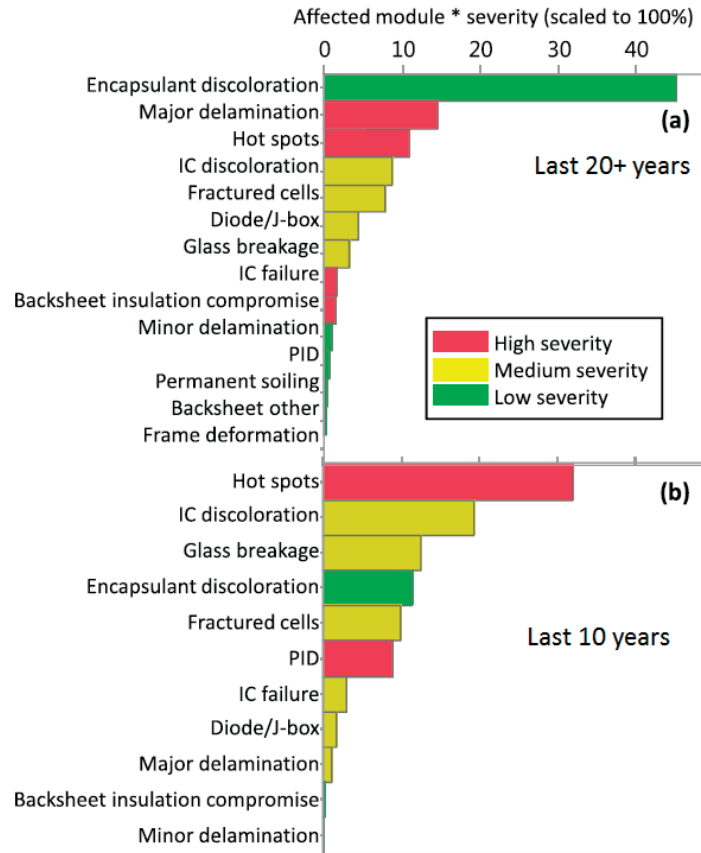
Figure 1.7 – Pareto chart of the most significant degradation modes for (a) systems installed more than 20 years ago and (b) systems installed in the last 10 years (Figure taken from [68]).

1.4.1 Common failure modes of BIPV modules

As previously mentioned, PV design has been driven by learning from the failure modes present in field installations. Up to now, BIPV installations have been limited to demonstration projects or recent installations; thus, information about failure is scarce and, in some cases, hidden by the manufacturers. The two main causes of fast degradation of BIPV are the high operating temperatures BIPV modules might experience due to reduced or absent back ventilation, and the high likelihood of hot spots due to shadows created by other buildings (especially in the case of façade integration).

Figure 1.8 shows examples of the main degradation modes of two BIPV installations in Switzerland and Italy after only a few years of installation (11–13 years) [69, 70]. In the case of the BIPV installation in Switzerland, the BIPV modules are composed of a glass-backsheet bonded to a roof tile, while the installation in Italy is composed of a glass-backsheet configuration mounted with clamps with an air gap of 10 cm. In both cases, the observed failure modes are: **(a) corrosion:** a strong surface pollution is visible due to the corrosion of the top solar tiles and cables (figure 1.8a); **(b) delamination**: the mini-solar module is bonded to the top

|(a) Tile corrosion|(b) Delamination|(c) Yellowing and delamination|
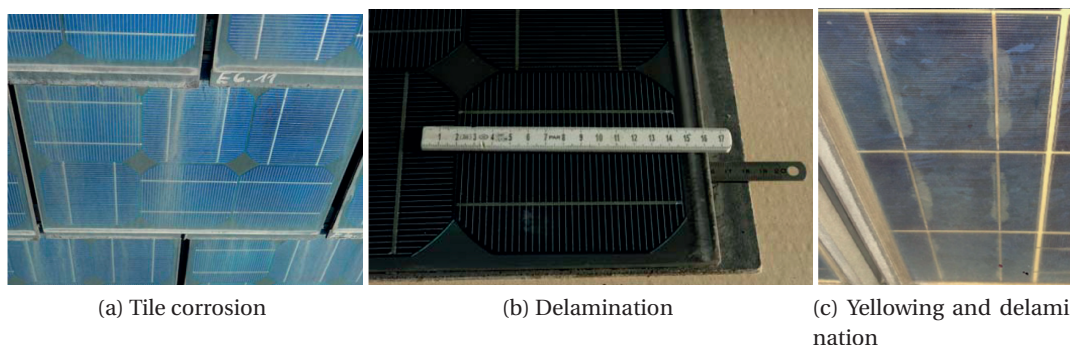
Figure 1.8 – Failure modes observed in three BIPV installations: (a) corrosion of tiles due to environmental influences, (b) delamination between the tiles and the solar module and (c) yellowing and delamination along busbar.

the roof tiles; however, over time, large gaps of up to 16 cm have opened between these two components (figure 1.8b); and **(c) yellowing**: all installed modules showed frontsheet and backsheet yellowing due to EVA degradation (figure 1.8c). Moreover, some modules also show a color change from yellow to brown.

In addition to failure modes similar to those of standard PV installations, BIPV modules normally see **higher operating temperatures (OT)** due to limited rear ventilation, meaning that the degradation can be further accelerated compared to standard PV modules. Nordmann et al. [71] analyze the rise of module temperatures (T_{module} - $T_{ambient}$) as a function of irradiation for different BIPV systems: a fully integrated PV system on the roof, a well-ventilated roof system, a façade installation with free airflow on the inside of the building and a façade with a narrow air gap between the module and the insulation. The author shows that the peak temperature can typically be 15 to 35°C higher for BIPV compared to well-ventilated systems. The losses averaged over one year that arise from higher temperatures will be in the range of 3 to 8% (figure 1.9). By comparison, the average operating temperature of a well-ventilated PV array in Switzerland is 35°C, which corresponds to an annual energy loss of less than 4%. Indeed, other authors point out that BIPV modules fully integrated into the building envelope with no ventilation from the rear side can reach operating temperatures as high as 86°C for a sunny summer day [72]. As stated by many authors [73, 74], the energy losses can be mitigated by adequate ventilation with a distance of 15 cm between the module and the building.

1.4.2 Accelerated-aging tests

In the PV industry, reliability refers to the ability of the PV module (or system) to perform as required, without failure, for a given time interval, under given conditions [75]. The long-term performance of PV modules is analyzed by applying accelerated-aging tests. The *IEC 61215* lays down requirements for the design qualification and type approval of PV modules suitable for long-term operation in general open-air climates. Figure 1.10 summarizes the different

Figure 1.9 – Overview of temperature losses and the rise in module temperature of well-integrated sloped roofs, façades, well-ventilated roofs and freestanding and flat roofs (figure taken from [71]).

test sequences proposed in [66]. It includes thermal stress tests (damp heat, thermal cycling, humidity freeze, UV preconditioning, and hot-spot tests) and mechanical tests (mechanical load and hail tests). Table 1.2 gives a short description of these tests with the description of the failure modes they aim to reproduce. This standard incorporates a strict "pass" or "fail" criterion which allows manufacturers to demonstrate the degree of performance [76]. A module is said to pass the qualification tests if:

- after each test sequence mentioned in figure 1.10, the maximum power output drop of each module (P_{max}) is less than 5%, in reference to the module's initial measured output power P_{max}. (In this work, when modules are submitted to single-shot tests or different test sequences, we consider the limit of -5% loss after each test, for the purpose of diagnosis)

- there is no visual evidence of major defects (yellowing, delamination, corrosion, bending).

- the insulation (dry) and wet leakage current test requirements are met at the beginning and at the end of each sequence.

These qualification tests are critical to identifying product design flaws that may show up in the field after several years. However, these tests have some limitations such as: (i) difficulty to correlate the output of accelerated-aging tests with the module's lifetime because the correlation between stress during the laboratory tests and in the field is weak; (ii) accelerated-aging tests are independent of climatic environments (the same module can show different degradation rates if installed in different climates) [77, 78]; (iii) modules might pass the predefined duration of an accelerated-aging test with similar power loss but show different degradation after this period [79]; and (iv) there are nearly no UV testing present in *IEC 61215*.
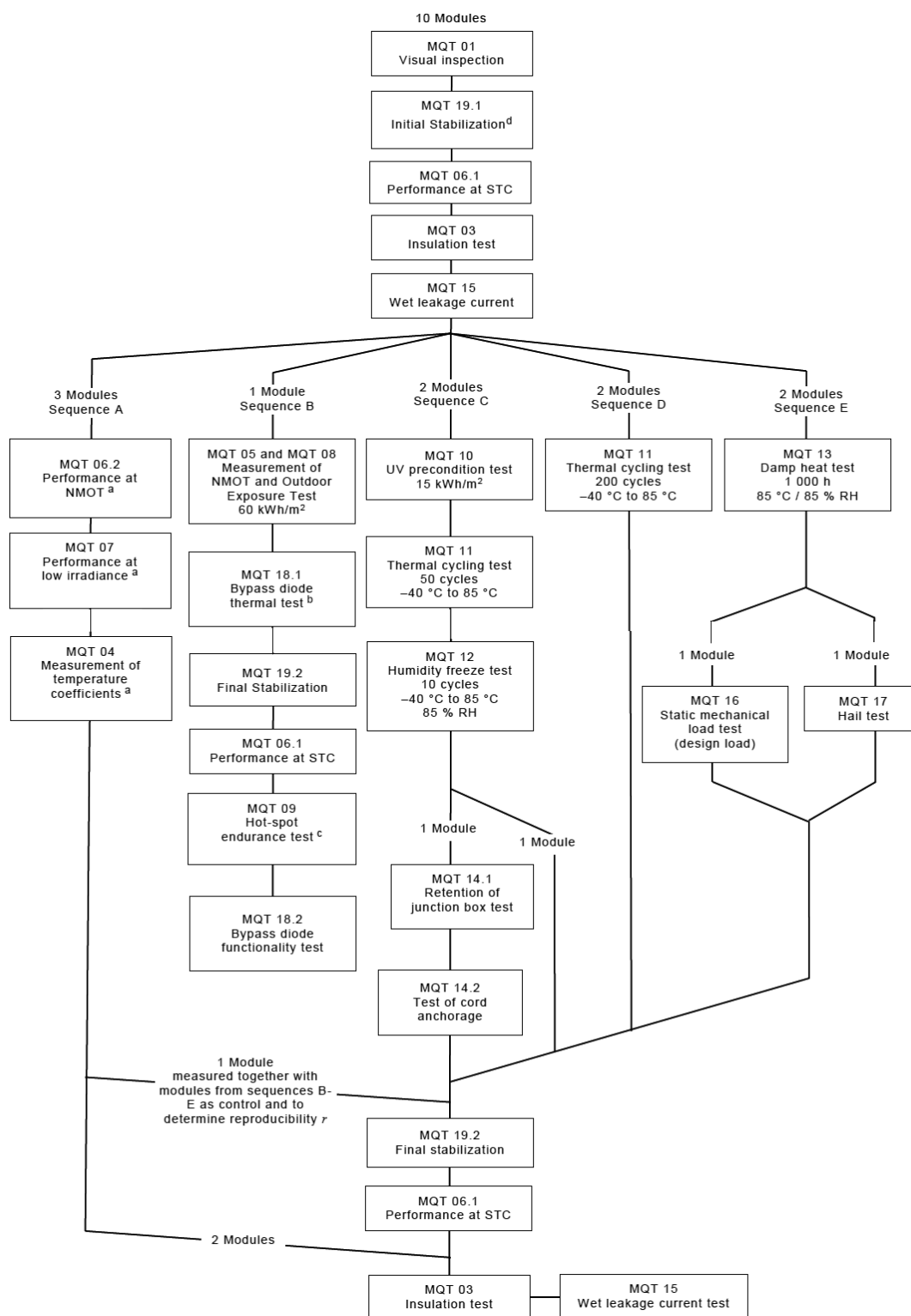
Figure 1.10 – Sequence of tests for module qualification as defined in *IEC 61215* [66].

Table 1.2 – Examples of the most-demanding aging tests contained in *IEC 61215:2016* and *IEC 62804:2015* with corresponding failure modes that each test aims to reproduce. More details can be found in [66, 80–85].

Aging test	Purpose/Description	Failure modes
Thermal Cycling	Determine module's ability to withstand thermal mismatch or fatigue: module is exposed to cyclic temperatures of 85 to -40°C for 200 cycles. For temperatures above 25°C, the module maximum current flows through the module.	Broken interconnections, cell breakage, solder bonding failure, junction box adhesion, delamination, junction box failure
Damp heat	Verify module's ability to survive the effect of long-term penetration of humidity: module is exposed to a temperature of 85°C and a relative humidity of 85% for a period of 1000 h.	Delamination, corrosion, encapsulant discoloration, solder bonding failure, snail trails
Humidity freeze	Evaluate module's resistance to the effect of high temperature and humidity followed by sub-zero temperatures: module is subjected to temperatures cycling between 85°C with relative humidity of 85% and -40°C. During the tests the module has a continuous current flow of ≤0,5% of the measured current under standard test conditions.	Delamination, cell breakage, junction box failure, solder bonding failure
Mechanical Load	Determine module's ability to withstand wind, snow, static or ice loads: module is loaded on the front side with 2400/5400 Pa for 1h and afterward with -2400/-5400 Pa for another 1h. This sequence is repeated three times.	Structural failures, glass damage, broken interconnections, cell breakage, solder bonding failure
Hail test	Verify module's ability to withstand the impact of hail: module is shot in several positions with ice balls with diameters of 25–75 mm at specific velocities (23–39.5 m/s).	Cell breakage, glass damage
UV pre conditioning	Evaluate components that are susceptible to UV degradation: modules are placed in a chamber at (60 ± 5)°C and illuminated by a UV light source within the wavelength ranges of 280–400 nm, not exceeding 250 W/m^2 and a percentage in the range of 3–10% of UV between 280–320nm. A total dose of 15 kWh/m^2 must be administrated.	Encapsulant and backsheet discoloration, delamination
Potential-induced degradation	Analyze module's resistance against PID: module is subject to 60°C, 85% RH in a climatic chamber with a voltage of -1000 V applied between the cells' circuit and the grounded frame for 96 h.	potential induced degradation, corrosion of the electrical connections

Correlation between indoor accelerated-aging tests and outdoor exposure: lifetime prediction

In the last few years, researchers started to address the issue of correlation between indoor accelerated-aging tests and outdoor prediction. A lot of effort is aimed at developing comparative and lifetime tests in the assessment of module reliability. These tests aim at predicting

performance in the long term, providing an absolute quantification of a module's lifetime. To reach this goal, different test protocols are being developed, e.g., Annigoni [86] proposes an indoor test sequence that, when performed in combination with a mathematical model and a simulation procedure, allows for the prediction of the PID effect on the electricity production of a module in the long-term. The same principle must be applied to lifetime prediction of BIPV modules. In an outdoor environment, a BIPV module will experience a higher operating temperature than a BAPV module. This might more quickly induce failure modes that are accelerated by temperature (e.g. backsheet cracking, delamination, hot spots, breakage of interconnection, etc.). Until now, PV modules from both types of installations (BAPV and BIPV) are tested under similar accelerated-aging tests, ignoring the future outdoor installation type and the maximum operating temperature modules might reach. In order to predict the lifetime of BIPV modules, the main failure mechanism must be identified and a new indoor test sequence must be developed to reproduce failure modes observed in the field and to extract degradation rates (e.g. identify activation energy from indoor tests, if degradation follows an Arrhenius dependency). This will help researchers to find mathematical models that can be used to predict the evolution of the module's power according to the module's operating temperature. A proposed sequence methodology is presented in Chapter 9.

1.5   Objectives and structure

1.5.1   Motivation and goal of this work

The conventional glass-glass BIPV design satisfies many solar consumers' needs. However, these solutions usually present a high price or constraints that have, for the moment, limited the deployment of PV into buildings as expected some years ago. This thesis focuses on the operational strategies to overcome technical obstacles towards large-scale BIPV integration into the urban renewal process. One of the obstacles identified includes the relative high weight of BIPV solutions, the complex manufacturing process of lightweight PV elements and their lack of aesthetics and long-term performance.

In this context, the global goals of this thesis are twofold:

- To identify and analyze the major limitations of current lightweight PV elements by proposing dedicated sets of characterization and test sequences. The objective is to understand the materials' constraints and interactions that can lead to failure. To fulfill this goal, we focus initially on the fundamental properties of the various materials composing the PV module (frontsheet, encapsulant, solar cell, backsheet). Modules on the market are then analyzed and tested in detail in order to gain insights into ways to improve the design of lightweight BIPV elements.

- To propose novel module designs for both easier implementation into building and long lifetime, with a focus on lightweight panels (targeting a weight of ≤6 kg/m^2). The proposed lightweight PV elements must be manufactured in a single lamination process

using standard lamination tools in order to be easily adapted to any existing manufacturing tools and to use as many materials used by the PV industry as possible. This will allow a simplification of the manufacturing while reducing manufacturing time.

1.5.2 Structure

Following this introductory chapter on the topic of reliability of BIPV and lightweight PV modules, this thesis is structured as follows:

- **Chapter 2** presents a short description of materials and experimental techniques used in this thesis. This chapter includes the description of materials selected for the development of lightweight PV modules, the experimental methods used for material characterization and finally the description of setups used to characterize the electrical performance of the module.

- **Chapter 3** presents an aging study performed on a set of commercially available lightweight solutions. This chapter also identifies their typical failure modes and the main materials used in their fabrication.

- **Chapter 4** gives a theoretical introduction to composite sandwich structures considered for the design of lightweight modules. This chapter also shows the sandwich properties and failure modes that must be known during the design of modules.

- **Chapter 5** shows the manufacturing process of lightweight PV modules and how a standard PV lamination process can be optimized when new materials or designs are used. This chapter also identifies the key properties that must be controlled during the manufacturing process optimization (adhesion, adhesive viscosity, cross-linking).

- **Chapter 6** is dedicated to the reliability study of our glass-free lightweight PV modules. This module design is tested under the most challenging thermal stress tests such as thermal cycling, damp heat, potential-induced degradation and humidity freeze tests. This chapter also shows the scale-up process from two-cell modules to sixteen-cell modules.

- **Chapter 7** shows how lightweight PV modules can be optimized to successfully pass mechanical stress tests, specifically point impacts and uniform loads. Furthermore, the response of the lightweight PV modules to the hail test and static mechanical load is discussed.

- **Chapter 8** shows that the proposed lightweight modules are also compliant with some demanding tests present in building and safety standards (*ISO 12543* and *CEN/TS 1187:2012*). It also shows the optimization of their appearance and their mounting systems.

- **Chapter 9** presents general conclusions of the outcomes of this thesis and proposes an outlook to future developments.

1.5.3 Contribution to the research field

This thesis contributes to the research field of the long-term performance of lightweight PV modules and encapsulation processes as follows:

1. By studying the degradation mechanism of commercial lightweight PV modules, we demonstrate that these solutions show a reduced performance even when the manufacturer claims compliance to relevant IEC/UL standards. We report, for the first time, the main failure modes of lightweight PV modules along with the main materials used for their fabrication. At this stage, novel materials are proposed for the development of lightweight PV modules.

2. We propose a fast and simple PV manufacturing process for composite sandwich structures using a flat-bed vacuum bag laminator, keeping high stiffness and low weight. This manufacturing process is compatible with lamination guidelines already used within the PV industry. This is achieved by substituting the standard liquid thermoset adhesive with a thermoplastic adhesive foil, developed in-house. This thermoplastic polymer, polyolefin, is designed to have a very high Young's modulus at operating temperatures to ensure a good stress distribution within the composite sandwich, but a melting temperature low enough to ensure a good wettability of the skin and core during manufacturing, providing a good adhesion between the two components.

3. We demonstrate that the mechanical properties of the proposed composite sandwich structure do not change after high stress tests such as temperature cycles, humidity, etc. We demonstrate that composite-based lightweight PV modules successfully passed the damp heat, thermal cycling, humidity freeze, UV-preconditioning and even potential-induced degradations tests with a reduced power loss.

4. We demonstrate that the frontsheet of the proposed lightweight PV module is designed to pass the hail test without power loss or cracked cells and without need of a front glass. Moreover, we demonstrate that the backsheet can be easily engineered to retain the loading case. Thanks to the correct trade-off between the frontsheet and backsheet, we demonstrate that the glass-free lightweight PV device survived harsh mechanical stress tests.

5. Finally, we demonstrate that our lightweight PV modules give positive feedback also under norms indispensable for building construction, such as the *CEN/TS 1187: Test methods for external fire exposure to roofs*. The most promising solutions passed the fire test; the fire extinguished itself and damages to the PV module were minimal. These results were validated on both the frontsheet and backsheet.

These findings open new perspectives for the adoption of lightweight PV modules both by potentially decreasing the cost of BIPV production and installation and by enabling improvements on the stability of lightweight PV designs. From this work, three articles were published in peer-reviewed journals [87–89]. The lightweight elements developed in this thesis have also led to the application for an international patent with the title *"Lightweight Solar Photovoltaic Module"*, which is under revision during the time of the writing of this thesis. Moreover, the results of these research efforts also led to presentations at various international conferences with contributions to four conference proceedings (the complete list of publications can be found at the end of this thesis in the *Publication List* section).

2 Experimental Methods

Summary

This chapter focuses on the materials and experimental methods used for the development and characterization of our lightweight PV modules. We start by explaining the materials used for the manufacture of lightweight modules in section 2.1 and then the experimental methods for the characterization of materials and PV modules in sections 2.2 and 2.3, respectively.

2.1 Materials

The lightweight PV module can be divided into two main components: the back cover (the composite sandwich structure) and the front cover (the polymeric frontsheet). In the lightweight PV module design, backsheet will be addressed to the full composite sandwich structure, which is composed of the skins, the core and the adhesive (figure 2.1).
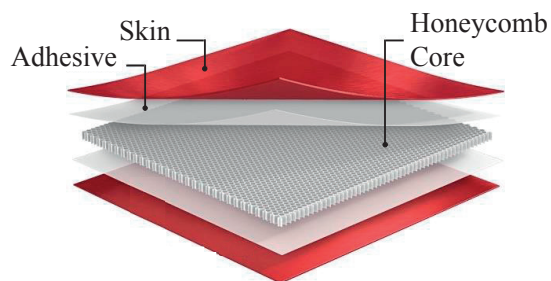

Figure 2.1 – Composite sandwich structure (backsheet) composed of two skins bonded to a core with an adhesive (figure taken from [90]).

2.1.1 Honeycomb core

We selected two types of honeycomb core to test: a 6-mm-thick 48 kg/m^3 aramid hexagonal honeycomb with a 3.2 mm cell size from Coremaster Advanced Composites and a 6-mm-thick 77 kg/m^3 aluminum hexagonal honeycomb with a 4.8 mm cell size from Euro-Composite®. Both cores are industrial grade. The two cores were selected for their heat thermal conductivity properties. The properties of the two cores are listed in table 2.1.

Table 2.1 – Mechanical properties of the sandwich core. L and W stands for the ribbon direction and direction normal to ribbon, respectively.

Core Type	Compressive Strength [MPa]		Shear Strength [MPa]		Shear Modulus [MPa]	
	Bare	Stabilized	L	W	L	W
Aramid	1.8	2.0	1.2	0.7	36.0	24.0
Aluminum	3.9	-	2.3	1.5	456	265

2.1.2 Skin material

The composite sandwich skins were fabricated using unidirectional (UD) E-glass fiber of 220 g/m^2 in a [0/90]$_s$ configuration and reinforced with epoxy L/hardener EPH 161, yielding a skin final thickness of 0.7–0.8 mm with a mass fiber ratio of 0.65. A vacuum bag technique was used to produce our skins (see Chapter 4). After applying the epoxy resin between the four layers, the skins were sealed inside a bag and left to cure at room temperature for 24 hours. After this time, the skins were removed and post-cured for 15 hours at 100°C with a heating rate of 0.2 °C/min.

2.1.3 Adhesives

We selected two types of adhesives: a thermoset material, which is a polymer that can cross-link and form irreversible chemical bonds during the curing process, avoiding the risk of polymer remelting when heated, and a thermoplastic material, which is a polymer that can soften when heated and become more fluid as additional heat is applied. In this case, the curing process is reversible as no chemical bonds are formed. Specifically, we used ethylene-vinyl acetate (EVA S88 Bridgestone) and epoxy (epoxy L/hardener EPH 161) as thermoset polymers, and ionomer (SentryGlas and PV5004T from DuPont) and polyolefin (polymer formulation developed internally by CSEM, it is a polymer produced from a simple olefin as a monomer) as thermoplastic polymers. The type of processing used depends on the adhesive selected. For an epoxy-based sandwich (our reference sample), a multi-step process is needed: (1) assemble solar cells with the inner skin of the backsheet, (2) laminate the assembly ($\approx$20 min), (3) assemble laminate with the core and skin by applying a liquid-epoxy adhesive in a wet-layup technique ($\approx$20 min), and (4) process in a vacuum bag to fully cure the adhesive ($\approx$24 hours). Figure 2.2 represents all steps necessary to process an epoxy-based lightweight module. By

1. Assembly of cells with inner skin   2. PV lamination   3. Assembly of laminate with core and outer skin   4. Vacuum bag

Figure 2.2 – Multi-step process for manufacturing of lightweight PV modules using an epoxy adhesive: (1) assemble solar cells with inner skin, (2) standard PV lamination process, (3) introduction of epoxy between laminated module and core and in between core and second skin and (4) the vacuum bag process.

substituting epoxy for PV adhesives, we aim to reduce the manufacturing time, reducing the cost of production and finally propose a process compatible with equipments used already within PV industry. The PV adhesive-based lightweight modules were manufactured using common PV processes (standard PV lamination guidelines using a flat-bed vacuum bag laminator).

We carefully consider the cost of materials during the development of lightweight modules. In large-scale production, these materials can achieve low costs: 5–20 \$/m^2 for the aluminum honeycomb structure, 10–20 \$/m^2 for the glass-fiber-reinforced polymer and 3–5 \$/m^2 for the adhesive layers. No additional manufacturing costs are expected since the sandwich structures will be optimized to use standard lamination processes.

2.2 Tools for characterization of the sandwich materials

2.2.1 Differential scanning calorimetry

Differential scanning calorimetry (DSC) is a common thermo-analytical technique that measures heat flow into or from a sample under heating, cooling or isothermal conditions, as a function of sample temperature. It allows for measuring the thermal transitions of polymers, including the glass transition temperature T_g (the temperature at which a polymer changes from a viscous or rubber condition to a hard or relatively brittle one due to changes in chain mobility), melting temperature T_m (the temperature at which a polymer changes from a solid to a liquid state, in which polymer chains are able to move freely) or crystallization (the temperature above T_g at which chains have enough energy to form ordered arrangements) as well as following exothermic or endothermic reactions [91, 92]. DSC is used within the PV industry to determine the gel content of EVA encapsulant in a reduced testing time (close to 30 minutes). Figure 2.3 shows a characteristic DCS thermogram of a non-cured EVA for a temperature range of -50 to 200°C. The main phase transitions can be identified as: (i) the glass transition between -40 and -20°C [93, 94], (ii) the melting peak from 55 to 65°C [95], and (iii) the exothermal decomposition of the additives (primary peroxides) corresponding to
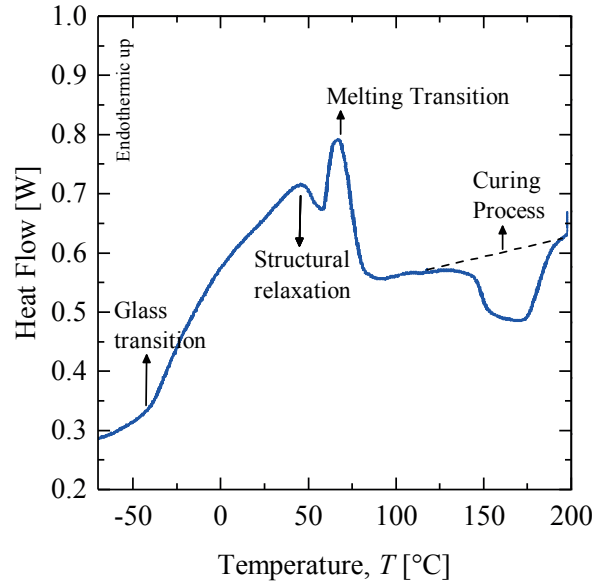
Figure 2.3 – Characteristic DSC thermogram of uncured EVA. The glass transition temperature appears at around -30°C, two endothermic peaks are found at about 45 and 60°C and the exothermic peak, which corresponds to the thermal decomposition of the additives (mainly peroxide), from 110/130 to 200°C.

the reaction of EVA cross-linking from 110 to 200°C [96]. The enthalpy (peak integral) of the exothermal transition from 110 to 200°C is proportional to the amount of residual peroxide in the EVA [91]. Assuming a homogeneous initial distribution of peroxide, the enthalpy of the exothermic transition of our samples ΔH_{cured} is directly related to the peroxide consumed during the cross-linking reaction and hence to the EVA gel content, according to [97]

$$X = \frac{\Delta H_{\text{uncured}} - \Delta H_{\text{cured}}}{\Delta H_{\text{uncured}}} \tag{2.1}$$

where X is the degree of cross-linking and $\Delta H_{uncured}$ corresponds to the enthalpy reaction of the uncured EVA reference. DSC measurements were performed on a Mettler Toledo DSC1 system operated in single-run mode. The samples consisted of 1-mm-thick discs of 5–10 mg. Thermograms were recorded under constant nitrogen flow from -20 to 225°C at a heating rate of 10°C/min, held at 225°C for 1 min and then cooled to 20°C at a cooling rate of 10°C/min.

2.2.2 Rheology

Rheology is the study of the flow and deformation of materials under the effect of an applied force [98]. It helps to describe the mechanical behavior of materials as a function of stress, strain, temperature and pressure in order to develop materials with correct processing behav-
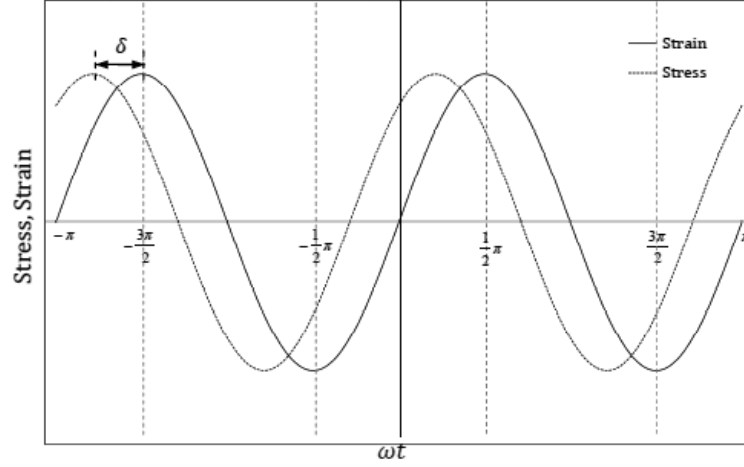
Figure 2.4 – Sinusoidal forms of stress and strain of viscoelastic materials. The phase lag δ between stress and strain depends of the viscoelasticity of the material (figure taken from [98]).

ior. During this technique an oscillatory deformation is applied to a material and the resulting response is measured with a phase lag expressed as the phase angle δ (figure 2.4).

In fully elastic materials the stress and strain are directly proportional, so both are in phase (following Hooke's law) [99]. For viscous materials, the deformation is time-dependent and the relationship between the stress and strain rate is determined by Newton's law. The viscoelastic materials' behavior lies somewhere between Hookean and Newtonian materials. Their viscoelasticity makes the materials' response to stress-strain behavior time-dependent and their deformation partially reversible. The applied strain (ϵ) and the measured stress (σ) are described according to

$$\epsilon \;=\; \epsilon_0 sin(\omega t) \tag{2.2a}$$
$$\sigma \;=\; \sigma_0 sin(\omega t + \delta) \tag{2.2b}$$

where ϵ_0 is the strain amplitude, and ω the angular frequency. Stress consists of in-phase and out-of-phase components. The in-phase component corresponds to the elastic part of the material; the out-of-phase components to the viscous part of the response to applied strain. Based on these models, it is possible to calculate the viscoelastic moduli properties:

Complex modulus (G^*) – measure of a material's overall resistance to deformation.

$$G^* = G' + iG'' \tag{2.3}$$

Storage modulus (G') – amount of energy stored in the material. Measure of elasticity of a material.

$$G' = \frac{\sigma_0}{\epsilon_0} cos\delta \tag{2.4}$$

Loss modulus (G'') – energy dissipated during the deformation. Measure of the viscous component.

$$G'' = \frac{\sigma_0}{\epsilon_0} sin\delta \qquad (2.5)$$

Loss factor ($tan\ \delta$) – measure of material damping (such as vibration or sound damping). The greater this value is, the higher dampening the material exhibits, because the G'' of the material is greater than the G', meaning that the viscous component of the G^* dominates the material's behavior.

$$tan\delta = \frac{G''}{G'} \qquad (2.6)$$

Complex viscosity (η^*) **–** relation between the complex modulus and frequency, consisting of the viscous and elastic parts.

$$\left|\eta^*\right| = \frac{|G^*|}{\omega} \qquad (2.7)$$

The rheology properties of the sandwich adhesive layer were analyzed by using a dynamic moving-die rheometer (D-MDR). The measurements were performed using an MDR 3000 Professional by Montech Werkstoffprüfmaschinen GmbH and a cone-cone geometry: the lower plate was stationary, while the upper plate oscillated at a small angle (typically 0.5°) and at a frequency of 1 Hz. During this measurement, the torque and the phase shift oscillation were continuously recorded. The rheology measurements were performed from 30°C up to 170°C.

2.2.3   Dynamic mechanical analysis

Similar to rheology, dynamic mechanical analysis (DMA) is also used to obtain the viscoelastic behavior of materials. However, it is used especially when the sample material does not flow
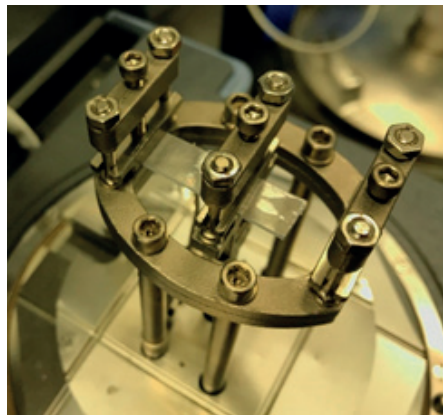

Figure 2.5 – Single-cantilever beam geometry used in dynamic mechanical analysis (DMA).

easily and hence cannot be sheared between surfaces without slippage [100, 101]. To study the properties of the skins and the frontsheet, DMA is thus the ideal method to evaluate the temperature-dependent viscoelastic properties, i.e. elastic storage (E') and loss (E'') modulus and the T_g. DMA was performed on a TA Instruments Q800 dynamic mechanical analyzer in the single-cantilever configuration (figure 2.5). Specimens were subjected to a constant sinusoidal deformation with 20 μm of amplitude at an oscillation frequency of 1 Hz, while the temperature increased from the ambient laboratory temperature of 21±3°C to 170°C at a rate of 5°C/min. By DMA, the T_g of the skins is identified as the onset value on the storage modulus curve ($T_{g,onset}$), used as reference in guidelines for structural FRP design [102].

2.2.4 Fourier transform infrared spectroscopy

The Fourier transform infrared (FTIR) spectroscopy is an analytic technique used to identify the materials of the commercially available lightweight modules. Two types of studies were performed. Samples were measured in attenuated total reflectance (ATR) mode on a Bruker Tensor 27 FTIR-Spectrometer with a Smart Orbit diamond ATR unit from Thermo over a continuous scanning from 600–4000 cm^{-1} (the background is collected on a clean ATR crystal). Samples on germanium discs were also measured in transmission mode on a Bruker Tensor 27 FTIR-Spectrometer during a continuous scanning from 600–4000 cm^{-1} with Opus software. In both cases, each layer was analyzed by 64 scans recorded with a resolution of 4 cm^{-1}.

2.2.5 Peel test

The peel test is the most widely used technique to measure adhesion strength in the PV industry [104–107]. This technique consists of pulling a peel arm from the peeling substrate of interest at a constant rate, as represented in figure 2.6. We used a simple single-arm peel test, where the peel arm is pulled with an angle θ. The peel strength (P_s [N/cm]) represents the adhesion strength between the peel arm and the peeling substrate and is calculated as the ratio between the average peeling force, when the bond line delaminates steadily, and the sample width [103, 104, 108]. The measured peel strength does not depend only on the interfacial adhesion strength, but also on the mechanical properties of the peel arm which might cause different levels of plastic energy dissipation on it. For this reason, we selected
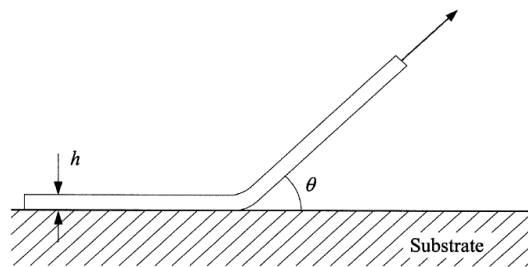
Figure 2.6 – Single-arm peel test used to measure peel strength (figure adapted from [103]).

the same peel arm material for all the adhesion study (Dun-Solar PPE+ backsheet). This test was performed to study the adhesion between the sandwich skins and polymeric adhesives in a 90° peeling test configuration. The test was performed on an Instron Zwick Roell Z020 mechanical testing instrument equipped with a 1 kN load cell in a displacement control test at a fixed rate of 100 mm/min at room and high temperature.

2.2.6 Tensile testing

Tensile testing is used to evaluate a material's rigidity (Young's modulus, E [Pa]) and the maximum stress that the material can withstand before failure (ultimate tensile strength, σ_{UTS} [Pa]) [109]. This test was used to evaluate the mechanical properties of the skins and was performed on a hydraulic universal testing machine (Instron 8800) with a video extensometer at a constant cross-speed of 1 mm/min. Tests were performed at room temperature, at 80°C and on aged samples (after damp heat and thermal cycling), according to *ASTM D3039* [110]. The E is calculated by applying a linear regression to the slope of the stress-strain curve obtained during the tensile test in the elastic regime (figure 2.7). The σ_{UTS} is calculated as the maximum load prior to failure (F_{max} [N]) divided by the average cross-sectional area (A [mm^2]).
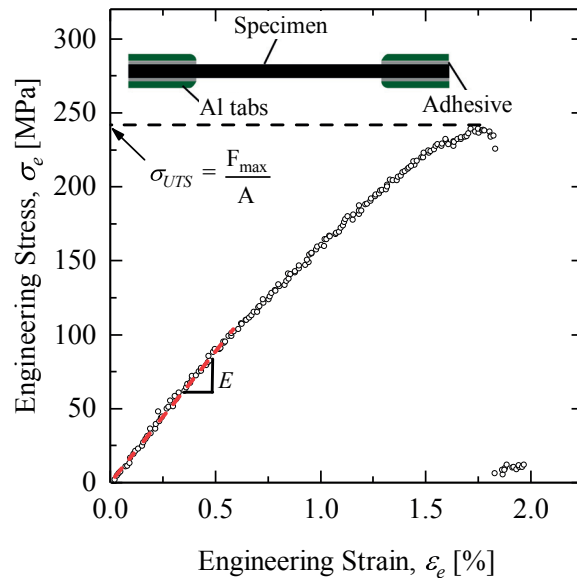
Figure 2.7 – Typical stress-strain curve obtained during a tensile test for a composite sandwich skin. The linear fit is used to calculate the Young's modulus (E) and the maximum stress is the ultimate tensile strength (σ_{UTS}). Above, it is presented a sketch of a tensile specimen with aluminum tabs.

2.2.7 Four-point bending tests

Sandwich structures are usually designed to resist bending loads. Bending tests are thus performed to assess their mechanical performance. During this test, three main characteristics are measured:

- Bending stiffness, D [N·m^2]: the resistance of a beam against bending deformation.

- Yield load, P_Y [N]: the limit of the elastic region. Beyond this threshold, the sandwich deformation becomes irreversible.

- Failure mode: this gives a direct insight into the weakest element or interface in the sandwich. More details are given in Chapter 4.

There is a three-point bending test and a four-point bending test. The three-point bending test is generally used to measure only the beam stiffness because failure usually occurs under the loading point, producing local indentation and compressing the skin, from where no valuable information can be obtained. In a four-point bending test the area between the two inner loading points is free of shear and, since the load is applied over two points, the magnitude of local indentation is reduced. The requirements of the four-point bending test are defined in the *ASTM C393-00 – Standard Test Method for Flexural Properties of Sandwich*

(a) Typical load-displacement plot obtained during a four-point bending test

(b) Sketch of the four-point bending test setup
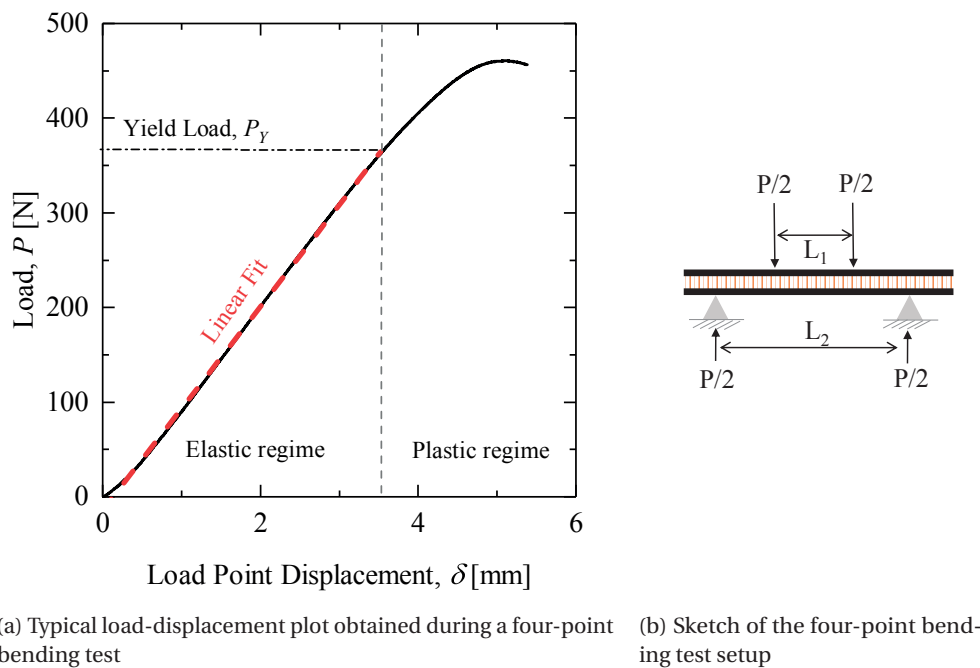
Figure 2.8 – Setup and data obtained during a four-point bending test: (a) the setup and (b) a typical load-displacement curve obtained with indication of elastic and plastic regimes.

Constructions [111] in which the deflection of the loading points is given by

$$\delta_x \left(\frac{L_2 - L_1}{2} \right) = \frac{P(L_2 - L_1)^2(L_2 + 2L_1)}{48D} + \frac{P(L_2 - L_1)}{4S} \tag{2.8}$$

The parameters P and δ are the applied load and load point displacement respectively, as shown in figure 2.8a. D and S are the bending and shear stiffness, respectively. Since during the four-point bending test the beam is free of shear in between the two inner loading points, equation 2.8 is reduced to

$$\delta = \frac{P(L_2 - L_1)L_1^2}{48D} \tag{2.9}$$

Figure 2.8b shows the experimental setup used during this test. The investigated samples have a width of 25 mm and a length of 220 mm. The test uses an outer load span (L_2) of 190 mm and an inner load span (L_1) of 95 mm. All tests were performed using a Walter+Bai AG EC80 MS mechanical testing instrument in displacement control at a rate of 20 μm/s. A linear variable differential transformer (LVDT) was used to measure the load point displacement and the applied load was measured with a 10 kN load cell. The results obtained from the measurements were compared with the values obtained by beam theory prediction, which assumes that the beam is made with a perfect adhesive and a rectangular cross section (given by equation 4.2). For well-bonded cores, the in-plane shear stiffness is sufficiently large so that the overall displacement is dominated by the bending momentum δ_D only. The sandwich beam stiffness D can thus be determined from the slope of the bending curve in the elastic regime [112].

2.2.8 Ultraviolet-Visible Spectroscopy

Ultraviolet-visible (UV-Vis) spectroscopy is an analytical tool used to measure the yellowness index (YI) and the haze factor of transmitted or reflected light through polymeric PV encapsulants. The YI is a number that indicates the degree of deviation of an object color from colorless or from a preferred white, towards yellow [113]. The YI is derived from the spectral transmittance or reflectance measurements according to *ASTM Method C313–10* [113] and is calculated as follows

$$YI = \frac{100(1.301X - 1.149Z)}{Y} \tag{2.10}$$

where *X, Y* and *Z* are the tristimulus values in the *XYZ* color system using the CIE Standard Illuminant D65 spectrum (according to *ISO 11664-1/2*). A YI value of 0.00 indicates no optical absorption between 360 and 830 nm; a YI value >0.00 indicates yellowing from absorption in the blue region of the spectrum and a YI value <0.00 indicates a shift towards blue due to absorption in the red region of the spectrum [114]. In this study we use a UV-Vis-near-infrared spectrophotometer (Lambda-950 equipment from PerkingElmer), dual-beam, covering the spectral range from 280 to 2500 nm with a measurement increment of 1 nm. The system is equipped with an integrating sphere to measure the total transmittance and reflectance [114–116].

2.2.9 Contact angle measurement

The contact angle measurement is normally used to quantify the wettability of a solid surface by a liquid. In our case, this test was performed to evaluate the wettability of the different sandwich adhesives (epoxy, EVA and polyolefin) with three different solid substrates: skin, aluminum and aramid. The contact angle (θ) is defined by the mechanical equilibrium of the drop under the action of three interfacial tensions: solid-vapor (γ_{sv}), solid-liquid (γ_{sl}) and liquid-vapor (γ_{lv}) (figure 2.9a) [117]. θ is the angle measured through the liquid, where a liquid–vapor interface meets a solid-liquid interface. Small contact angles (<< 90°) correspond to high wettability, while large contact angles (>> 90°) correspond to low wettability. Figure 2.9b shows the contact angle setup composed of an optical part that includes an IDS camera with 3.1 Mpix CMOS sensor from ON Semiconductor and an optical lens with a focal distance of 5 mm, a light source positioned behind the sample to make the liquid drop appear black, and a heated support mounted on a translation system, allowing for subtle focus adjustments. All parts are mounted on an aluminum breadboard.

(a) Polymer drop

(b) Contact angle setup
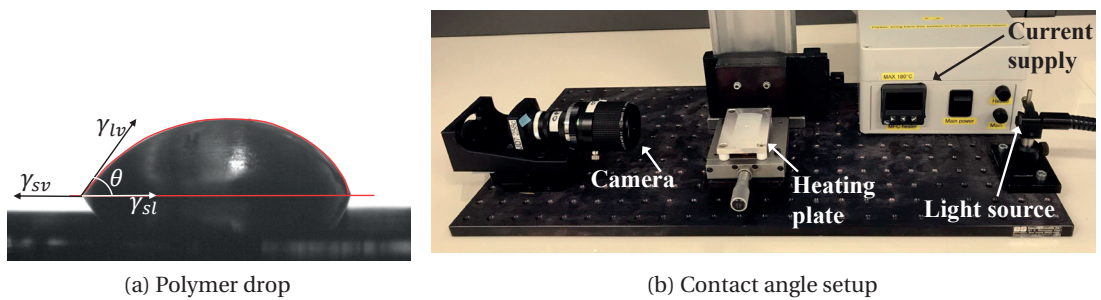
Figure 2.9 – Contact angle measurements: (a) example of a polymer drop used for the contact angle analysis and (b) the contact angle setup used during the tests.

2.3   Tools for characterization of module performance

2.3.1   Current-voltage (I-V) measurements

The fundamental electric characteristics of a PV module are evaluated by means of a current-voltage (I-V) measurement. I-V curves represent all the combinations of current and voltage at which the module can operate. This method consists of scanning an applied voltage across the solar cell and measure the current response of the solar cell. An I-V curve is often displayed with its associated power-voltage (P-V) curve (igure 2.10). The power at each voltage point is calculated using the corresponding I-V curve [118]. In order to compare the efficiency of different PV modules, this measurement has to be performed at standard test conditions (STC) as defined by *IEC 60904–3:2016* [119]: the module is at 25°C, illuminated by a simulated light with an intensity of 1000 W/m^2, with AM1.5G being the reference solar spectrum. From the I-V measurement, we can calculate the parameters indicative of device performance such as:

- The open-circuit voltage (V_{oc}) – the voltage when the current in the solar cell is zero, representing the maximum voltage that can be obtained by a module.

- The short-circuit current (I_{sc}) – the current passing through the solar cells when there is no voltage crossing it, representing the maximum current that could be obtained if materials behave optimally. This parameter depends on some factors such as the area of the solar cells, the incident light source, the spectrum of the incident light, and the optical properties of absorption and reflection of the solar cell.

- The current (I_{MPP}) and voltage (V_{MPP}) at the maximum power point.
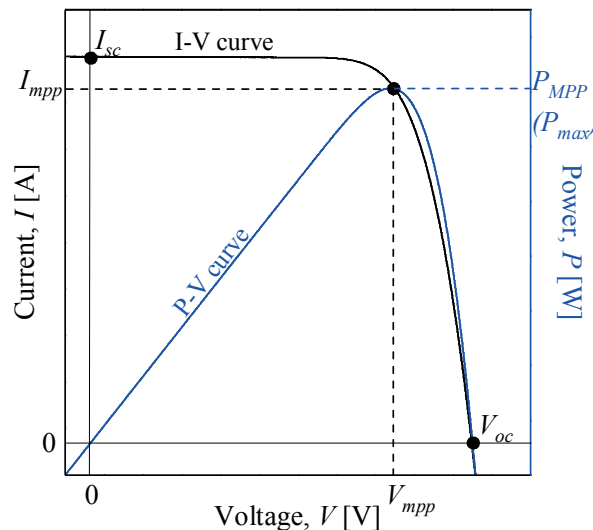
Figure 2.10 – Characteristic current-voltage curve (I-V curve in black) and power-voltage curve (P-V curve in blue) of a PV module, with relevant electrical characteristics.

- The maximum power point (P_{MPP}) – the maximum power that can be extracted from the PV device. It is the product of the I_{MPP} and the V_{MPP} and is located at the knee of the I-V curve.

- The fill factor (*FF*) – determines the maximum power delivered by the solar cell and is defined as the ratio of the maximum power produced from the solar cells to the product of $V_{oc} \cdot I_{sc}$. A *FF* of 1 represents a perfectly square I-V curve, a physical impossibility but a useful reference shape $\left(FF = \frac{V_{MPP}I_{MPP}}{V_{oc}Isc} \right)$. Expressed as a percentage (%).

- The efficiency (η) – the ratio of the electrical power output to the incident light power input under STC $\left(\eta = \frac{P_{MPP}}{P_{in}} \right)$. Expressed as a percentage (%).

- The series (R_s) and shunt (R_{sh}) resistance – parasitic resistance caused by contact resistance, resistance of the top metal contacts, resistance of lateral conduction in the emitter or manufacturing defects.

The I-V curves are measured indoor using a solar simulator device. The PV module is placed horizontally over a glass table with the solar cells facing downwards and connected in the four-point probe configuration (to remove the effect of probe/cell contact resistance). The device is then illuminated by a set of halogen and LED light sources which replicate the AM1.5G spectrum. The temperature of the device is recorded by a temperature sensor placed at the back of the module. The I-V curve is corrected by the software to STC (25°C) for temperature deviations using the measured temperature and the temperature coefficients for V_{oc}, I_{sc} and P_{MPP}. The measurement uncertainty of the setup is estimated at ±3%, and the reproducibility at ±1%.

2.3.2 Electroluminescence (EL)

Electroluminescence (EL) imaging of PV devices is an easy and non-destructive method that provides a qualitative analysis of the PV module including identification of shunts, pre-breakdown sites, cracks, broken fingers and interconnections. During this test, a DC current (typically the value of I_{sc}) is injected in the module to stimulate radiative recombination of electrons and holes in the solar cells [118]. These photons emitted by the solar cells
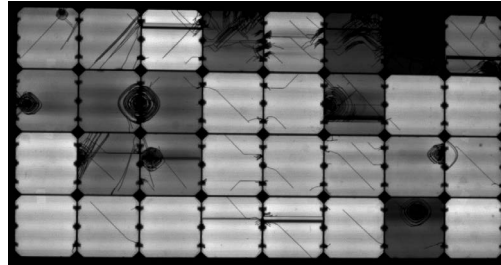
Figure 2.11 – Typical electroluminescence (EL) imaging of a commercial lightweight PV module after accelerated-aging tests, showing shunt regions and cracked cells.

are detected by a charge-coupled device (CCD) camera from Sensovation, model SamBa Ci equipped with a Nikon lens with a fixed focal length and a pixel resolution of 1660×1252. Images are acquired in dark conditions to reduce background noise. Figure 2.11 shows an example of an EL image where many defects are easily detected.

2.3.3 Wet leakage current

This test evaluates the insulation resistance of the module under wet operating conditions. The test was performed by submerging the module in a tank that contains water and a wetting agent with a resistivity ≤3500 Ω·cm and a temperature of 22±2°C. The solution covered all module including junction box and cables. Once the module is installed, the short output terminals of the module were connected to the positive terminal of the dielectric strength tester and the liquid test solution is connected to the negative terminal of the test equipment. A voltage of 500 V was applied (or the maximum voltage of the module) for 2 min. The current was measured and used to calculate the insulation resistance. More details can be found in *IEC61215:2016* [66].

2.4 Accelerated-aging tests

Seven accelerated-aging tests were performed according to *IEC 61215* [66] and the *IEC 62804* [80] as described in the following subsections.

2.4.1 Thermal cycling (TC)

Two- and sixteen-cell modules are subjected to temperature cycles from -40 to 85°C for 200 cycles (equivalent to 50 days). The modules were connected in series and a current corresponding to I_{max} was applied when the temperature was above 25°C. The most promising lightweight PV modules were subjected to up to 500 thermal cycles.

2.4.2 Damp heat (DH)

The test is performed by introducing a two-cell module and a sixteen-cell module into a chamber at 85°C and 85% relative humidity for 1000 h. An extended damp heat test (of up to 2000 h) was performed with the most promising lightweight modules.

2.4.3 Humidity freeze (HF)

Two-cell modules are subjected to cycling between a temperature of 85°C, with a relative humidity of 85%, and -40°C. PV modules are subjected to 10 complete cycles in the closed climatic chamber (10 days). During the humidity freeze test a continuous current flow of no more than 0.5% of the measured STC peak power current is applied to all modules. Again,

most promising lightweight designs were submitted to extended humidity freeze cycles (up to 100 cycles).

2.4.4 Potential-induced degradation (PID)

For the PID test the metallic module frame was simulated by an electrically conductive aluminum tape applied to the four sides as shown in figure 2.12 [120]. The modules are introduced into a climatic chamber at 85°C and 85%RH under -1000 V, as prescribed in *IEC 62804-1* [80]. However, the test duration was extended from 96h to 192h, in order to gain more information about the degradation process.
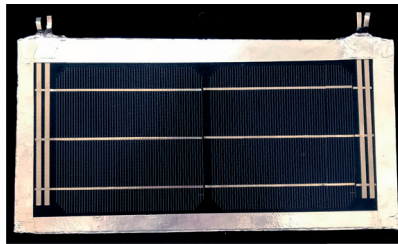
Figure 2.12 – Example of a two-cell lightweight PV module used for potential-induced degradation tests. The aluminum tape was used to simulate the frame.

2.4.5 UV Preconditioning test

This test was performed with two-cell modules installed in a temperature-controlled light-soaking chamber in dry conditions (relative humidity of around 15%). The test was performed for 11 days (equivalent to a total dose of 15 kWh/m^2). During the tests two main conditions are considered: (i) irradiance between 280–400 nm, which is lower than 250 W/m^2, and (ii) wavelength range between 280–320 nm, which corresponds to 3–10% of the total irradiance dose.

2.4.6 Hail test (HT)

The hail test setup is an internal development and is represented in figure 2.13. It comprises five main parts: a pressure gauge controller, an air reservoir, a digital pressure gauge display, an ice ball canon, and a velocity display. The ice balls were manufactured in two steps: first ice cubes were prepared using a cubic mold and, in a second step, the ice cubes were placed into an aluminum mold that produces round ice balls 25 mm in diameter. The test was performed by shooting the ice balls at a velocity of 23.5 ± 0.6 m/s. For the flexible lightweight modules (commercial solutions), modules were tested on a rigid surface support and fixed to two of its edges; for the rigid lightweight modules (solutions developed in this thesis), modules were fixed by two bars along the short edges without any rigid mechanical support. The modules were hit in four to seven different critical locations, depending on the number of solar cells.
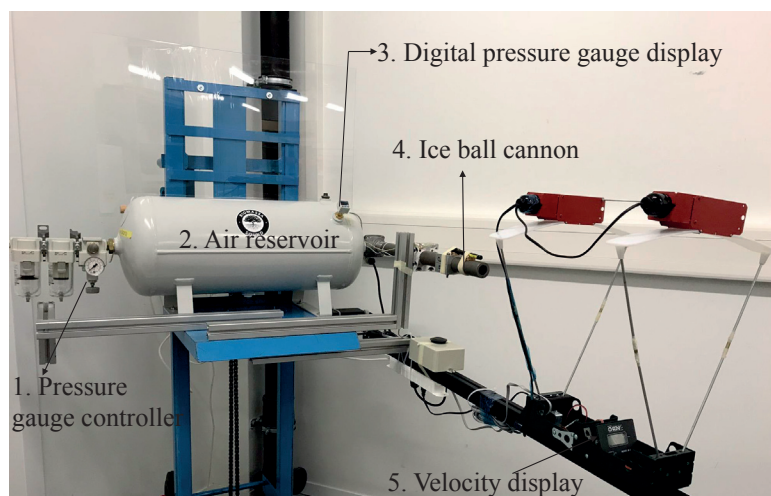
Figure 2.13 – Hail test equipment developed internally during this thesis. It is composed of a pressure gauge controller, an air reservoir, a digital pressure gauge display, an ice ball cannon, and a velocity display.

2.4.7 Static mechanical load test (ML)

The static mechanical load test applied a load of ±2400 Pa to the surface of a sixteen-cell module. This test aims at evaluating the mechanical stability of the composite sandwich backsheet thus, modules are mounted using four clamps, as represented in figure 2.14. This mounting system was selected because it does not add any extra support to the module, meaning that resistance of the module to load is provided only by the backsheet. During the test the electrical continuity of the module was constantly monitored.
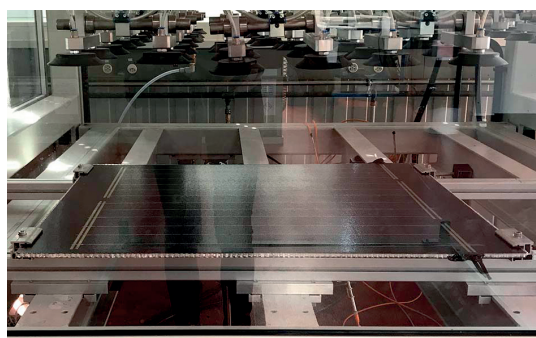
(a) Module unloaded
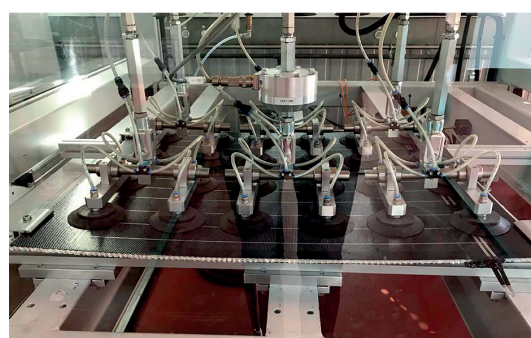
(b) Module loaded

Figure 2.14 – Example of static mechanical loading performed on sixteen-cell modules: (a) no loading and (b) loading.

3 Reliability of commercial lightweight PV modules

Summary

In this chapter, we investigate the stability of lightweight PV modules under different stresses and we show that commercial products show degradation under different accelerated-aging tests, even if the manufacturer claims compliance with relevant PV standards (IEC or UL norms). We also identify the main failure modes of lightweight modules: bending or twisting, yellowing, delamination, visual surface deformation and cell cracks. These failures are due mainly to poor material selection. These modules use materials with a high coefficient of thermal expansion that are not stable under high temperatures and humidity. Or they employ a thin or week frontsheet which does not provide the required protection to the solar cells. We conclude that semi-rigid and rigid lightweight modules show superior behavior under accelerated-aging tests and that they are less sensitive to handling (flexible modules presented many cracked solar cells).

3.1 Introduction

Weight reduction can be achieved by changing the encapsulation materials of PV modules and especially by replacing the standard glass with a lighter material. Nowadays, there are different types of lightweight PV modules present on the market [42, 51, 59, 60, 121–123]. This segment can be subdivided into two categories: flexible modules, which are mainly thin-film technology, and semi-rigid or rigid modules composed of c-Si solar cells. Lightweight modules based on thin-films are flexible structures that are very attractive for flat and curved roof tops. The advantages of such designs are the significant weight reduction, simplicity of use, custom-produced finishing and freedom in design [124]. Thin-film lightweight solutions can be manufactured in roll-to-roll production and are easily adapted to building curvatures [125–

127]. However, they offer lower conversion efficiencies, a limited field of applications and fast degradation.

Lightweight solutions based on c-Si technologies are by far more attractive for BIPV. Lightweight c-Si solutions using alternative materials to glass are available and can achieve a weight of around $3\,kg/m^2$. Such solutions are based on the substitution of the glass with a highly transparent layer at the front side (e.g. ethylene tetrafluoroethylene) and supported by a polymer backsheet or a fiber-reinforced polymer. These solutions can be flexible, semi-flexible or rigid. The drawbacks of lightweight PV for BIPV are the reduced lifetime and lack of compliance with relevant PV qualification standards.

3.2 Experimental procedure

3.2.1 Characterization of commercially available lightweight PV modules

We bought different types of lightweight modules and analyzed them according to a subset of selected and relevant IEC qualification tests [66]. Of the lightweight modules, four were flexible (developed mainly for portable and leisure applications such as for boats and caravans), one was semi-rigid and one was rigid. The latter two were both developed for BIPV applications. Table 3.1 summarizes the module types, properties and compliance with relevant standards. Based on the type of PV module, we designed different sets of aging sequences (see figure 3.1). All lightweight PV modules were evaluated electrically by means of I-V measurements. The presence of defects, such as cracked cells or bad interconnections, were identified using EL imaging, as described in Chapter 2. The modules were characterized electrically and visually before and after each test.

Table 3.1 – Dimensions, weight, warranty and indication of compliance with relevant PV standards of the commercially available lightweight PV modules tested.

Module ID	Dimensions [cm×cm×cm]	Weight [kg/m²]	Warranty [years]	Compliance [norm]
Flex-a	88×67×0.15	2.5	5	HT from IEC 61215
Flex-b	111×55×0.2	2.5	5	no
Flex-c	74×53×0.3	2.4	5	no
Flex-d	116×57×2	2	5	no
Semi-a	165×99×0.2	2.7	25	IEC 61215/61701
Rigid-a	102×99×3.8	9	25	UL 1703 and HT from IEC 61215

3.2.2 Fourier transform infrared spectroscopy measurements

No information about the materials used for the fabrication of these flexible devices is provided on the product data sheets. Thus, to understand the degradation observed under the different
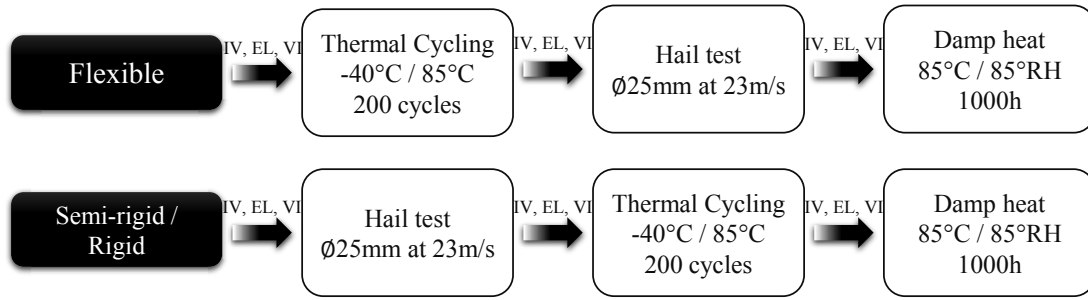
Figure 3.1 – Sequence of tests designed for the flexible, semi-rigid and rigid lightweight modules.

accelerated-aging tests, we analyzed small samples from the modules by FTIR according to the method described in section 2.2.4. Samples of 5 cm × 5 cm were cut from the module and separated into their individual layers. Each layer was measured by FTIR-ATR without further treatment. For transmission on germanium discs, the different layers were dissolved in tetrahydrofuran or hexafluoroisopropanol, pipetted onto a germanium target and dried to build a thin film of the sample material.

3.2.3 Optical measurements

The yellowness index (YI) is calculated from the UV-Vis spectroscopy technique (see section 2.2.8). We removed samples of 5 cm × 5 cm from the flexible devices and analyzed the reflectance response using an UV–Vis–near-infrared spectrophotometer. The YI is calculated according to equation 2.10 using the spectral reflectance measurement [116].

3.3 Results and discussion

3.3.1 Failure modes of flexible lightweight PV modules

Figure 3.2 shows the performance degradation from the flexible lightweight. Figure 3.3 presents EL images of the modules before and after degradation. The EL images show lots of cracks in the solar cells just after we received the modules. The absence of glass and a frame allows for weight reduction but also decreases the mechanical rigidity of the module, thus making it much more fragile (especially module Flex-c).

Thermal cycling was the first test we performed. The EL imaging of module Flex-a and Flex-b shows no major defects, having a power loss of -1.2% and -0.5%, respectively. However, a strong **yellowing** of the materials is visually noticed. The I_{sc} did not change, thus the yellowing must come from the backsheet and not from the encapsulant or the frontsheet. The module Flex-c shows a strong degradation with a power loss of -60%. This loss comes from the fact that half of the module was no longer working. This module has a bypass diode that can avoid
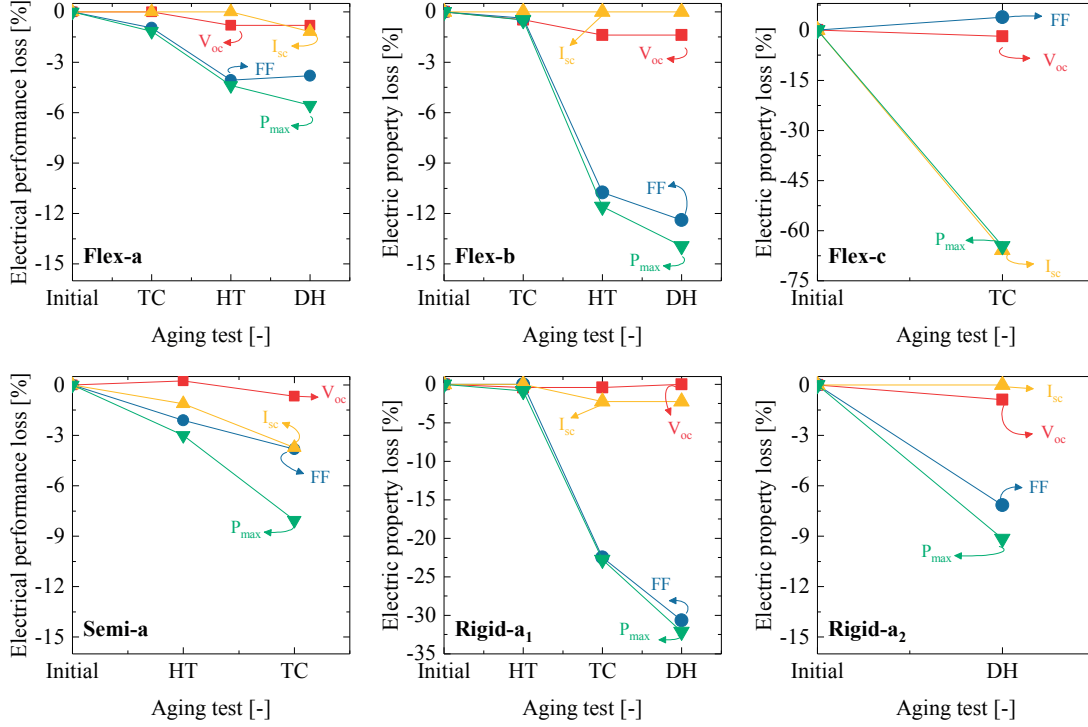
Figure 3.2 – Loss of short-circuit current (I_{sc}), open-circuit voltage (V_{oc}), fill factor (*FF*), and maximum power output (P_{max}) obtained from the flexible (top) and rigid solutions (bottom) after the sequence of aging tests defined in figure 3.1.

a big current drop (in case of defects or shadowing). In the presence of cracks or a shadow, the bypass diode becomes "forward biased" and begins to conduct current. All the current greater than the shaded cell's new I_{sc} is bypassed through the diode, thus reducing drastically the amount of local heating at the shaded area. Consequently, due to the large damages, this bypass disconnects part of the module and thus P_{max} decreases considerably. During the thermal cycling test, the materials tend to expand (when heated) and contract (when cooled). In the case of the plastic foils used to substitute for the glass, the coefficient of thermal expansion (CTE) is usually higher than other materials. This makes the module structure **bend** and **twist**, inducing cracks in the solar cells and breakage of the interconnections [128]. The CTE of plastics ($CTE_{plastics} = 50–770 \times 10^{-6}$ 1/K [25, 129, 130]) is much higher than that of silicon ($CTE_{silicon} = 3.5 \times 10^{-6}$ 1/K [131]). Due to this strong degradation, this module was not considered for further testing. The module Flex-d_1 did not pass the thermal cycling test when the module was placed vertically, like standard glass-glass modules. In this position, the module bends as can be seen in figure 3.4. By holding the module to the top of the chamber (situation where module does not support its own weight from below), the module (Flex-d_2) passed successfully the thermal cycling test with no power loss.

After thermal cycling, we subjected the modules to the hail test. The EL images show **solar cell cracks** and damages in all the impacted spots (figure 3.3). The power loss at the maximum

Figure 3.3 – Electroluminescence imaging of commercially available flexible lightweight modules after different accelerated-aging tests (thermal cycling, hail test, damp heat).

power point measured by I-V measurement is about -3.3 %, -11.1 %, and -4.3% for module Flex-a, Flex-b and Flex-d_2, respectively, relative to the power measured after thermal cycling. This test shows that the frontsheet used on these solutions is too thin to efficiently protect the solar cells against impacts. Moreover, besides the power loss lower than -5%, the impact
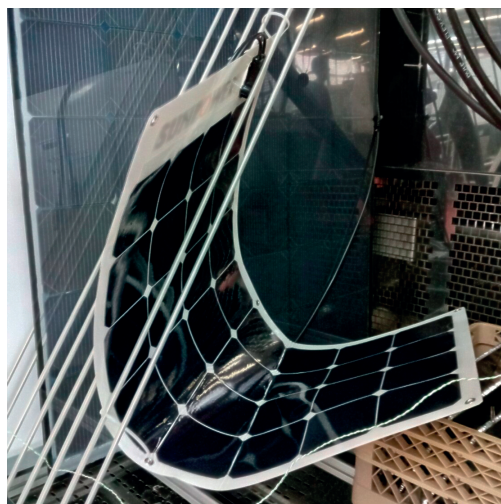
Figure 3.4 – Visual inspection of the Flex-d_1 module after a few thermal cycles. Note the module bending towards the frontsheet.

locations can be identified with the naked eye by the presence of visual cell cracks.

Finally, the damp heat induces the appearance of **delamination** and strong **yellowing** of the module components. After only 200 hours of damp heat testing, we measured a yellowness index of 4, already visible to the naked eye. From the I-V measurements, we observe a decrease of I_{sc} especially with Flex-a. This loss is due to the color change of the frontsheet from transparent to yellow, reducing the quantity of light arriving to the solar cells, and consequently the I_{sc}. In the case of Flex-d_3 (equivalent to Flex-d_2 but without being subjected to thermal cycling or hail test), we measured a reduced power loss (-0.4%). In this case, the yellowing comes from the backsheet since we do not measure any chance in I_{sc}.

3.3.2 Failure modes of semi-rigid and rigid lightweight PV modules

From our study of flexible modules, we conclude that the hail test is one of the most demanding tests for lightweight modules. Thus, we performed this test first for our study of semi-rigid and rigid lightweight modules. Figure 3.2 presents the performance degradation after each aging test. After the hail test, we measure a power loss lower than the -5% threshold (-3% and -0.9% for the semi-rigid and rigid modules, respectively). EL inspection shows, however, many **cracked cells** that correspond to the impact spots of the test (figure 3.5). Moreover, the rigid module shows a **surface deformation**, which can be detected by the naked eye, as seen in figure 3.6.

After the hail test, the modules were exposed to thermal cycling. The results show a further power degradation of -5.2% and -22.1% referent to the power after the hail test. This decrease is due mainly to the loss in I_{sc} and the increase of R_s. The rigid module shows a higher loss due to the presence of three bypass diodes that allow the current to pass around cracked cells
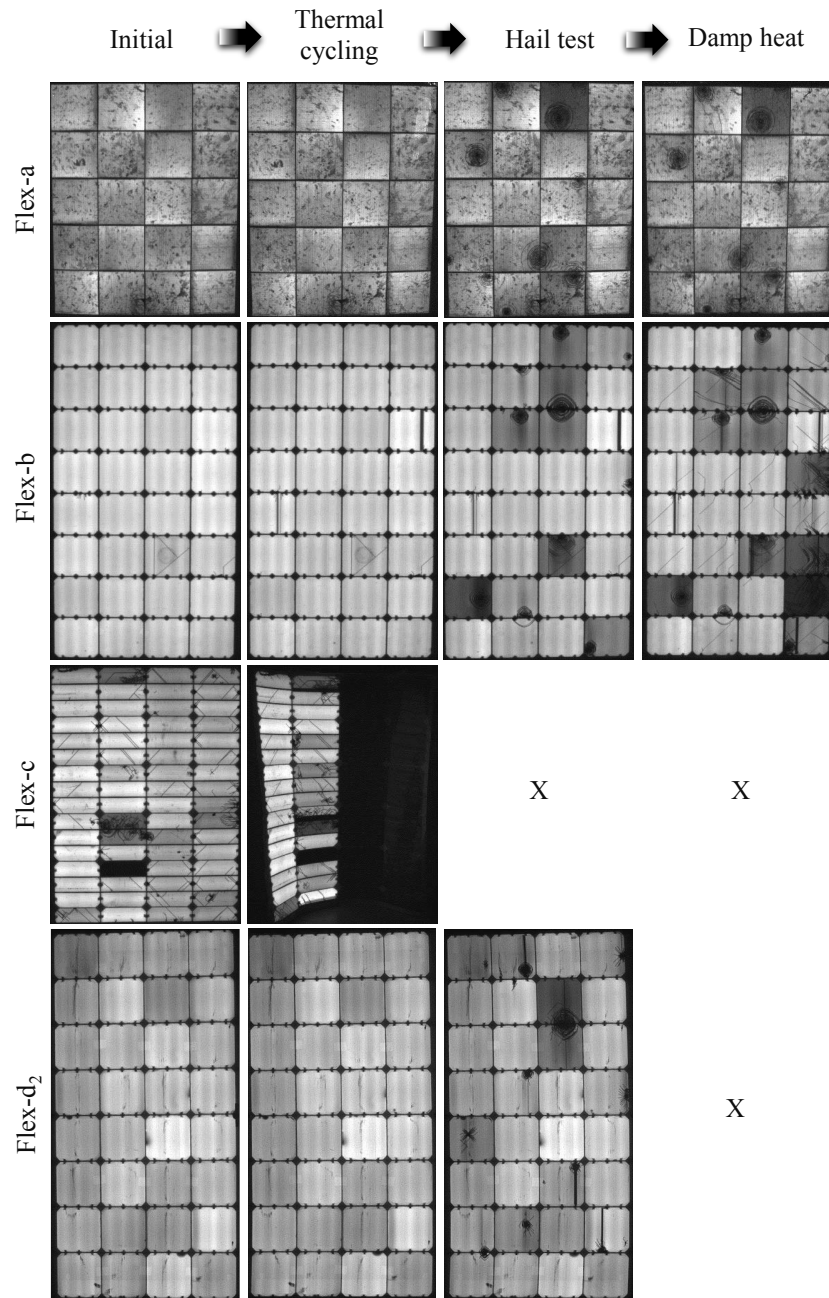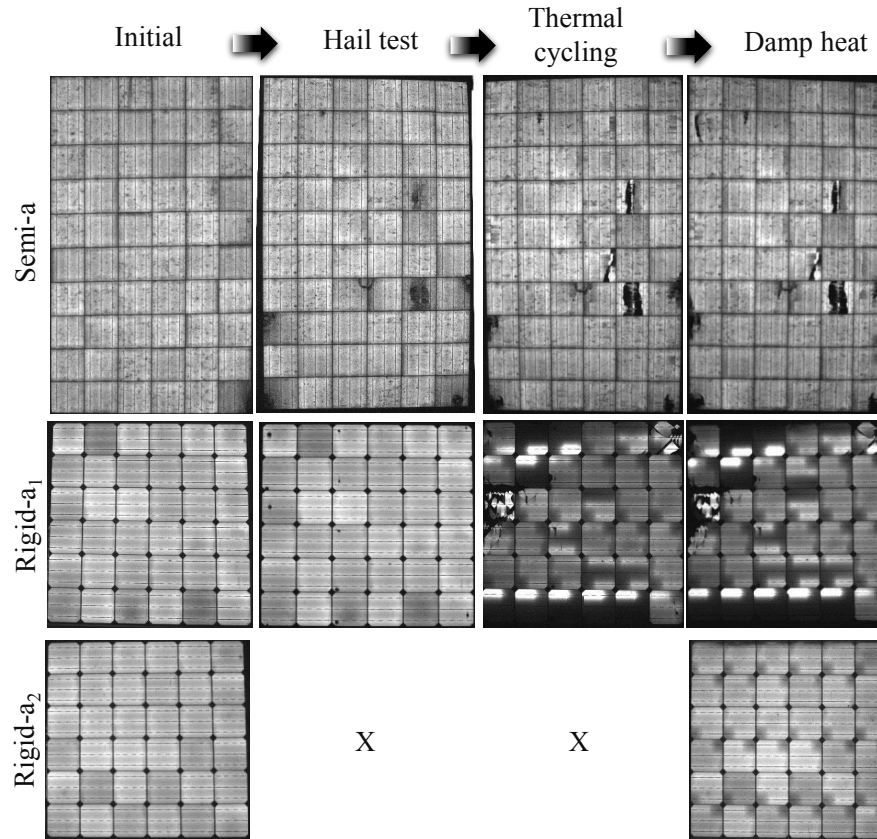
Figure 3.5 – Electroluminescence imaging of commercially available semi-rigid and rigid lightweight modules after different accelerated-aging tests (hail test, thermal cycling and damp heat).

and thereby reduce the voltage losses through the module. Both modules show a pronounced **yellowing** of their backsheets, as can be seen in figure 3.6.

The damp heat test was performed third. All the lightweight modules tested show an increase in yellowing. We also observe that some polymers melted and flowed out of the frame, and some other polymers showed a strong **milky or hazy** aspect (figure 3.6). The rigid module uses polyolefin foils as an encapsulant. Thus, when the module is heated, the chains of the polyolefin will tend to reorganize to form a big crystal. The boundary between two crystals in the polymer will promote light diffraction that makes the polymer appear milky [132]. Due to the high degradation state of the rigid module, we used a second module (Rigid-a_2) from the same producer to repeat the damp heat test (without subjecting it to the hail test or the thermal cycling test). We observed similar results: high power loss (-9%), strong yellowing of the backsheet and a milky aspect. This milkiness is concentrated on the bottom solar cells and reduced the maximum current. Consequently, the bypass diode become "forward biased" to avoid overheating this area, strongly decreasing the *FF*.

(a) Surface deformation

(b) Polymer milkiness

(c) Delamination
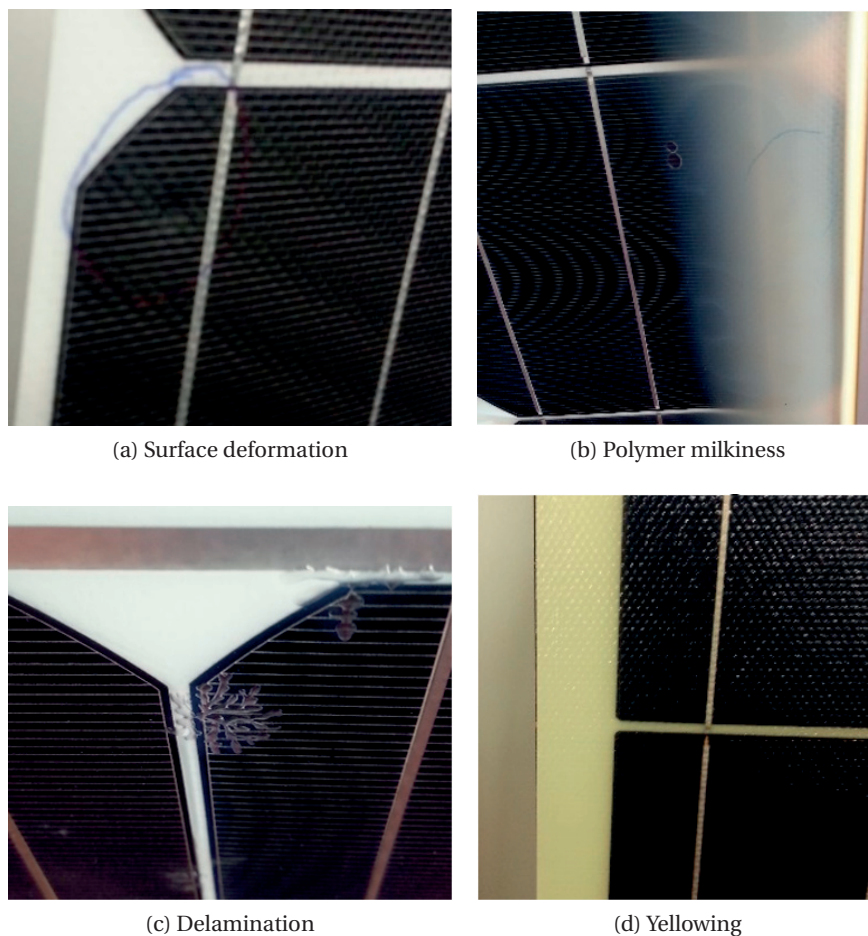
(d) Yellowing

Figure 3.6 – Main failure modes observed from visual inspection of semi-rigid and rigid commercially available lightweight PV modules: (a) surface deformation, (b) milkiness, (c) delamination, and (d) yellowing.

3.3.3 Materials characterization

Figure 3.7 shows the FTIR spectra of all the materials present in the flexible lightweight modules, showing that all the modules are composed of very similar materials:

- **Ethylene-vinyl acetate (EVA)** as a PV encapsulant. EVA is identified by the absorbance of some bands assigned to the VA units (1734 cm^{-1}, 1240 cm^{-1}, 1020 cm^{-1}, and 610 cm^{-1}) and by the absorbance of the ethylene groups (2920 cm^{-1}, 2850 cm^{-1}, 1470 cm^{-1}, and 720 cm^{-1}) [133–135].

- **Polyolefin (PO)** as PV encapsulant. PO is identified by the peaks associated with methylene stretching vibration (2915 cm^{-1} and 2846 cm^{-1}) and methylene deformations (1463 cm^{-1}, and 719 cm^{-1}) [136].

- **Polyethylene terephthalate (PET)** as a frontsheet or backsheet. PET is identified by the
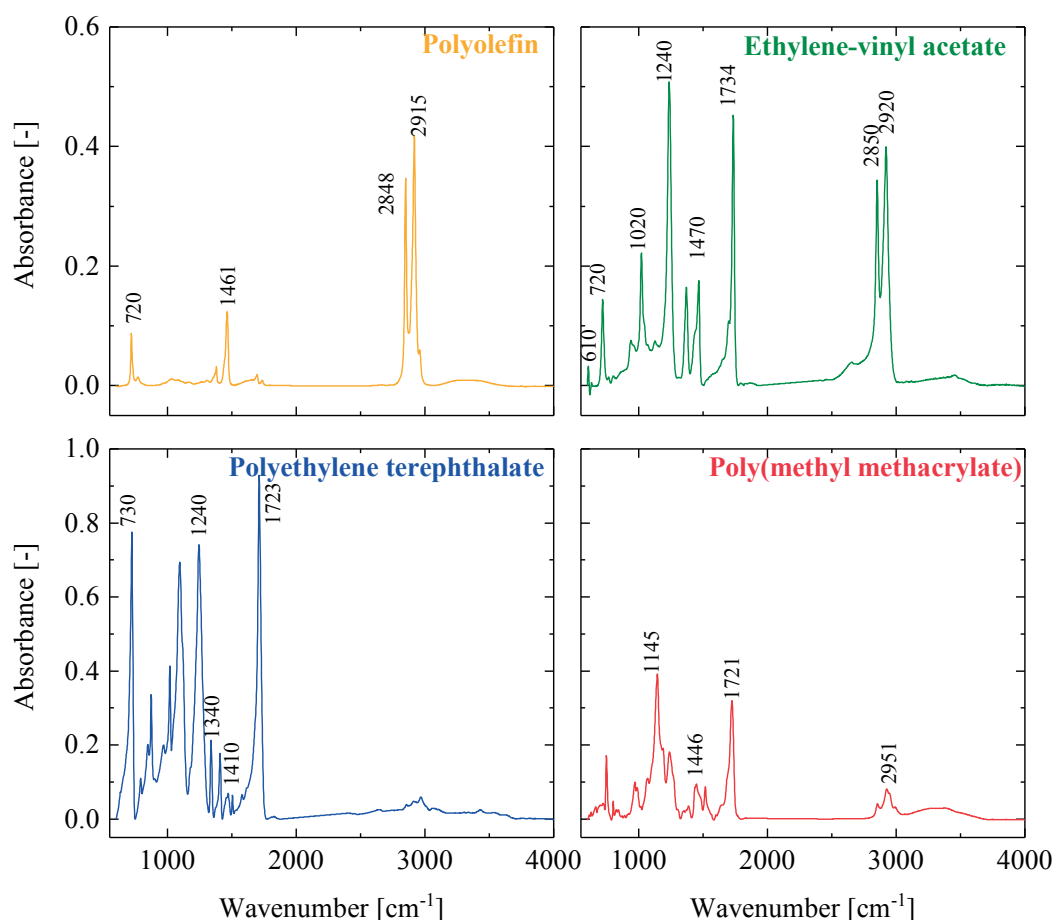
Figure 3.7 – FTIR spectra of module components with indications of main absorbance bands characteristic of each material. These results show that flexible lightweight modules are composed of: polyolefin, ethylene-vinyl acetate, polyethylene terephthalate and poly(methyl methacrylate).

absorbance of bands assigned to the ester carbonyl stretching (1723 cm^{-1}), ethylene group (1340 cm^{-1}, and 1410 cm^{-1}), terephthalate group (1240 cm^{-1}), and interaction of a polar ester group and benzene rings (730 cm^{-1}) [137–140]. In the case of some flexible modules, there is also a percentage of polyester/terephthalate on the inner side of PET.

- **Poly (methyl methacrylate) (PMMA)** as a frontsheet (Flex-d). PMMA is identified by the absorbance of the band associated with the C-H bond stretching (2951 cm^{-1}), C=O stretching (1722 cm^{-1}), CH_3 stretching (1446 cm^{-1}), and O-C stretching (1145 cm^{-1}) [141].

The results of the accelerated-aging tests performed on the flexible modules show that temperature and humidity significantly increase the yellowing of the materials. Figure 3.8 shows the YI of the three flexible devices analyzed. For all samples, we observe a linear increase of YI as a function of aging time. After only 200 h, a slight yellowing of the materials is already visible (when YI $\approx$ 4). The strong yellowing is explained by the materials identified during

(a) Total reflectance measurement
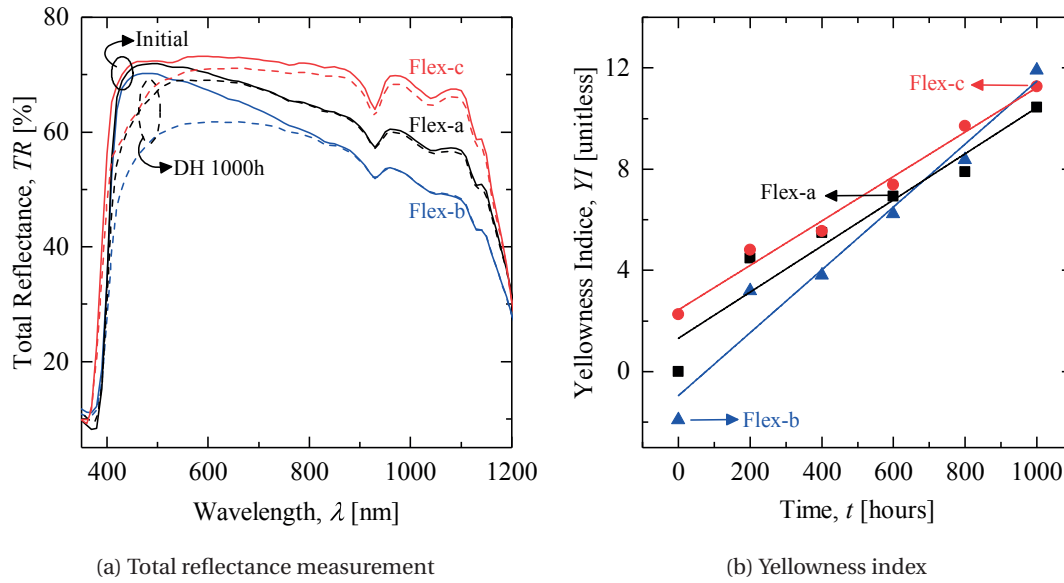
(b) Yellowness index

Figure 3.8 – Results obtained by optical spectroscopy: (a) total reflectance and (b) yellowness index of commercial available lightweight modules measured during the damp heat test.

FTIR. PET gradually degrades under high temperature, humidity and ultraviolet radiation due to the hydrolysis of the material. This degradation is caused by both thermal and hydrolytic degradation, inducing a loss of molecular weight of the polymer caused by chain scission [142–144]. Additionally, the peroxide molecules from EVA might also decompose in highly reactive peroxides, creating chromophores, making the EVA appear yellow. The EVA and PET yellowing will reduce I_{sc} as we observe from the I-V measurements. Moreover, even if there are PET and EVA formulations that do not show such high degradation rates, the manufacturers of the analyzed modules give a very short lifetime (5–10 years), thus most of the polymers used might not be stabilized for long outdoor exposure.

3.4 Conclusions

The study of commercially available PV modules based on c-Si technology showed that lightweight modules have a strong degradation under accelerated-aging tests, even if the manufactures claim compliance with relevant PV standards (IEC or UL norms). From this study, we conclude that:

- Flexible lightweight solutions are very fragile. EL images of the modules immediately after we received them showed many solar cell cracks due to handling or transportation.

- Flexible modules have a poor design. Modules were composed of polymeric materials with different thermal properties and, under thermal cycling tests, modules tend to bend and twist due to CTE mismatch. Moreover, the bending was strongest when

modules were kept in a vertical position during the test: due to the polymer softening, the mechanical stability is reduced and modules showed a strong deformation.

- All lightweight modules showed delamination and yellowing. At high temperatures and high humidity we observed a strong yellowing ($YI_{max} \approx 12$) of the module components. The yellowing was detected by visual inspection and from the reduction of I_{sc} in the I-V measurements.

- All commercial products had a weak frontsheet design. The presence of cell cracks and surface deformation after the hail test showed that the frontsheet design was too weak to absorb the impact of adverse weather conditions.

- Rigid solutions showed higher thermo-mechanical stability than flexible modules. Rigid and flexible lightweight PV modules had similar failure modes, however, the thermo-mechanical stability of the rigid solutions seemed to be less affected (no bending or twisting under high temperatures). From the data sheets of these modules, we know that they were produced with composite materials.

Table 3.2 shows the power loss relative to the state prior to the test for all the commercially available lightweight PV modules tested and their respective failure modes. These results show that the lightweight modules on the market have low thermal and mechanical stability.

Table 3.2 – ΔP_{loss} of commercially available lightweight modules after each aging test.

	TC	HT	DH	Failure modes
Flex-a	-1.2%	-3.3%	-1.3%	
Flex-b	-0.5%	-11.1%	-2.7%	bending, twisting,
Flex-c	-59.7%	-	-	yellowing, cell cracks,
Flex-d$_2$	-0.1%	-4.3%	-	delamination
Flex-d$_3$	-	-	-0.4%	
	HT	**TC**	**DH**	**Failure modes**
Semi-a	-3.0%	-5.2%	-	yellowing, milkiness,
Rigid-a$_1$	-0.9%	-22.1%	-12.8%	surface deformation
Rigid-a$_2$	-	-	-9.1%	under HT, cell cracks

With the increasing need of lightweight solutions, this study motivates us to start the development of lightweight modules that are based on c-Si solar cells and are durable under outdoor exposure. The main failure modes observed for lightweight PV modules showed that rigid modules are more resistant to thermo-mechanical stress. Indeed, from the very start, they were able to endure the stresses of handling and transportation, in contrast to some of the flexible modules, which were damaged by shipping. Thus, we will focus our attention on the design of glass-free rigid lightweight solutions.

4 Composite sandwich structures

Summary

This chapter gives a theoretical introduction to composite sandwich structures, showing their advantages over other polymer materials already used to develop lightweight PV modules. We show that designing a symmetric and balanced skin with a fiber orientation $[0/90]_s$ will limit thermal and hygroscopic deformations due to temperature and humidity changes during processing and accelerated-aging tests.

4.1 Introduction

Composite sandwich structures were first discussed by Duleau in 1820 and later by Fairbairn [145]. However, it was only after the first flight of an airplane that intensive research started with the aim of considerably reducing the weight of structures, while preserving the relevant mechanical properties [146]. After extensive studies, the mass production of sandwich structures started during the Second World War with the British Mosquito aircraft using a balsa core and plywood faces [146]. From that time, sandwich structures have been constantly re-designed and optimized, and today these structures can be found in many different applications, from high-tech satellites [41, 43–45] to bridges and buildings [147, 148] to low-cost wooden furniture [149].

A composite sandwich structure is composed of three main components: skins (also called faces), the core and adhesive, as represented in figure 4.1. The two thin and strong skins are bonded using an adhesive layer to a thick and light core. The adhesive transfers the stress between the sandwich components and plays, therefore, a critical role. Sandwich structures work similarly to I-beams. The way they function can be easily explained by studying the
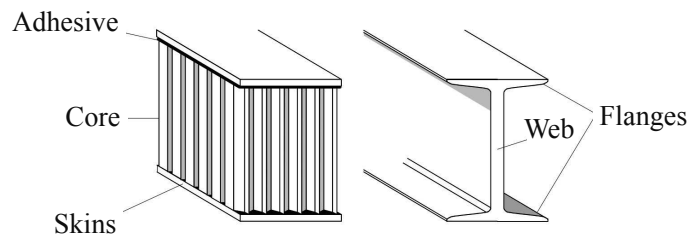
Figure 4.1 – The concept of sandwich structures and I-beams is analogous: placing of the material where it is mostly needed and removal from where it is not needed (adapted from [151]).

strain and stress acting on a beam during bending: the maximum strains are on the upper and lower skin of the beam and the lower stress is near the neutral axis [150]. Thus, to keep high stiffness and low weight, it is important to place materials with high strength where high stress occurs (top and bottom positions) and soft and light materials where the strains are low (close to neutral axis) [48]. The main difference between a sandwich and an I-beam is the fact that the core of a sandwich is made of a different material from the skins and it is spread out as a continuous support for the skins rather than concentrated in a narrow web. The adhesive bond between the skins and the core has to be strong enough to transfer the stress from one skin to another, through the sandwich core, without debonding. If the adhesive is too weak, the different sandwich components will not act together to resist an applied load and the stiffness of the structure will be usually limited by the poor mechanical performance of the core. The choice of the adhesive between the core and the skins is thus of critical importance.

The selection of the right materials allows for the development of structures with increased stiffness and strength but with reduced weight. Figure 4.2 is a generic example of the gain in strength and flexural stiffness by inserting a light core between the two skins: an 0.81-mm-thick aluminum sheet is compared to two sandwiches made by splitting the aluminum into two skins and bonding a honeycomb core between them. In bending, the thickest of the two sandwich panels is 37 times stiffer and more than 9 times stronger than the plan aluminum sheet, with a weight increase of only 6% [152].

4.2 Components of the sandwich materials

During the sandwich design phase, one of the first steps is the selection of the sandwich components: the skins, the core and the adhesive. This selection depends on the application, the required mechanical properties, the processing and, especially, the cost, since it can vary over several orders of magnitude.

4.2.1 Skin materials

The skin materials can be any structural material in the form of thin sheets [153]. The main criteria used for the selection of the ideal skin are stiffness, strength under tensile and com-

	Solid aluminum	Sandwich construction	Thicker sandwich construction
Relative stiffness	100	700 7x more rigid	3700 37x more rigid
Relative strength	100	350 3.5x as strong	925 9.25x as strong
Relative weight	100	103 3% increase in weight	106 6% increase in weight

Figure 4.2 – Generic example of the stiffness, strength and weight of composite sandwich structures compared to those of a solid aluminum panel.

pression, surface finish (adhesion to the bonding adhesive) and, in some cases, resistance to impact or environmental stress (chemical, UV, heat, etc.) [146]. There are two main groups of skin types: metallic and non-metallic materials. **Fiber-reinforced skins** are non-metallic skin. They offer many advantages. They provide strength properties very similar to, or even higher than, those of metals but with a much lower weight. It is easier to manufacture a sandwich with non-metallic skins than with metal skins. There is a large selection of fiber reinforcement that can be combined in different layers, orientation and types. This allows for the production of skins with large variety of properties depending on the application's needs.

Fibers for this type of skin are usually made of glass, aramid or carbon. Glass is the most commonly used reinforcing material in fiber composites (especially E-glass fiber). Glass fibers have good mechanical properties and environmental resistance, but it is their low cost that makes these fibers so widely used. The main disadvantages are their relatively low elastic modulus and higher density as compared to other reinforcement materials. Composites based on glass fibers and polymers are called glass fiber-reinforced polymer (GFRP). The other types of fibers, such as aramid or carbon fibers, present low densities and even higher strength and stiffness than glass fibers. Their main drawbacks are high cost and potentially brittle behavior (in the case of carbon fibers). The **matrix** of a fiber composite can be either a thermoplastic (polyamide, polypropylene, etc.) or a thermoset polymer (epoxies, polyurethane, etc). For large low-cost sandwich structures with glass fibers, polyester resins are often used, while epoxy resins are preferred for advanced applications.

4.2.2 Core

The purpose of a core in a composite laminate is to increase the laminate's stiffness by "thickening" it with a low-density core material [154]. The primary properties of interest for core selection are its density, shear modulus and strength (material's response to shear stress) perpendicular to the skins plane. There are three main core groups: light woods (such as balsa),

foams and honeycombs. Honeycombs' cores have the highest strength and stiffness ratio to weight, and are therefore used in high-tech applications such as aerospace applications. The most-used honeycombs are made of aluminum, impregnated glass or aramid fiber mats (e.g. Nomex®).

4.2.3   Adhesive

The adhesive layer links the core to the skins and has to be carefully optimized [155]. The selection of the ideal adhesive is based on the skins and core to bond and the main considerations are the toughness and strength of this layer. In a composite material the shear stress can change rapidly between the skin and the core. If the adhesive is too weak, this can lead to a complete failure of the composite structure [156, 157]. The most common adhesives are epoxy resins, phenolics, polyurethanes and polyester resins.

4.3   Design of composite sandwich structures

Designing a sandwich structure requires predicting its mechanical behavior, which depends on its construction (e.g. core thickness) and constituent properties (e.g. mechanical properties of the skins). The usual pattern for the prediction of the mechanical behavior of a sandwich structure is summarized in figure 4.3 and comprises the following steps:

1. The properties of a single unidirectional lamina (ply) are calculated based on its constituents' properties (matrix and fibers) using **micro-mechanics models**

2. The properties of the skins (laminate comprising several lamina stacked on top of each other with different fiber orientations) are studied using **macro-mechanics models** (classic laminate theory, CLT) [146, 158–160].

3. The properties of the sandwich structure (combination of skins and core) are assessed using the **sandwich beam theory**.
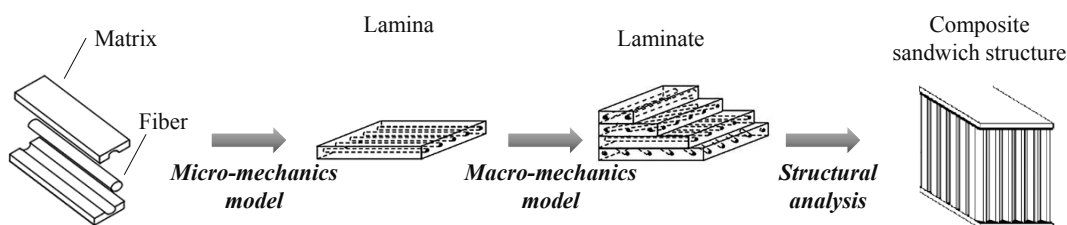
Figure 4.3 – Sequence of models used during composite structure design: (i) micro-mechanics models are used to obtain properties of the lamina, (ii) macro-mechanics models are used to obtain properties of the laminate (skin), and (iii) structural analysis models are used to obtain properties of the sandwich structure (pictures adapted from [158]).

The composite mechanics (either skins or sandwich) have been covered extensively in several books [146, 158, 160, 161]. Therefore, only the main equations used in the present work are given in this section, without a complete development.

4.3.1 Design of skins: micro-/macro-mechanics model

From composite mechanics theory, we know that laminate structures must be designed to be **symmetric** and **balanced**: the skins' symmetry will prevent warping from coupling between in-plane strains and out-of-plane rotations (curvature); and the balance reduces coupling between in-plane normal strains and in-plane shear strains (twist). Table 4.1 gives some examples of the consequences of non-symmetrical laminates. For the development of lightweight PV modules we selected symmetric and balanced skins with a fiber orientation [0/90/90/0]. With this structure, we found that skins will limit the thermal and hygroscopic deformations due to temperature and humidity changes during processing and accelerated-aging tests.

Table 4.1 – Effect caused by (non)symmetry or (non)balanced design of laminates.

Type	Fiber orientation angles	Effects
Symmetric/balance	(0, +90, +90, 0)	flat, constant mid-plane stress
Non-symmetric/balanced	(90, +45, 0, 90, -45, 0)	Induces curvatures
Symmetric/non-balanced	(-45, 0, 0, -45)	Induces twist
Non-symmetric/non-balanced	(-0, -45, 0, 90, -45, 0)	Induces twist and curvature

4.3.2 Design of the sandwich: sandwich beam theory

Knowing the homogenized engineering constants of the skins (see Appendix A), and the properties of the core, one can extrapolate the properties of the full sandwich structure.

Bending stiffness and stress

The bending stiffness (D) is calculated using the Euler-Bernoulli beam theory, which correlates the beam's deflection with the applied load. A cross section of a composite sandwich structure is represented in figure 4.4 together with the nomenclature of the different properties and thicknesses. The bending stiffness is given by

$$D = B \left(\frac{E_{f1} t_{f1}^3}{12} + \frac{E_c t_c^3}{12} + \frac{E_{f2} t_{f2}^3}{12} + E_{f1} t_{f1} (d - e)^2 + E_{f2} t_{f2} e^2 + E_c t_c \left(\frac{t_c + t_{f2}}{2} - e \right)^2 \right) \quad (4.1)$$
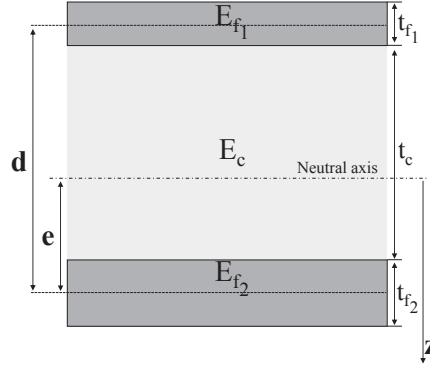
Figure 4.4 – Composite sandwich structure with designation of thickness and Young's modulus of each component.

where E_f and E_c are the in-plane Young's modulus for the skins and core, respectively, t_f the skins thickness, t_c the core thickness, B the width of the beam, d the distance between the centers of the two skins, and e the position of the neutral axis. When the two skins have the same thickness, the neutral axis is at the center of the beam, and the bending stiffness presented in equation 4.1 is simplified and becomes

$$D = B\left(\frac{E_f t_f^3}{6} + \frac{E_c t_c^3}{12} + \frac{E_f t_f d^2}{2}\right) \tag{4.2}$$

The first and second terms describe the stiffness of the two skins and the core about their own centroids, while the third term adds the stiffness of the skins about the center of the beam. When a flexural load (with a bending momentum M) is applied to the sandwich structure, the skins are loaded in tension or compression and the core is loaded in shear. Compressive (negative) and tensile (positive) maximum stress in the skins (f_1 and f_2) is given by

$$\sigma_{f1} = -\frac{M(d-e)E_{f1}}{D} \qquad\qquad \sigma_{f2} = \frac{MeE_{f2}}{D} \tag{4.3}$$

Shear stiffness and stress

The shear stiffness (S) is computed in the same way as for the beam and considering G_c as the shear modulus of the core

$$S = B\frac{G_c d^2}{t_c} \tag{4.4}$$

with T being the shear force, the maximum shear stress in the core is given by

$$\tau_c = \frac{T}{Bd} \tag{4.5}$$

Bending deflection

The maximum deflection of a sandwich beam under a bending momentum consists of two terms: one due to the momentum itself, δ_D, and another due to core deformation in shear, δ_S [112].

$$\delta = \delta_B + \delta_S = \frac{PL^3}{c_1 D} + \frac{PL}{c_2 S} \tag{4.6}$$

where c_1 and c_2 are constants that depend on the loading configuration. The parameters P and δ are the applied load and deflection, respectively.

4.4 Processing of sandwich structures

The basis for sandwich structure manufacturing consists in bonding the core with two stiff skins with the help of pressure to ensure better quality. A complete description can be found in [146, 154, 162].

4.4.1 Skins processing

In the widely used **wet layup technique** (figure 4.5a), a liquid resin is impregnated by hand into fibers with the help of rollers or brushes. After impregnation, the laminates are left to cure under standard atmospheric pressure. This technique is popular because it is simple and low cost and because there is a wide choice of raw materials. However, the homogeneity of resin distribution is difficult to control and the intensive labor makes this technique not suitable for high-volume applications. The **vacuum infusion technique** (figure 4.5b), which consists in introducing a structure into a molding compound and injecting resin to impregnate the fibers by vacuum, produces a better skin quality. This technique can be used for mass production, and the skins have a higher specific strength and stiffness. This technique can be used to produce only sandwich structures with a closed-cell core in order to avoid filling the core with resin. The **pre-impregnated fibers (prepregs)** are another type of skin that can be laminated directly to the core with the help of an autoclave or an oven. A prepreg is a reinforcing fiber which is already pre-impregnated with a resin, being ready to be laminated without the need of additional resin. Generally, the resin matrix in prepregs is partially cured for ease of handling and is stored in a cold place to prevent complete polymerization. This technique allows for

(a) Wet layup technique

(b) Vacuum infusion technique
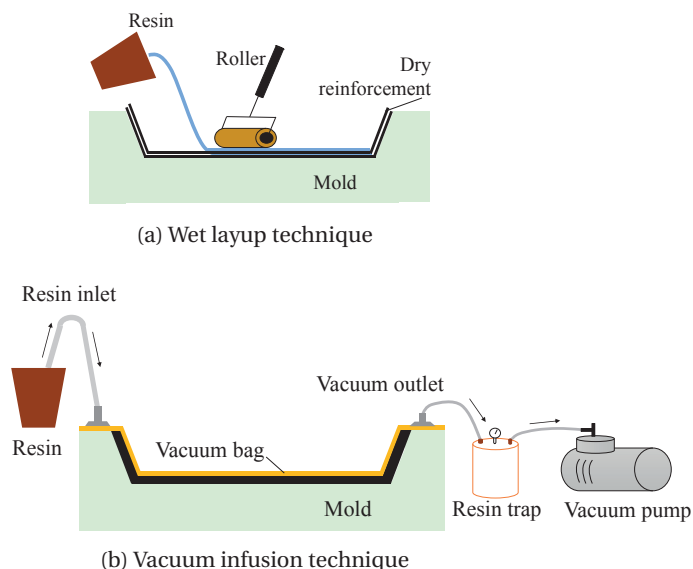
Figure 4.5 – Most-used techniques for preparation of composite: (a) the wet layup technique (also used for manufacturing of sandwich structures) and (b) the vacuum infusion technique.

high-strength properties, good reproducibility and short curing times. However, prepregs have a limited lifetime, must be stored at very low temperatures to avoid curing and have a high cost.

4.4.2 Sandwich processing

The most common processing method to produce sandwich structures is the **adhesive bonding method**. This method consists in placing an adhesive layer between the skins and the core and then subjecting the entire structure to an increase in temperature and pressure as required by the adhesive resin. The bonding process can take place in a vacuum bag (figure 4.5a), an autoclave or a hydraulic press, depending on the application. This technique results in a well-controlled bonding and good mechanical properties. However, it requires intensive labor and often the use of an autoclave — good resin adhesives normally need high temperatures and pressures — both of which increase the cost of manufacturing.

The selection of the best manufacturing methods depends on the type of core, thickness of the skin, type of adhesive, size of the structure to be fabricated and, and of course, cost.
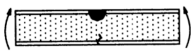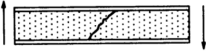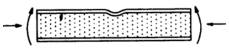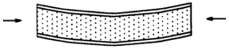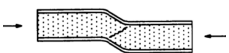
4.5 Sandwich mechanics

4.5.1 Failure modes

Sandwich structure design often integrates sizing and material selection to obtain the mechanical properties required for the defined application. From the mechanical point of view,

stiffness and strength are of major interest during the design. The stiffness can be estimated by using the equations presented in section 4.3. However, the strength depends on the failure mode, which depends on the internal structure of the sandwich as well as the applied load. Table 4.2 lists the failure modes considered during the design of sandwich structures. Each mode sets limits to the load-bearing capacity in a different way, limiting the overall performance of the structure.

Table 4.2 – Illustration and description of the failure modes observed in composite sandwich structures (figures taken from [146]).

Failure mode	Description
Face yield/fracture	Occurs when the skin reaches its maximum allowed stress, whether it be yield or fractured stress, in either tension or compression [163].
Core shear	Occurs when shear stress in the core is higher than its shear strength [164].
Wrinkling	Occurs due to local skin instability, which penetrates the core and forms waves [153, 165–167].
Skin debonding	Occurs due to the presence of out-of-plane loads, in which case shear stress appears in the interface and can lead to debonding, or compression that causes the skin to buckle and debond from the core [168].
Global buckling	Is a general failure which starts being critical at the moment the skins reach their yield strength. If the ultimate load-bearing capacity of the sandwich is reached, the buckled sandwich cannot sustain any more load [146].
Shear crimping	Occurs when a large out-of-plane deformation is applied in a post-buckled state while transverse forces build up due to the deformation [146, 153].
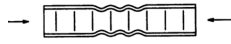
  Face dimpling	Is a typical local instability observed in discontinuous cores (such as a honeycomb) when thin skins are used. This failure can be reversible but might also lead to failure of the skin [169, 170].
  Local indentation	Occurs when a load point is applied. The skin will act as a plane on an elastic support and will bend independently of the opposite skin [164, 171].
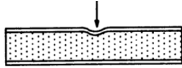
5 Processing optimization of composite sandwich structures

Summary

This chapter proposes a new design for a composite sandwich structure to be used as the backsheet for a lightweight PV module. Our goal is to develop a composite sandwich structure with reduced weight, excellent mechanical stability and durability and that is processable in a simple manufacturing process used in the PV industry. We demonstrate that by selecting a thermoplastic material (ionomer or polyolefin) and a high-thermal-conductivity core (aluminum), we can manufacture a composite sandwich structure in a very short time, using the standard lamination process used in the PV industry. This material combination allows for the production of a polyolefin-based sandwich with a bending stiffness of 15.5 N·m^2 and an ionomer-based sandwich with a bending stiffness of 16.4 N·m^2. These values are equivalent to (and even higher than) the bending stiffness obtained with an epoxy-based sandwich structure (15.5 N·m^2).

The results presented in this chapter are part of a publication entitled *"Light and durable: Composite structures for building-integrated photovoltaic modules"* (see ref. [87]).

5.1 Introduction

As mentioned in Chapter 4, a symmetric composite sandwich structure is composed of two skins bonded to a core by means of an adhesive. Usually, this adhesive is a two-compound liquid, of which compound is a co-monomer responsible for the adhesive cross-linking. It is also possible to find thermoset adhesives in a solid state (adhesive foils, i.e. prepreg) which require storage conditions under negative temperatures to avoid spontaneous cross-linking. Researchers have been working on the development of lightweight PV modules using

these adhesives. In 1995, Carey et al. [172] developed a laminate structure in which solar cells were sandwiched between two fluoropolymer tedlar/silicone and later glued with the help of liquid adhesives onto the composite wings of an airplane. Rion [150] developed an asymmetric photovoltaic sandwich structure comprising one skin made of cells glued with a prepreg to the honeycomb core, allowing for a 20% weight reduction. Keller et al. [173, 174] demonstrated the possibility to include different types of solar cells into a transparent composite frontsheet and a composite sandwich structure backsheet based on glass fiber-reinforced polymer (GFRP) skins and a polyurethane core. This work showed that thin-films are more appropriate for such a PV design due to the brittle behavior and higher thermal coefficient of wafer-based solar cells. Zhang et al. [175] proposed a lightweight structure, in which the solar cells are encapsulated using epoxy and bonded to the upper wing skin. The disadvantages of such thermoset adhesives are the long manufacturing process (curing phases up to 24 h), use of autoclave and high cost of raw materials (especially in the case of prepreg). Besides these disadvantages, sandwich structures are very attractive for high-tech applications, such as aerospace [41], marine [176] and construction [177], due to their excellent mechanical properties (stiffness and strength) at minimum weight. However, they still remain a second option when cost and simplicity of manufacturing processes are primary requirements.

This chapter focuses on the optimization of the manufacturing process of composite sandwich structures by substituting the standard liquid epoxy with a PV adhesive foil. The goal is to propose a composite sandwich design compatible with standard PV lamination best practices while preserving optimal mechanical properties (e.g. high stiffness). The mechanical properties of the sandwich and the adhesive (e.g. bending stiffness, degree of cross-linking) are quantified to evaluate the robustness of the designs proposed.

5.2 Experimental Procedure

5.2.1 Design and fabrication of composite sandwich structures

The composite sandwich structure consists of a stack composed of skin/adhesive/core/adhesive/skin. The skins used are based on a GFRP described in section 2.1. For this study,

Table 5.1 – Elastic and thermal properties of the four selected adhesives. Poisson's ratio is the ratio of the lateral strain to axial strain in an axial loaded specimen [31, 159].

Adhesive Properties	Epoxy	EVA	Ionomer	Polyolefin
Thickness (1 layer), t_{th} [mm]	≤0.05	0.46	0.45	0.10
Young's Modulus, E [GPa]	3.45	0.015	0.057–0.394	0.002–0.235
Poisson's ratio, ν [-]	0.35	0.4	0.45	0.45
Coefficient of thermal expansion, CTE [10^{-6} K^{-1}]	50	270	150–180	35–110

we select two types of cores: a low-thermal-conductivity core (aramid honeycomb), and a high-thermal-conductivity core (aluminum honeycomb); and four types of adhesives: a liquid thermoset as the reference (epoxy), a PV thermoset foil (EVA) and two PV thermoplastic foils (ionomer and polyolefin). Table 2.1 and table 5.1 gives the mechanical and thermal properties of each core and adhesive used in this study. The manufacturing process is optimized according to the type of core and adhesive selected (table 5.2):

- **Epoxy/Vacuum bag process**
  A reference sandwich structure built using epoxy adhesive is manufactured using a wet-layup vacuum bag technique, at room temperature (see figure 2.2).

- **PV adhesive foil/single-step process (s)**
  A sandwich structure built using a PV polymer adhesive foil (EVA, ionomers or polyolefins) in place of the epoxy, manufactured in a simple lamination process (considerably speeding up the manufacturing process).

- **PV adhesive foil/double-step process (d)**
  Again, a sandwich structure built using a PV polymer adhesive but the sandwich is produced in a double lamination process. A first lamination step is performed with the frontsheet close to the heating plate and a second step after flipping the module by 180°. (This process ensures that both adhesive layers in the sandwich have similar processing conditions.)

Table 5.2 – Materials and manufacturing process used for the fabrication of composite sandwich structures. "s" and "d" stand for single and double lamination process, respectively.

Materials		Processing conditions	
Honeycomb core	Adhesive	Vacuum bag	Lamination (min)
Aramid	Epoxy	24h	-
	EVA	-	s11
	Ionomer	-	s11
	Polyolefin	-	s11
Aramid	EVA	-	d11
	Ionomer	-	d11
	Polyolefin	-	d26
Aluminum	EVA	-	s26
	Ionomer	-	s26
	Polyolefin	-	s26

5.2.2 Characterization of the composite sandwich structure (backsheet)

In this section we briefly review the experimental techniques used to characterized our back-sheets (details can be found in Chapter 2) and compliment the technique description with sample information (sample type, number and preparation methods). The results of the material characterization are presented in section 5.3.

Four-point bending test

The bending stiffness (D) and the yield load (P_y) of the composite sandwich structures were characterized using four-point bending tests (test description in section 2.2.7). Samples were manufactured according to the respective choices of sandwich adhesive and core (see table 5.2). For each composite sandwich structure, three to five samples of 25 mm × 220 mm were tested. All tests were performed at room temperature.

90° peeling tests

The adhesion between the sandwich skins and the adhesive was investigated in a 90° peeling test (see section 2.2.5). Samples (25 mm × 170 mm) composed of GFRP/EVA/peel arm were laminated according to the processing guidelines in table 5.2. In order to reproduce the temperature-pressure-time (T-p-t) profile measured during the fabrication of a full module, we kept the same structure represented in figure 5.1, removing the interface GFRP/EVA we wanted to study after lamination. A teflon releasing sheet was inserted into the interface between the EVA and GFRP, functioning as the initiator for the subsequent peeling test. Samples were measured in ambient environment after the encapsulation process without any intentional accelerated aging. For each condition tested, four coupons were evaluated.

Temperature-pressure-time (T-p-t) measurements

During the lamination process, in order to monitor the real process temperature experienced by the encapsulant layers at different positions in the sandwich stack, we manufactured a set of 10 cm × 10 cm coupons embedding two PT1000 temperature sensors. The temperature sensors were placed at the interfaces between the skin and core on each side of the sandwich stack, as shown in figure 5.1. In all coupons, one sensor was in contact with the front skin (i.e. closer to the laminator's heating plate, P_1), and another was in contact with the back skin (farther from the heating plate, P_2). The sensors were connected in a four-wire configuration to an acquisition unit and the temperature was recorded every 10 seconds. Due to the low thermal conductivity of the aramid honeycomb core, a temperature gradient (ΔT) was expected between P_1 and P_2.
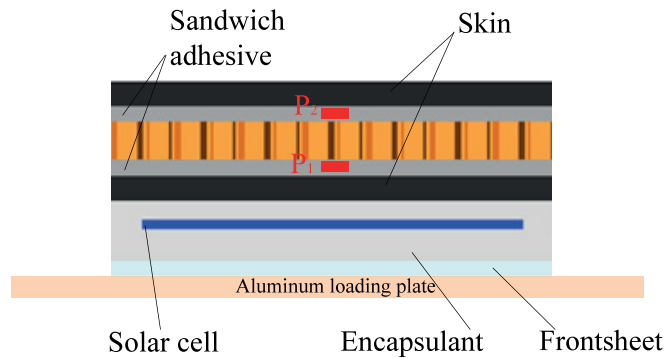
Figure 5.1 – Schematic of a lightweight PV module structure. P_1 and P_2 represent the position of the PT1000 sensors used to record the temperature profiles during the lamination process.

Identification of failure modes

In order to gain insights into the quality of the materials and the processing conditions and to anticipate failure modes that might happen when a module is aged under different thermal aging tests, we produced coupons of 40 cm × 20 cm (the same stack materials presented in figure 5.1). For this study we used always the same frontsheet composed of ETFE, and solar cells were embedded in two layers of EVA encapsulant. Based on the sandwich adhesive used, the ideal processing condition was selected from table 5.2. After lamination, we introduced the samples into a chamber under cyclic temperatures (-40°C to 85°C, more test details can be found in [66] under the *Thermal Cycling Test* section). The test was performed until visual changes were observed.

5.2.3 Adhesive characterization

Differential scanning calorimetry (DSC)

DSC, in the case of thermosetting polymers as EVA, was used to evaluate the degree of cross-linking of the layers at positions P_1 and P_2. The measurements were performed as described in section 2.2.1 and the degree of cross-linking calculated according to equation 2.1. Samples of 10 cm × 10 cm size were manufactured according to structure presented in figure 5.1. A 25-μm-thick ETFE layer was used to protect the encapsulant at position P_1 and P_2 to allow for an easier removal from this layer after encapsulation. After the manufacturing process, 1-mm-thick circular discs were cut from the laminated EVA layer and used for analysis.

Contact angle measurement

This test was performed as described in section 2.2.9 using three sandwich adhesives (epoxy, EVA and polyolefin) and three substrates (GFRP, aramid and aluminum). The contact angle of the EVA and polyolefin polymers were measured after heating the sample to 160°C (maximum

temperature observed during lamination). We obtained a picture of the drop (figure 2.9a) and this image was processed 10 times by the ImageJ drop analysis plugin to evaluate the level of precision on the analysis of a single drop.

5.3 Results and discussion

5.3.1 Quality of the EVA-based sandwich structure

Bending stiffness and peel strength

We first substitute EVA foil for the epoxy adhesive in the composite sandwich structure (reference condition) due to its long durability, its excellent adhesive bonding with glass and backsheets, its cross-linkable properties which do not allow EVA to flow easily under high temperatures (once cured), its low cost, and its status as the most-used encapsulant in the PV industry. For these reasons, we started our study with an aramid honeycomb core and an EVA adhesive using a single lamination process to bond the different layers of the backsheet.

Figure 5.2a shows the four-point bending load-displacement curves for sandwiches prepared with epoxy (reference sandwich sample) and EVA. The bending stiffness of the epoxy-based reference sandwich is 15.5 N·m^2, exhibiting *shear crimping* as a failure mode after the four-point bending test. This failure suggests that there is a good stress transfer from the skins to the core (see section 4.5.1 for a review of the main failure modes of composite structures). Moreover,

(a) Four-point bending test   (b) 90° peel test
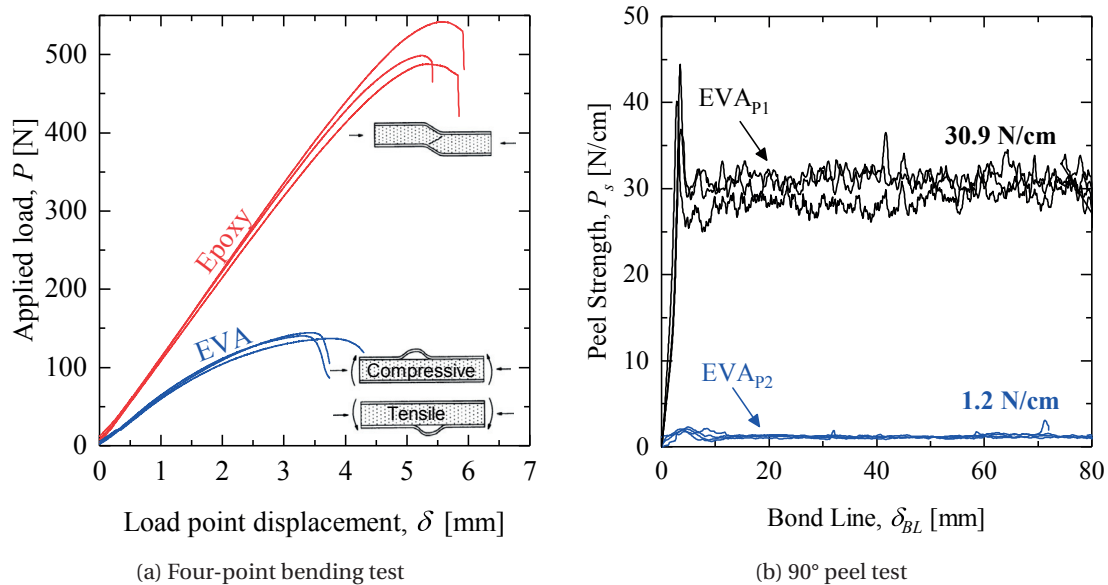
Figure 5.2 – (a) Load-displacement curve from four-point bending tests of sandwiches made with epoxy adhesive and EVA single lamination and (b) peel strength of the interface EVA/skin in position P_1 and P_2.

this value is close to the bending stiffness calculated by conventional beam theory predictions (17.6 N·m^2). The bending stiffness for the sandwich glued with EVA is about 8.5 N·m^2, much lower than the value obtained with epoxy. Additionally, we observe a different failure mode with *skin debonding*. This failure mode occurs when the interfacial adhesion between a sandwich's adhesive and skins is low. Moreover, the skin delamination always affects the interface that is more distant from the heating plate during the lamination process (position P_2), regardless of whether the interface is loaded in tension or compression mode.

Figure 5.2b shows the results obtained during peeling tests between the EVA adhesive and the skin. Peel strengths of 30.9 N/cm and 1.2 N/cm were obtained in positions P_1 and P_2, respectively. The very low adhesion at P_2 explains the delamination of the back skin during the four-point bending test. However, this low peel strength is not a sufficient explanation for the measured low bending stiffness. This may be attributed to the low mechanical properties of EVA due to its weak intrinsic Young's modulus (as compared to epoxy) or to inappropriate lamination guidelines leading to partial EVA cross-linking.

To evaluate the material selection, we introduce the composite sandwich structure made with EVA adhesive and aramid core to cyclic temperatures (-40°C to 85°C, as described in the thermal cycling test in *IEC 61215*). The epoxy-based module did not show any visual change; however, the EVA-based module started to show bending towards the cell side after only 10 days. Due to the high CTE of the frontsheet materials (ETFE/EVA), significant internal stress built up when the sample was stressed with thermal cycles. As seen from the four-point
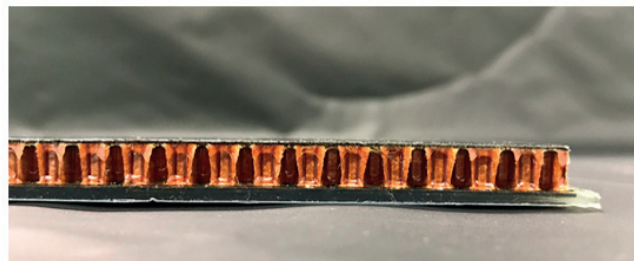
(a) Epoxy
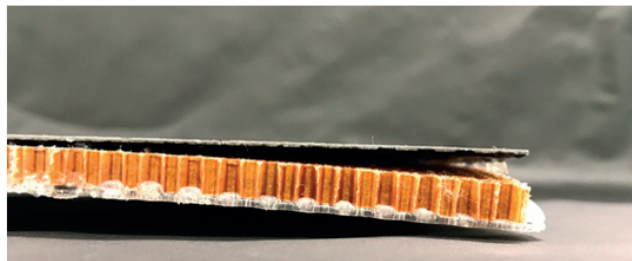
(b) EVA

Figure 5.3 – Visual inspection of composite sandwich structures produced with (a) epoxy and (b) EVA after subjecting the samples to thermal cycles (50 days in a chamber with cycles in temperature from -40°C to 85°C).

bending test, the EVA/aramid-based sandwich was not stiff enough to resist the thermal stress built during the thermal cycling on the module frontsheet, resulting in a visible deformation of the module and, consequently, delamination (see figure 5.3). These deformations do not induce cell damages, but they should be avoided to ensure long-term performance of the devices. Further, according to *IEC 61215*, the visual appearance of the module should be unchanged after each stress test. These results confirm that the sandwich backsheet structure processed with EVA has poor mechanical properties and low mechanical stability. To investigate delaminations occurring on the back skin, we monitored the lamination temperature profile of our adhesive on the two sides of the core during a standard lamination process.

Cross-linking degree of EVA interlayers

Figure 5.4 shows the temperature profiles of the EVA layers recorded during a standard lamination process for both a glass-glass configuration and the lightweight design configuration. As expected, the T-p-t profiles are different in positions P_1 and P_2. During the preheating stage, the temperature at P_2 increases faster than the temperature at P_1, due to the fact that the laminator's silicone membrane that is used to apply pressure is not yet under vacuum and is in contact with the top of the sample. During the curing stage (i.e. once the pressure is applied), a considerable difference in temperature between P_1 and P_2 is observed. The front skin (close to the heating plate, P_1) reaches 153°C at the end of the curing process, a temperature even higher than the glass-glass reference sample. In contrast, at the end of the process, the back skin (P_2) reaches a temperature of only 106°C. This temperature is higher than the melting point of the EVA, but lower than the temperature needed to activate the
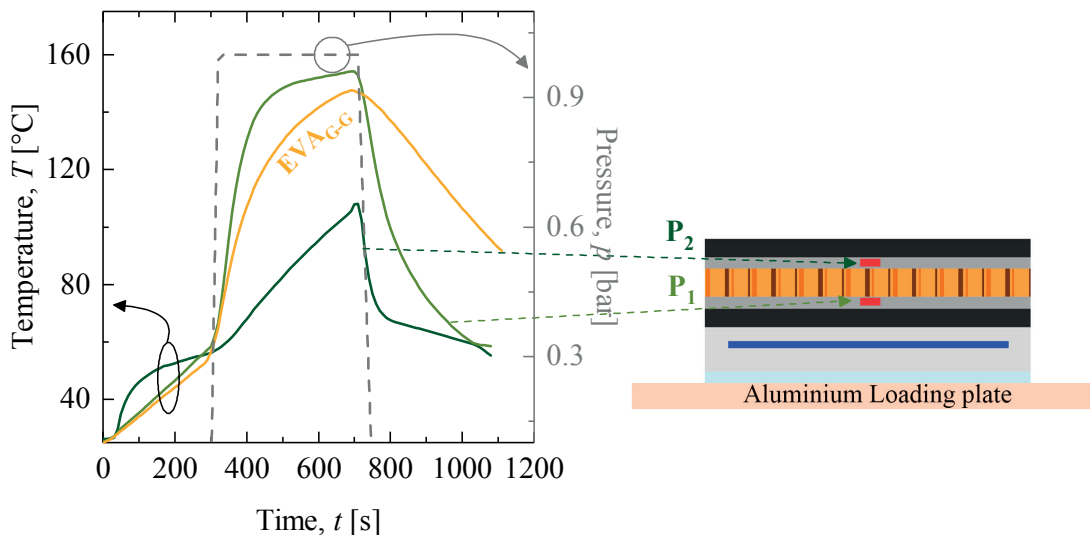
Figure 5.4 – T-p-t profiles, as measured during a standard lamination process by introducing PT1000 sensors on both sandwich skins. A reference profile for a sensor laminated in a glass-glass (2 × 3.2 mm) module architecture is also plotted.

peroxide decomposition, responsible for the reticulation of EVA (between 110 and 130°C). Figure 5.5a shows the DSC evaluation of the cross-linking degree for layers processed in a single lamination run. We recognize from the DSC thermograms that the cross-linking degree at P_1 and P_2 are only 76% and 1%, respectively, meaning that in both adhesive layers the EVA has a cross-linking degree below the 80% threshold usually reported as a standard value. These results explain the lower bending stiffness exhibited by the sandwiches processed with EVA as the gluing material, when compared to reference process with epoxy.

5.3.2 Improving quality of the composite sandwich structure

In the previous sections we showed that the EVA layer localized in P_2 (i.e. the skin farther from the heating plate) is processed at very low temperatures (106°C), and consequently the EVA is not well cross-linked, it is not stiff enough to provide good stress transfer between skins and core, and the adhesion between the top EVA and skin is very low. In order to improve the sandwich quality, we explored three main possibilities:

- **Change the processing conditions**
  Double lamination will ensure that both EVA layers will present similar properties on top and bottom and that the cross-linking degree will approach the 80% value.

- **Choose a different encapsulant**
  A better sandwich glue more compatible to a single lamination process, stiffer than EVA, which does not show problems during curing. Polyolefins and ionomers are good candidates.

- **Change the sandwich core**
  Choosing a material with a higher thermal conductivity will enhance the process conditions seen by the EVA layer at position P_2. Aluminum honeycomb is a good candidate.

A. Double lamination process

To increase the cross-linking degree of the EVA in position P_2, we performed a double-step process. The first lamination step was performed with cells (and the frontsheet) close to the heating plate; the second one after flipping the module by 180°, ensuring that the two polymer layers used to glue the skins to the core to experience — as much as possible — identical process conditions. The goal of this double lamination process is to evaluate the full potential of EVA by trying to reach a uniformly and satisfactory ($\geq$ 80%) degree of cross-linking on both adhesive layers. DSC scans performed on double-laminated EVA layers confirm that both layers in the sandwich are well cross-linked after double lamination (see figure 5.5a). The initial low cross-linking degree of EVA increases to 87% and 96% at P_1 and P_2, respectively. This increase in cross-linking leads to an increase in adhesion between the skin and adhesive as figure 5.5b clearly indicates. Indeed, the failure mode observed with a double

(a) DSC measurements

(b) 90° peel test
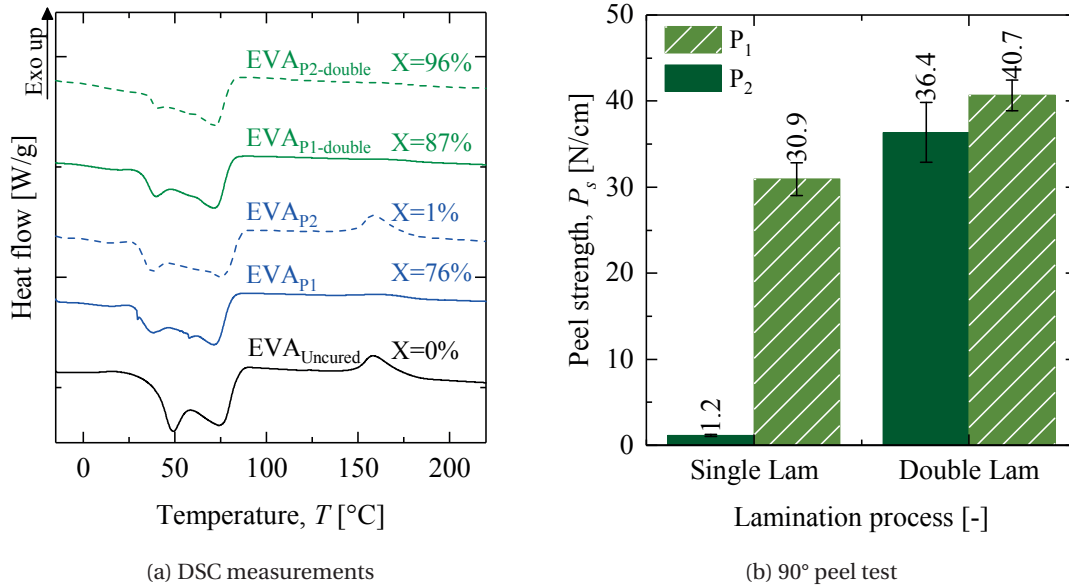
Figure 5.5 – (a) DSC scans for EVA laminated at position P_1 and P_2 and in single and double lamination processes. As a reference, the DSC profile of an uncured EVA is also plotted. (b) The peel strength of the EVA/skin interface in position P_1 and P_2.

lamination process is shifted from skin debonding to *shear crimping* of the core, indicating a clear improvement of the sandwich stability.

However, even if the stiffness of the sandwich obtained in a double lamination process (9.9 N·m^2) improves by 16% when compared to sandwiches processed in a single lamination step, this value is still lower than that of the epoxy reference sample (15.5 N·m^2). To evaluate whether this gain in bending stiffness is sufficient to pass the thermal aging tests without mechanical deformations, we manufactured samples using EVA and a double lamination process (frontsheet made of ETFE/EVA) and subjected them to temperature cycles (for 50 days). From the visual inspection, we identify a tendency of the front skin to bend slightly toward the frontsheet, though less pronounced, even if no complete skin delamination occurs (figure 5.6). A bending of 2 mm is measured at the center of the structure (over a length of 40 cm). This bending occurs due to polymer softening since a very small percentage of EVA is not cross-linked and can still flow, happening now at position P_1 (local where cross-linking degree is lower). The sandwich stiffness is now limited by the intrinsic low elastic properties of the EVA adhesive layers. Moreover, in view of simplifying the manufacturing process, we aim at avoiding the need for a double manufacturing step. For this reason, replacing EVA with an encapsulant material exhibiting a higher intrinsic stiffness and showing less sensitivity to the processing conditions will help to reduce the manufacturing time.
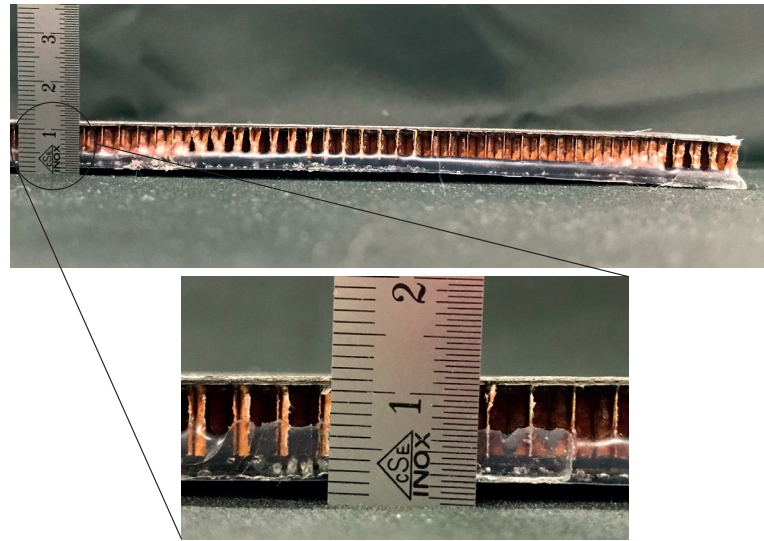
Figure 5.6 – Visual inspection of composite sandwich structure laminated with EVA adhesive in a double lamination process. A bending of 2 mm is measured at the center of the 40-cm-long module.

B. Alternative adhesive for sandwich structure: thermoplastics

Thermoplastics are good candidates to replace EVA as sandwich adhesive thanks to their higher Young's modulus and thermoplastic behavior, eliminating the need for cross-linking. For this study, we selected two thermoplastics: ionomer and polyolefin. These two polymers are used to fabricate new sandwich structures using both single and double lamination processes.

In four-point bending tests, the bending stiffness of the sandwiches manufactured in a single lamination process using ionomer, increases to 11.6 N·m^2 (figure 5.7). However, we still observe *skin debonding* as failure mode of the backsheet. The adhesive layer farther from the heating plate (P_2) does not reach the temperature required to achieve a high wettability, thus we obtain a poor adhesion between the core and adhesive and between the skin and adhesive. This is confirmed by the peel strength measured on both surfaces: 44.8 N/cm and 7.13 N/cm at position P_1 and P_2, respectively. For the polyolefin adhesive, the single lamination process is to short to produce a composite sandwich structure, mainly due to the high melting point of the adhesive. After the single lamination process, the top skin (position P_2) could be easily peeled by hand.

By applying a double lamination process, however, the mechanical properties of the backsheet sandwich improve considerably. The samples using an ionomer adhesive, show a change in failure mode from skin debonding to *shear crimping* and a remarkable increase in bending stiffness of up to 14.2 N·m^2, approaching the stiffness of the epoxy reference (15.5 N·m^2). For the sandwich made with polyolefin, we increased the processing time (see table 5.2) to ensure that the adhesive could reach a minimum viscosity, enough to allow for a good weatabillity between the skin and core. The composite sandwich structures using polyolefin and processed
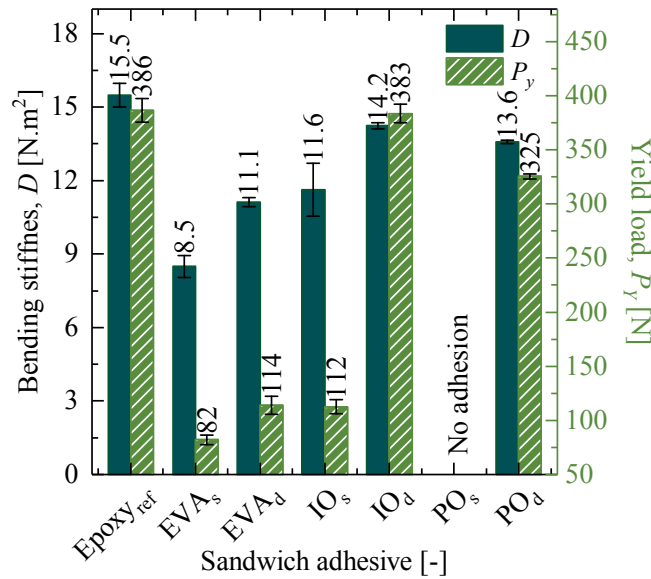
Figure 5.7 – Bending stiffness and yield load for composite sandwich structures glued with different PV polymer foils in a single (s) and double (d) lamination process. The polyolefin-based sandwich laminated in a single lamination process does not show any adhesion between the encapsulant and skin localized at position P_2.

with double lamination process also show a high bending stiffness (13.6 N·m^2) approaching our epoxy reference value.

The disadvantage of using thermoplastic adhesive with an aramid honeycomb core is that, due to the high melting temperature of the thermoplastic polymers (between 80 and 110°C), the full PV module production still requires a double lamination process to bond the adhesive sufficiently well to both core/skin interfaces. The relatively high thickness of the aramid core (≈ 6 mm) introduces a considerable temperature gradient between the two skins during the lamination process, which negatively affects the adhesive properties of the interface farther from the heating plate. The double lamination process would take 22–52 min with these thermoplastic foils, which is long (especially with polyolefin-based sandwiches), and it is not convenient to flip the module, in view of an industrial application of the product.

C. High thermal-conductive core: aluminum core

In order to reduce the manufacturing process time of our lightweight PV module, a new core material is needed to replace the aramid core. We considered three main requirements during the selection of a new material: the thermal conductivity, the availability on the market, and the cost. Besides its higher density (77 kg/m^3) when compared to aramid (48 kg/m^3), the aluminum honeycomb seems very promising: its thermal conductivity is 100% higher (3.9 W/m·C) [146], and it is 50% cheaper than the aramid honeycomb (details about cost can
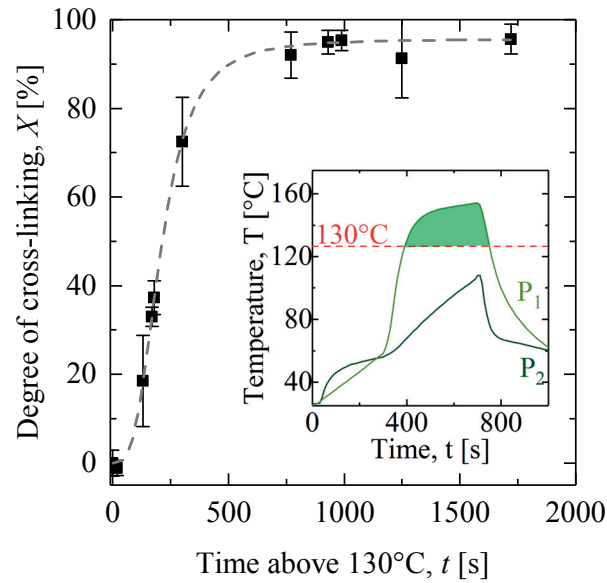
Figure 5.8 – Degree of EVA cross-linking as function of the time the adhesive stays above 130°C (temperature at which peroxide consumption starts). This time is taken from the temperature profiles recorded during the lamination process.

be found in section 2.1).

Previously we showed that, even fully cured, the mechanical properties of the EVA-based sandwich structure are not sufficient to prevent deformation under thermal stress. However, we decided to keep this adhesive to study the influence of the aluminum core because (i) its cross-linkable properties are preferred to avoid flowing at high temperatures, and (ii) the aluminum core's mechanical properties are higher than those of the aramid core, so this extra rigidity in the core might be enough for the EVA-based sandwich to increase stiffness and reduce bending/twisting during thermal cycles tests. In order to correctly select the manufacturing process for the EVA adhesive, we performed a study where the cross-linking degree is related with the time that the adhesive spends above 130°C (highest temperature required for the peroxide activation). Figure 5.8 shows that, by targeting a minimum of 80% degree cross-linking, the adhesive must stay above 130°C for a minimum of 400 s (similar to the time needed in a glass-backsheet module lamination). These processing guidelines are also used to manufacture the sandwich structures made of thermoplastic materials.

Figure 5.9 shows the bending stiffness of the composite sandwich composed of an epoxy adhesive and an aramid core (reference condition), and the different PV adhesive foils with an aluminum honeycomb core. The EVA-based sandwich structure shows a bending stiffness of 10.4 N·m^2, much lower than the bending stiffness of epoxy (15.5 N·m^2). These results show that, even if the use of an aluminum core considerably improves the lamination time,
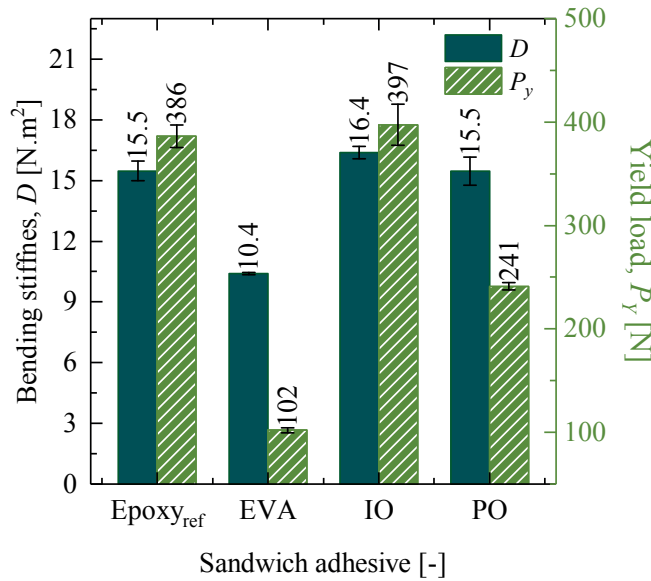
Figure 5.9 – Bending stiffness and yield load of (i) epoxy/aramid-, (ii) EVA/aluminum, (iii) ionomer/aluminum-, and (iv) polyolefin/aluminum-based sandwich structure. Sample (i), (ii), and (iii) are manufacture in a single lamination process.

the intrinsic properties of EVA do not allow the sandwich backsheet stiffness to be as high as the value measured for our reference. As observed by visual inspection of the sandwich manufactured with an aramid honeycomb core (see figure 5.6), this low bending stiffness will not be enough to resist the thermo-mechanical stress induced by the frontsheet dilatation and shrinkage during temperature cycles. On the other hand, sandwich structures manufactured with ionomer or polyolefin show the same (or even higher) bending stiffness as our epoxy reference: the bending stiffness measured on the aluminum core is 15–40% higher than the values obtained with the aramid core in a single lamination process. This is due to the fact that the aluminum core has a better resistance in shear than the aramid core (details in section 2.1). These two promising solutions (ionomer- and polyolefin-based sandwich structures) will be further considered to understand their thermo-mechanical behavior under different aging tests.

Looking at the lamination profile for a laminated composite sandwich structure with the two core types (figure 5.10), we can clearly see the advantages of using a high-thermal-conductivity core. In the case of a laminated composite sandwich structure with an aramid core, we measure a maximum ΔT of 47°C between the two skins of the composite. The presence of an insulating material (aramid core) hinders the heat transfer from the bottom adhesive (P_1) to the top adhesive (P_2). Consequently, a double lamination process is needed to ensure that both adhesives have similar mechanical properties after processing. In the case of an aluminum core, the thermal conductivity is high enough so that the adhesives located at P_1 and P_2 are exposed to almost the same lamination temperature. The presence of the aluminum core
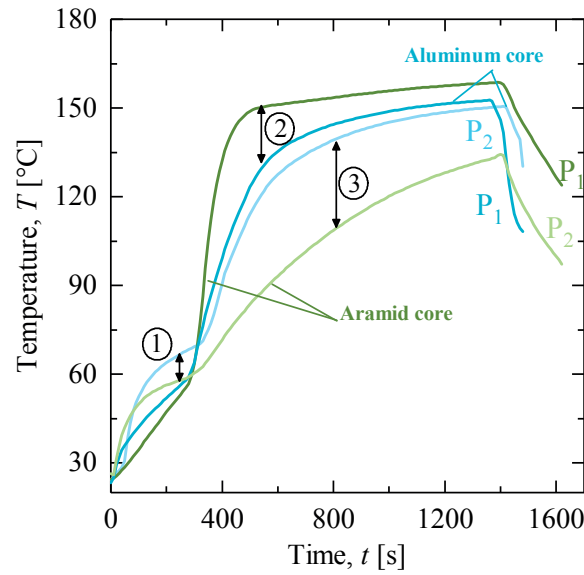
Figure 5.10 – Adhesive temperature measured during lamination process using an aluminum and aramid core: (1) high temperature at position P_2 during preheating phase, (2) layer at position P_1 has a lower temperature due to heat transfer through the core towards the layer at P_2, and (3) higher temperature at layer P_2.

provides three benefits: (1) a more efficient heat transfer from the top layer to the bottom layer during the preheating phase, (2) the layer in P_1 has a lower temperature due to heat transfer through the core towards the layer at tP_2, and (3) better heat transfer through the core material enables the back layer to reach a higher temperature.

5.3.3 Contact angle measurement

During the design of composite sandwich using honeycomb cores, it is important to analyze the contact angle in between adhesive and skin and the adhesive and core, to evaluate whether the adhesive flows and attaches well to the substrate. The adhesive strength of a macroscopic interface depends mainly on:

- The **chemical compatibility** between the adhesive and substrate. Low contact angles are obtained when chemical compatibility is high.

- The **meniscus surface area**. A large adhesive fillet between the honeycomb core cell walls and skins will lead to high adhesion. Different studies demonstrate the importance of meniscus formation showing that a bigger adhesive fillet absorbs more energy during delamination [178], large and regular-shape adhesive fillets lead to higher debonding energies [179], and the size and the quality of the adhesive fillet (e.g. porosity) influence the debonding energy [180, 181].
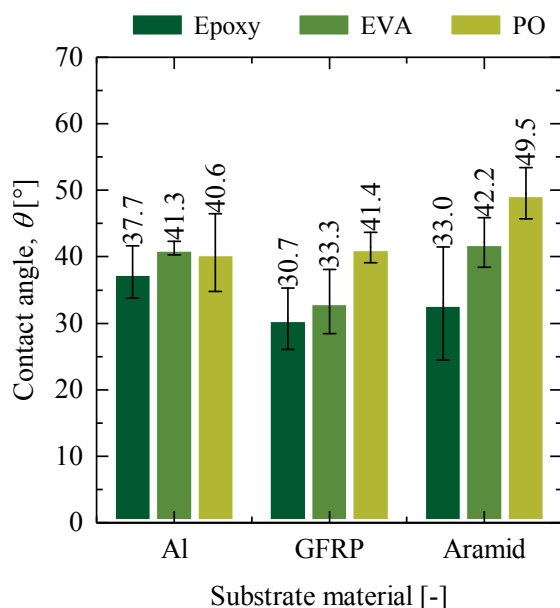
Figure 5.11 – Contact angle measurement between adhesives (epoxy, EVA, polyolefin) and different sandwich components (skins, aluminum, aramid). Contact angles measured between the thermoset adhesives and the different substrates are obtained after full polymer curing and between the polyolefin and the substrates obtained at 160°C.

Even with a good chemical compatibility, with a low contact surface area, the overall adhesion will be low.

Figures 5.11 and 5.12 show the contact angle and microscopic images of three different adhesives in contact with both skin and core materials, respectively. Thanks to the high chemical compatibility of epoxy, this adhesive shows the lowest contact angle (in the range of 30.7–37.7°), providing a good wettability with the different surfaces (GFRP skins, aluminum and aramid core). In the case of EVA and polyolefin, the adhesives are in a form of foil (at room temperature) thus, the polymers are first melted to reach similar viscosity to what is obtained during lamination process. Indeed, the measurement of the contact angle shows that in all cases its value is << 90° (contact angles are in the range of 30–40° and 40–50° for EVA and polyolefin, respectively). Despite the fact that the contact angle values measured for EVA/PO are higher than the those of epoxy reference, the analysis of the meniscus of the polyolefin shows a good surface contact with aluminum and aramid core. The microscope images show that a good adhesive meniscus was created with the polyolefin (similarly to what is obtained with epoxy adhesives) but not with the EVA. These two measurements together show that, thanks to the reduced contact angle and large contact surface area, polyolefin is well distributed inside the honeycomb core and it has a good chemical compatibility. These results suggest that the processing conditions used for polyolefin are good enough to provide good adhesion strength.

Polyolefin   EVA   Epoxy
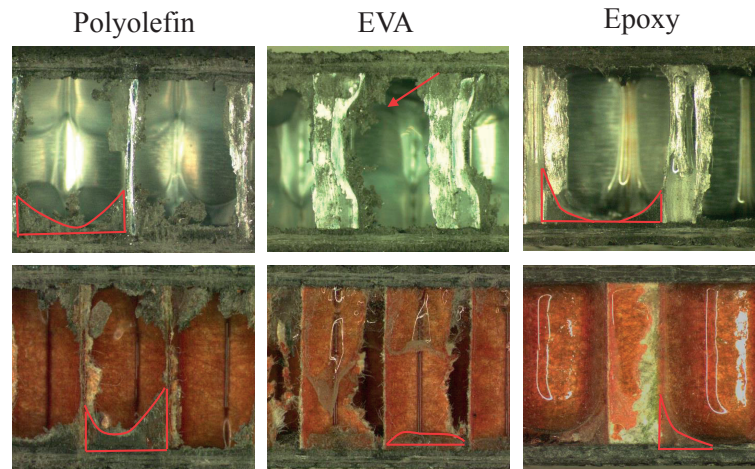
Figure 5.12 – Microscopic images of the adhesive meniscus in different composite sandwich structures. The red outlines represent the meniscus surface area for each sandwich type.

5.4 Conclusions

Epoxy liquid materials are the preferred adhesive to produce composite sandwich structures thanks to their reduced cost and easy handling. However, vacuum bag techniques are not compatible with PV module production. In this chapter we studied the use of alternative sandwich adhesives to enable manufacturing of a lightweight PV module using standard PV lamination process. With this in mind, we evaluated the following possibilities to substitute for the standard epoxy adhesive:

1. Using **ethylene-vinyl acetate (EVA) foil** as the adhesive

   Single lamination process – The EVA-based sandwich processed in a single lamination PV process exhibited low bending stiffness (8.4 N·m^2) and showed skin delamination during the bending test or when the sandwich was subjected to temperature stress (e.g. thermal cycling). DSC scans and temperature profiles acquired during the lamination process showed that the skin delamination, the low mechanical properties and the poor adhesion between the adhesive and skin were due to the low degree of cross-linking of the EVA layer positioned farther from the heating plate (P$_2$).

   Double lamination process – The EVA-based sandwich processed in a double lamination PV process enables heating at similar temperatures both backsheet's skins. With this process we were able to fully cross-link all EVA layers present in our lightweight PV module. The sandwich stiffness hence increased to 11.1 N·m^2. However, after cyclic temperature tests, the sandwich still tended to bend towards the frontsheet, due to the low stiffness of the composite sandwich structure.

2. Using **thermoplastic (ionomer and polyolefin) foils** as the adhesive

Single lamination process – The ionomer-based sandwich reached a bending stiffness of 11.6 N·m^2. However, we still found that skin delamination occured under load. In the case of the polyolefin-based sandwich, no adhesion was observed between the skin and adhesive at position P$_2$. These behaviors were due mainly to the higher melting temperature and higher viscosity of thermoplastic polymers when compared with EVA, making them difficult to laminate in a single lamination process when a non-conductive core is used.

Double lamination process – By performing a double lamination, we increased the bending stiffness to 14.2 N·m^2 and 13.6 N·m^2 for ionomer and polyolefin, respectively, approaching the bending stiffness measured for the epoxy reference. From the mechanical properties measured, these materials and manufacturing process hold promise for the production of a glass-free lightweight PV module.

3. Using **thermoplastic (ionomer and polyolefin) foils** with a **high-thermal-conductivity core**

Single lamination process – Combining the higher stiffness of the thermoplastic adhesives with a high-thermal-conductivity core (aluminum honeycomb core) we improved the heat transfer from one skin to the other, and reduced the manufacturing time. This material combination allowed for the production of a sandwich structure with a bending stiffness of 15.5 N·m^2 and 16.4 N·m^2 for the polyolefin- and ionomer-based sandwich, respectively.

From this study, we selected two promising structures: the structure made of EVA / ionomer / polyolefin) and an aramid honeycomb core manufacture in a double lamination process and the structure made of EVA / ionomer / polyolefin and an aluminum honeycomb core manufacture in a single lamination process. We decided to keep EVA because is the widely used polymer within PV industry. We selected these two structures to evaluate the thermo-mechanical stability of glass-free lightweight PV modules, presented in the next chapters.

6 Environmental reliability of lightweight PV modules

Summary

This chapter discusses the reliability of the composite sandwich structures under accelerated-aging tests and at high temperatures. We demonstrate that EVA- and ionomer-based sandwich structures show a low bending stiffness at high temperatures due to their low storage modulus at 80°C, which limits their sandwich mechanical stability. We also show that the ideal composite sandwich — to improve mechanical stability — is a polyolefin-based sandwich structure with an aluminum core thanks to the high storage modulus of polyolefin adhesive at elevated temperatures and the simple manufacturing process provided by the better heat distribution when a heat-conductive core is used. The latter structure is used to manufacture two-cell modules that are aged using industry standard qualification testing (*IEC 61215*), by applying different climatic, mechanical and electrical stress, in order to investigate their durability properties. The optimized solution is scaled up to a sixteen-cell module which successfully passes a pre-qualification test sequence (Sequence C, Sequence D and Sequence E of the *IEC 61215*).

The results presented in this chapter are part of a publication entitled *"Thermo-mechanical stability of lightweight glass-free photovoltaic modules based on a composite substrate"* (see ref. [88]).

6.1 Introduction

PV modules are subjected to high-stress conditions when installed outdoors: external mechanical loads (wind/snow), humidity, UV, hail and temperature cycles. In addition to these challenges, BIPV elements can be exposed to relatively high module operating temperatures

(OT) [182]. The module OT depends on different factors, among which the mounting configuration, incident sunlight and module packaging are the most important ones [72, 183–185]. Usually, BIPV modules are fully integrated into the building envelope with no ventilation from the rear side and can reach operating temperatures as high as 86°C on a sunny summer-day in Europe. In contrast, a ventilated, rack-mounted module in the same location on the same day would have an operating temperature 20°C cooler, as reported in [72] (see Table 6.1). Moreover, according to the guideline *ETAG 002* [186], 80°C can be considered a temperature limit for practical purposes in civil engineering. Such high operating temperatures are known to accelerate the degradation rates of PV modules [68, 86, 118, 185, 187] and, consequently, may pose a threat to the long-term stability and performance of BIPV devices.

Table 6.1 – Maximum operating temperatures for a glass-backsheet module on a sunny, cloudless day in three different configurations: open rack fixation, building-added PV (BAPV) and building-integrated PV (BIPV).

Mounting configuration	OT on a sunny, cloudless day [°C]
Open-rack	64
BAPV	72
BIPV	86

The composite sandwich structures presented in the previous chapters are the key component of a glass-free lightweight PV module: they must provide electrical insulation, rigidity and mechanical stability over more than 25 years in an outdoor environment. In order to assess their long-term stability, it is very important to quantify their mechanical properties under real operating conditions (close to the real module OT) and after accelerated-aging tests. Having identified the ideal composite sandwich backsheet, we manufactured a two-cell PV module and we investigate its thermo-mechanical stability by performing different aging tests, such as thermal cycling, damp heat, humidity freeze, hail test, mechanical load test and potential-induced degradation [66, 80].

Potential-induced degradation

Potential-induced degradation (PID) is a critical degradation mode for c-Si-based solar modules that has received attention in recent years as it can reduce the power output in a rapid and severe way [188]. PID occurs due to the migration of sodium (Na^+) ions from the glass, or other elements of the module, towards the semiconductor material, when the modules or cells are exposed to a negative voltage compared to ground. PID depends on the module and cell technology, encapsulant resistivity and system design [86, 189–191]. At the moment, this test is not present in the *IEC 61215*; however, in our glass-free lightweight PV module, the presence of an aluminum core can pose an additional threat. If the core is not properly insulated, it may contribute to an increase of the potential difference within the module materials and,

consequently, to a stronger electric field that might promote migration of ions between the semiconductor material and other elements of the module. To understand the stability of this new design with regard to this degradation mode, we submitted the lightweight modules to a PID test (*IEC 62804*) and compared the results with a standard glass-backsheet module produced with the same type of solar cells, encapsulant foil and interconnections.

6.2 Experimental procedure

6.2.1 Material characterization methods

Sandwich adhesive characterization

Three sandwich adhesives were studied and compared to the reference condition processed with epoxy adhesive: ethylene-vinyl acetate (EVA), ionomer, and polyolefin. These polymers were laminated in the standard lamination process and characterized by differential scanning calorimetry (DSC) and rheology, as described in sections 2.2.1 and 2.2.2, respectively. DSC allows us to derive the glass transition temperature (T_g) and melting temperature (T_m) [192, 193]. The rheology measurements are performed to obtain the storage modulus in shear (G') and dynamic viscosity (η').

Skins mechanical characterization

The skins of the composite sandwich were fabricated using UD E-glass fiber in a $[0/90]_s$ configuration (more details can be found in section 2.1). We used a tensile test to assess their Young's Modulus (E) and Ultimate Tensile Strength (σ_{UTS}), as presented in section 2.2.6. Tests were performed at room temperature, at 80°C and on aged samples (after damp heat and thermal cycling). The tests were performed on specimens on 250 mm in length, 25 mm in width and 0.7–0.8 mm in thickness. The tensile test specimens were prepared by bonding four aluminum tabs to the specimens' edges, resulting in an available area of 160 mm^2 for testing (see figure 2.7). Dynamic mechanical analysis (DMA) was performed on a set of three different specimens 45 mm × 10 mm × 0.7 mm after manufacturing and after being aged. The test was performed according to section 2.2.3 and was used to obtain the temperature-dependent viscoelastic properties of the skins, i.e. storage (E') and loss (E'') modulus, and the glass transition temperatures for the cured skins. The T_g of the skins is identified as the DMA onset value on the storage modulus curve ($T_{g,onset}$), used as reference in guidelines for structural FRP design [102]. The E' obtained by DMA can be correlated to the G' obtained by rheology, using equation 6.1, where v represents the Poisson's ratio:

$$E' = 2(1 + v) \cdot G' \tag{6.1}$$

Sandwich mechanical characterization

The composite sandwich structures were manufactured using the different adhesives previously presented (EVA, ionomer, polyolefin and the reference epoxy), the skins and two cores: a low-thermal-conductivity core (aramid honeycomb) and a high-thermal-conductivity core (aluminum honeycomb). The manufacturing process depends on the respective choices of sandwich adhesive and core, as already stressed in the previous chapter. Based on the results presented in Chapter 5, we selected a double lamination process for the aramid core and a single process for the aluminum core. Details about the processing can be found in table 5.2. The bending stiffness and the yield load of the composite sandwich structures were measured using four-point bending tests, as described in section 2.2.7. The mechanical properties of the composite sandwich structures aged in thermal cycling and damp heat were measured 24 h after removal from the aging test. Four-point bending tests were also performed at 80°C using a climatic chamber directly on the tensile testing equipment with a temperature resolution of ±0.1°C. Tests were performed using a 50 kN load cell. Specimens were kept at constant test temperature for at least 30 min before the test started. The goal of this test is to assess the bending stiffness at an operating temperature that a BIPV module might reach.

6.2.2   Module manufacturing, aging and characterization

Based on the most promising backsheet structures (polyolefin/aluminum-based backsheet), two-cell modules (20 cm × 40 cm) were manufactured. The module's frontsheet is composed of conventional c-Si solar cells (aluminum-back surface field, Al-BSF, or passivated emitter rear cell, PERC) with three or five busbars encapsulated in EVA and covered by an ethylene tetrafluoro-ethylene layer (ETFE from Saint Gobain). The full module stack is shown in figure 6.1. A glass-backsheet module was also produced as a reference: it consists on a 3-mm-thick solar-grade soda-lime glass at the front and a 0.36-mm-thick polyethylene terephthalate (PET) backsheet from Dunmore (PPE[+]). The solar cells and the protective encapsulant are the same in both cases. Lightweight modules were manufactured according to table 5.2 and the glass-backsheet modules were manufactured with a standard lamination process as represented in figure 1.6. After manufacturing, the modules were subjected to aging tests described in *IEC 61215-2:2016*: thermal cycling, damp heat, humidity freeze and the potential-
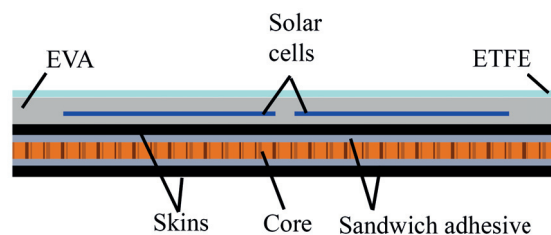
Figure 6.1 – Schematic of the layers of the glass-free lightweight PV module.

induced degradation present in *IEC 62804*, which are described in table 1.2 and in section 2.4. Electrical characterization of the modules was performed at standard test conditions (STC) by means of current-voltage (I-V) measurement and electroluminescence (EL) imaging to visualize damages affecting the module power as described in section 2.3.1 and 2.3.2. Moreover, a careful visual inspection was performed to identify visual changes (such as yellowing, delamination or bending).

We selected the most promising lightweight design configuration and scaled it up to a sixteen-cell module as represented in figure 6.2 (81 cm × 81 cm). The same manufacturing guidelines were used. To provide a pre-qualification to our new design, we followed different test sequences required in [66]: Sequence C, Sequence D and Sequence E (see figure 1.10 for detailed explanation about the test sequence).
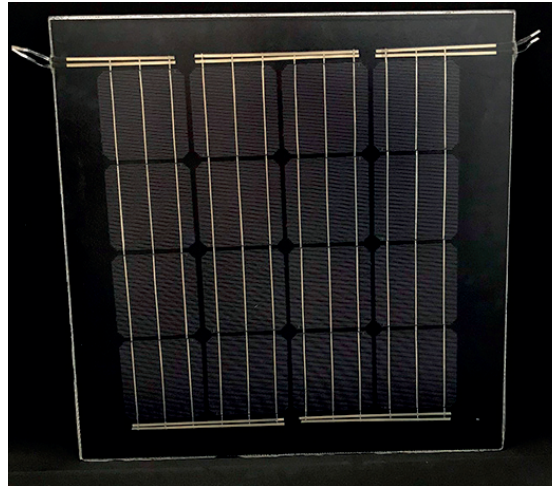
Figure 6.2 – Sixteen-cell glass-free lightweight module developed to study stability under accelerated-aging tests (thermal cycling, damp heat, mechanical load test).

6.3 Results and analysis

6.3.1 Stability of the individual composite sandwich components

To evaluate the stability of the composite sandwich structure we assess the behavior of each sandwich component individually by establishing the stiffness of the different sandwich adhesives at different temperatures, and evaluating the mechanical stability of the skins after each accelerated-aging or high-temperature test.

A. Sandwich adhesive

Table 6.2 and figure 6.3 show the results obtained by DSC and rheology measurements. These results demonstrate that the ionomer and EVA have a low melting temperature of 84°C and

Table 6.2 – Summary of thermo-mechanical properties measured for all types of adhesives used to produce the composite sandwich structure.

Adhesive	T_g [°C]	T_m [°C]	G' at 30°C [MPa]	G' at 80°C [MPa]
EVA	-28	70	0.31	0.14
Ionomer	50	84	12.98	0.75
Polyolefin	-	110	18.77	2.97
Epoxy	53	-	1242	1.72

70°C, respectively. The fact that EVA is cross-linked causes the polymer not to melt completely (only the amorphous fraction of the non-reticulated volume can still melt). However, EVA shows the lowest G' of all polymers at 80°C, with only 140 kPa. The G' of the ionomer decreases constantly as the temperature rises; it can melt and solidify above or below T_m. The ionomers contain ionic segments attached to the bulk polymer-forming clusters that act as reversible cross-links [194, 195]. The high chemical reactivity of these ionic groups increases the number of bonds between the polymeric chains, which increases the material stiffness and strength [196]. However, the ionic bonds lose their attraction in the presence of heat, showing a lower resistance to loads. At 80°C, a G' of 746 kPa is measured for the ionomer, which is only $\approx$ 6% of its value measured at room temperature. Regarding the polyolefin, the rheology measurements show that this adhesive has a good resistance to high temperatures
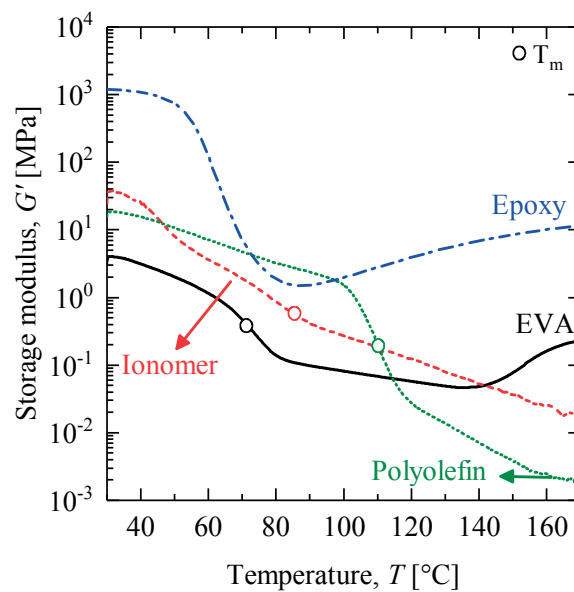
Figure 6.3 – Thermo-mechanical properties of all adhesives. Results for the EVA, the ionomer and the polyolefin are obtained by rheology after lamination and results for the epoxy are calculated from DMA data using equation 6.1. Round symbols represent the melting temperature measured by DSC.

with a melting point of around 110°C. We measured a storage modulus of about 2.97 MPa at 80°C, much higher than the value measured with the ionomer. Finally, epoxy is the adhesive that shows the highest storage modulus. However, we observe that in the range of 75–100°C, its storage modulus decreases, being even lower than the value measured for the polyolefin adhesive. At temperatures above 100°C, the epoxy can further cross-link, which leads to an increase of G'.

B. Skins

We measured the mechanical and thermal properties of the skins after manufacturing, thermal cycling, damp heat and at 80°C. Table 6.3 shows that Young's modulus of the skins does not change with thermal cycling or damp heat tests. The increase in temperature to 80°C induces a decrease of E by 40%, which can considerably affect the thermo-mechanical properties of the sandwich structure. As measured using DMA, the T_g of the skins is 80°C after manufacturing. After thermal cycling and damp heat, we measured a T_g of 83°C and 78°C, respectively. These results show that the aging tests do not degrade the initial thermal properties of the skins. In fact, T_g slightly increases due to further post curing.

Table 6.3 – Young's modulus, ultimate tensile strength and glass transition temperature of the skins obtained before and after aging and at high temperature.

Test	E_f [GPa]	σ_{UTS} [MPa]	T_g[°C]
Initial	19.1	239	80
TC	18.6	230	83
DH	18.4	220	78
80°C	11.5	156	-

6.3.2   Mechanical stability of composite sandwich structures

Figure 6.4 and 6.5 summarizes the bending stiffness of all composite backsheets studied before and after aging and at 80°C. The reference epoxy/aramid-based sandwich reference shows a high bending stiffness (15.5 N·m²) and is therefore taken as the target to match. Moreover, its bending stiffness does not change after thermal cycling and damp heat. At 80°C however, the bending stiffness decreases by 55%, which is linked to the decrease in mechanical stiffness when exceeding the epoxy glass transition temperature (53°C). EVA is kept as a benchmark, even though the bending stiffness for EVA-based sandwiches is lower (11.1 N·m²) than for the samples processed with epoxy, as demonstrated in Chapter 5. We observe that the bending stiffness of EVA-based sandwiches is slightly reduced (10.3 N·m²) after damp heat, but decreases by 23% and 87% after thermal cycling and at 80°C, respectively. The ionomer-based sandwiches show a high bending stiffness at room temperature and after thermal cycling (14.2 N·m² and 13.8 N·m², respectively), close to the properties obtained with the epoxy-based
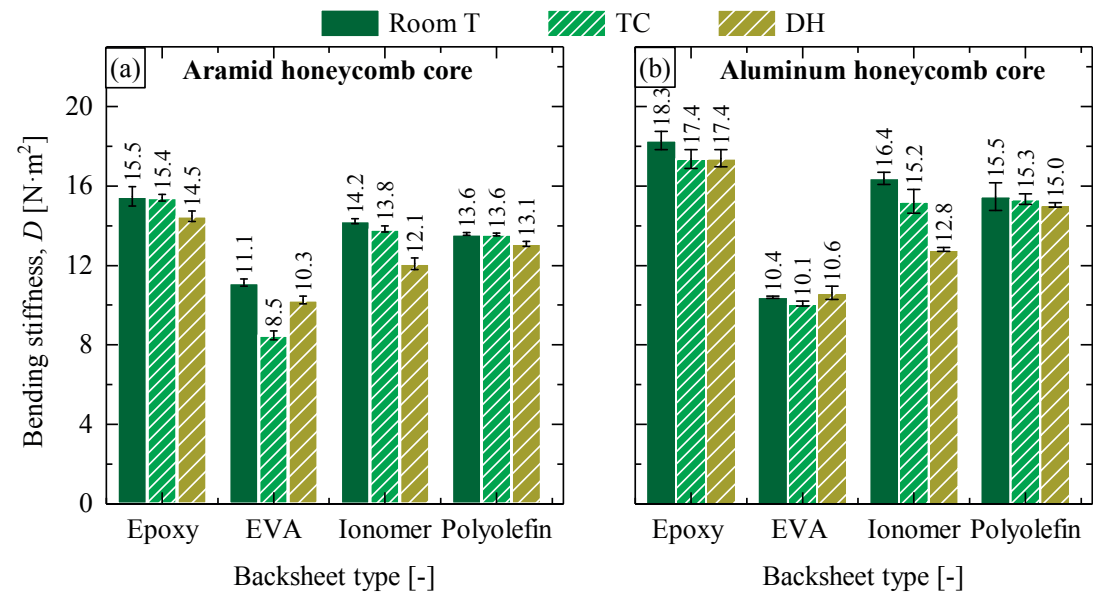
Figure 6.4 – Bending stiffness measured in a four-point bending test for backsheets manufactured with: (a) an aramid core and (b) an aluminum core using different adhesives, after acelerated-aging tests.

sandwiches. After damp heat the ionomer-based sandwich shows a 15% decrease in bending stiffness, very similar to the epoxy adhesive as well. However, at 80°C, the ionomer-based sandwich shows a strong decrease of 90%, because the melting temperature of the ionomer is
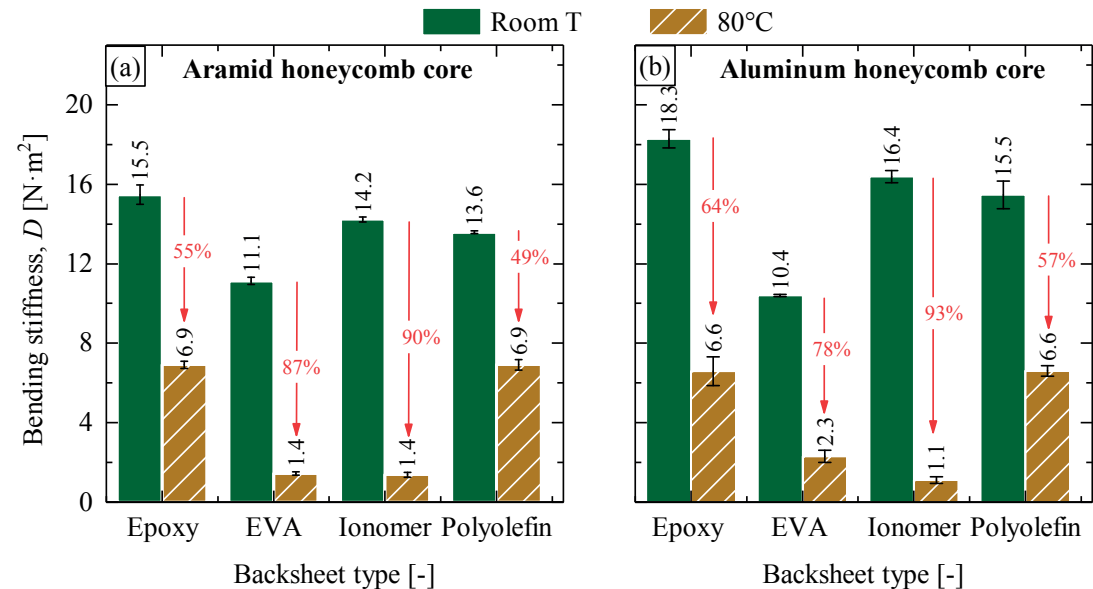
Figure 6.5 – Bending stiffness measured in a four-point bending test at room and high temperature for backsheets manufactured with: (a) an aramid core and (b) an aluminum core using different adhesives.

close to 80°C (see details in section 6.3.1). The polyolefin-based sandwich shows a bending stiffness close to the value obtained with the epoxy reference adhesive (13.6 N·m^2). These composite sandwiches show a higher bending stiffness at 80°C than the sandwiches produced with ionomer. Additionally, the bending stiffness of the polyolefin-based sandwich structures does not change after thermal cycling or after damp heat.

Similar to what is observed with an aramid core, with an aluminum core we observe a loss of bending stiffness of 78%, 93% and 57% for the EVA-, ionomer- and polyolefin-based sandwich structures, respectively. Beside the decrease at high temperatures with EVA and ionomer, the sandwich produced with a polyolefin adhesive and an aluminum core shows a similar decrease as observed with the epoxy-reference sandwich.

Ideal composite sandwich backsheet: polyolefin/aluminum-based structure

Figure 6.6 shows the relative variation of the parameters measured at 30°C and 80°C, i.e. the Young's modulus of the sandwich skins (E_f) and the storage modulus of the polyolefin and epoxy adhesives ($G'_{polyolefin}$ and G'_{epoxy}). We calculate the equivalent Young's modulus of full sandwiches (E_{eq}) from the bending stiffness according to

$$D = E_{eq} \cdot I_{\text{inertia}} \tag{6.2}$$
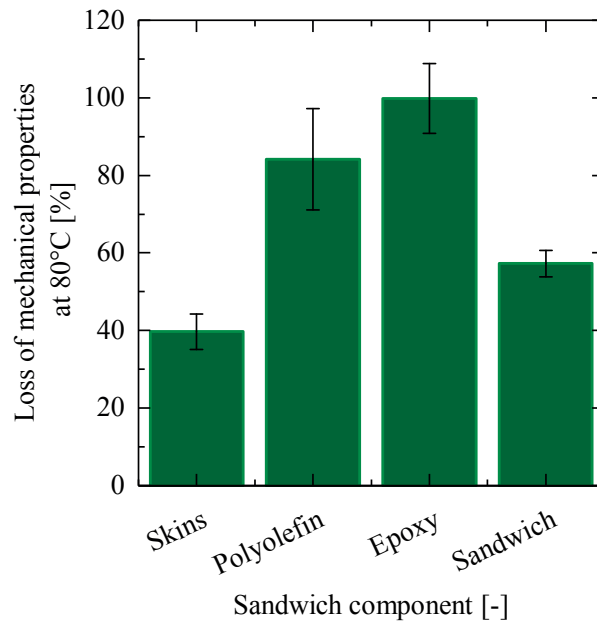
Figure 6.6 – Loss in mechanical properties when material is heated up from room temperature to 80°C considering: the Young's modulus of the skin and sandwich; the storage modules of the polyolefin and epoxy obtained from rheology and DMA measurements, respectively.

where $I_{inertia}$ (expressed in m^4) is the sandwich inertia momentum. We observe that the E_f decreases by 40% when the temperature increases from room temperature to 80°C. However, $G'_{polyolefin}$ and G'_{epoxy} decrease by 80% and 99%, respectively. Thus the loss in bending stiffness in the sandwich, when the samples are heated to 80°C, comes mainly from the decrease of the rigidity of the adhesives. Beside the relative high loss of the sandwich thermo-mechanical properties, polyolefin shows an equivalent stiffness to the epoxy-reference adhesive. Thus, polyolefin adhesives combined with a high-thermal-conductivity core are the best sandwich structure to replace the standard one.

6.3.3 Thermo-mechanical and electrical stability of lightweight PV modules

We selected the polyolefin-based sandwich with an aluminum honeycomb core to produce our two-cell module. For sake of comparison, we also manufactured glass-backsheet modules and subjected both configurations to accelerated-aging tests.

Thermal cycling and damp heat

Figure 6.7 shows the loss in electrical performance (I_{sc}, P_{max}, V_{oc} and FF) measured during and after thermal cycling and damp heat (performed sequentially). We notice that the power loss measured for the lightweight module is similar to the loss measured for glass-backsheet modules prepared with exactly the same cells. In the former, we measured a power loss of -3% and -2% after thermal cycling and damp heat, respectively. EL characterization of the
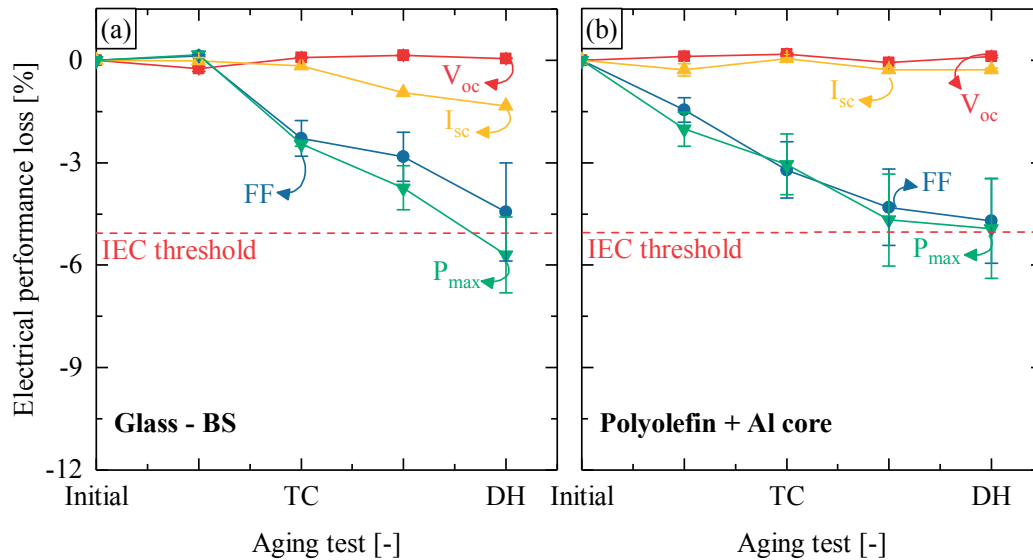
Figure 6.7 – Electrical performance loss after a sequence of thermal cycling and damp heat aging tests for (a) the glass-backsheet modules and (b) the polyolefin/aluminum-based lightweight module. We indicate the threshold of -5% for the purpose of diagnosis.
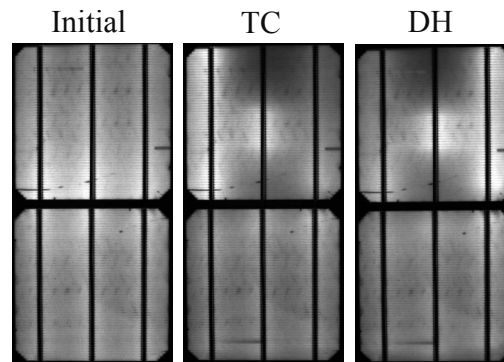
Figure 6.8 – Electroluminescence imaging of the polyolefin/aluminum-based module after the accelerated-aging tests (thermal cycling and damp heat) presented in figure 6.7.

polyolefin/Al-based modules shows no signs of damages, cracks or corrosion after aging tests (figure 6.8). Small darker areas in the EL images are due to an increased contact series resistance, identified during the electrical tests. For the glass-backsheet configuration, we measured a power loss of -2% and -3.5% after thermal cycling and damp heat, respectively. These losses are mainly due to the increase in contact resistance and, consequently, a decrease in FF. With this configuration, we also observe a slight decrease of I_{sc}, especially after damp heat. In fact, during damp heat, moisture entered the encapsulant. When we removed the samples from the damp heat chamber, they appeared hazy due to the production of water droplets from the supersaturation when the samples are cooled quickly [197]. In the case of the glass-backsheet configuration, this haze takes more time to disappear compared to an ETFE frontsheet, which consequently has an effect on the I_{sc} measured.

Potential-induced degradation

Figure 6.9 shows the I-V curves after the PID test of the lightweight PV module and a standard glass-backsheet module. The results show that, besides the strong PID effect present on the standard glass-backsheet module (-49.3% after 192 h), the same solar cells do not show any PID effect when encapsulated within the lightweight design. A front cover made of soda lime glass, which contains Na^+ ions, is known to promote PID, if used in combination with a low-volume-resistivity encapsulant. During the test, the moisture and high temperature enhances the alkali metal ions' migration from the glass towards the cell surface thus causing a strong degradation [198]. If we remove the glass cover, we remove the primary source of Na^+ ions, which cause the degradation, and therefore we can avoid PID. The EL images (figure 6.10) show that the lightweight PV modules do not show any signs of degradation due to PID.

The excellent mechanical stability evidenced by the absence of visual defects (including bending and twisting of the sandwiches) and by a negligible degradation in electrical performance after the aging tests (thermal cycling, damp heat and potential-induced degradation)
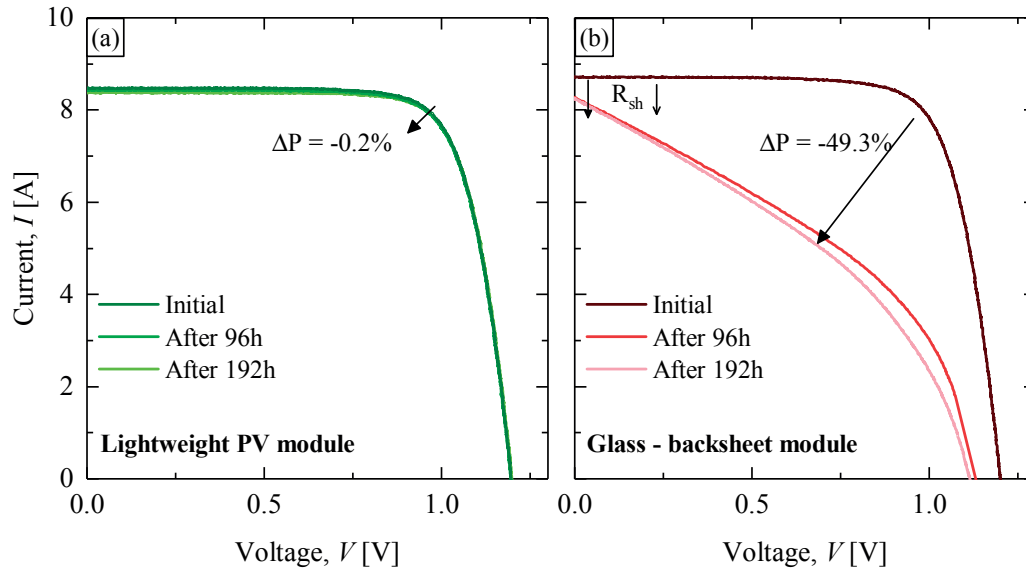
Figure 6.9 – Current-voltage curve of (a) a lightweight module and (b) a glass-backsheet PV module after a potential-induced degradation test. The test is performed at 85°C/85°RH/-1000V.

(a) Lightweight PV modules   (b) Glass-backsheet PV modules
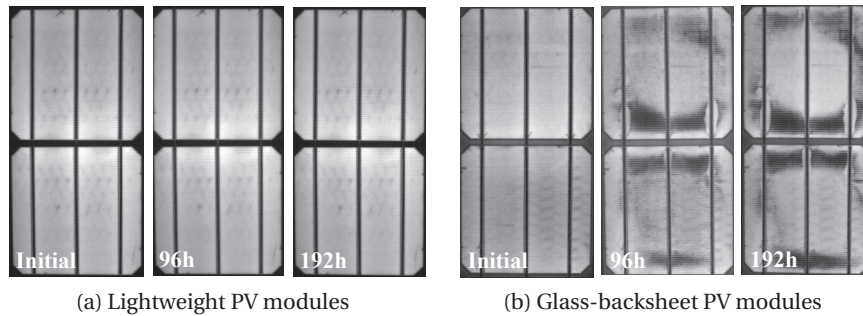
Figure 6.10 – Electroluminescence imaging of (a) lightweight and (b) glass-backsheet PV modules measured after manufacturing and after 96 h and 192 h of potential-induced degradation test (85°C/85°RH/-1000V).

shows that we are able to manufacture a durable lightweight device by using a high-thermal-conductivity core and a polyolefin adhesive. With this material selection, the lightweight PV module will have a final weight of 6 kg/m^2, meaning that we have reduced up to 70% of the weight of currently available BIPV modules.

6.3.4 Pre-qualification of lightweight PV modules

We scaled up our lightweight PV module composed of a polyolefin/aluminum-based sandwich structure backsheet and an EVA/ETFE frontsheet to a sixteen-cell module. In order to pre-

qualify our design, we followed three different sequence tests from *IEC 61215* [66]. Figure 6.11 shows the electrical losses after Sequence C, Sequence D and Sequence E (details presented in figure 1.10).

Due to equipment limitations, Sequence C was performed on two-cell modules. From this sequence we observe a slight decrease in I_{sc} after the UV preconditioning test, due to a slight yellowing of the front cover. However, this decrease affects the power output with only a
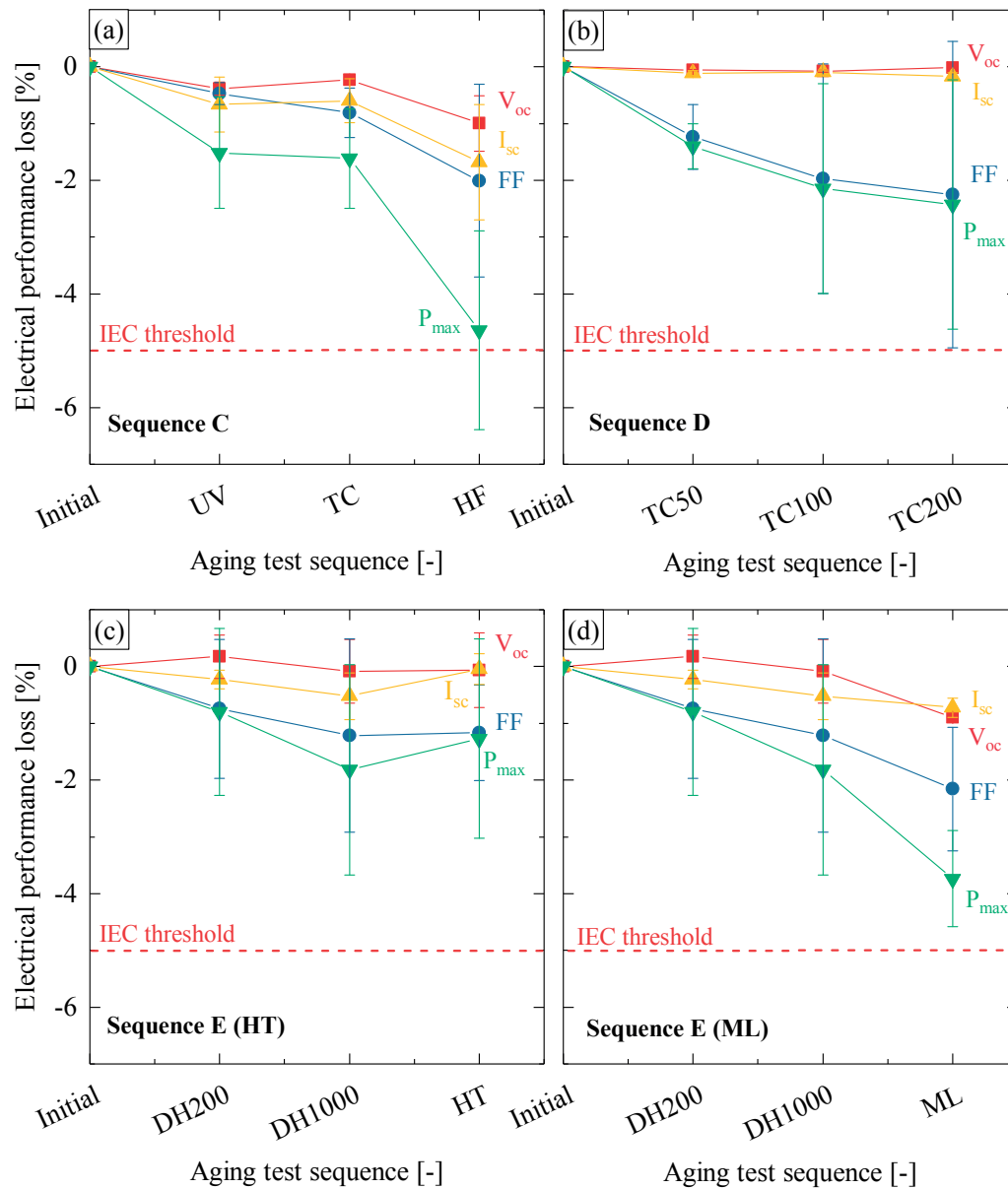
Figure 6.11 – Power loss — relative to the initial condition — of lightweight PV modules subjected to (a) Sequence C, (b) Sequence D, (c) Sequence E with hail test and (d) Sequence E with static mechanical load test from the qualification standard *IEC 61215-2:2016* [66].

Initial   DH1000   HT
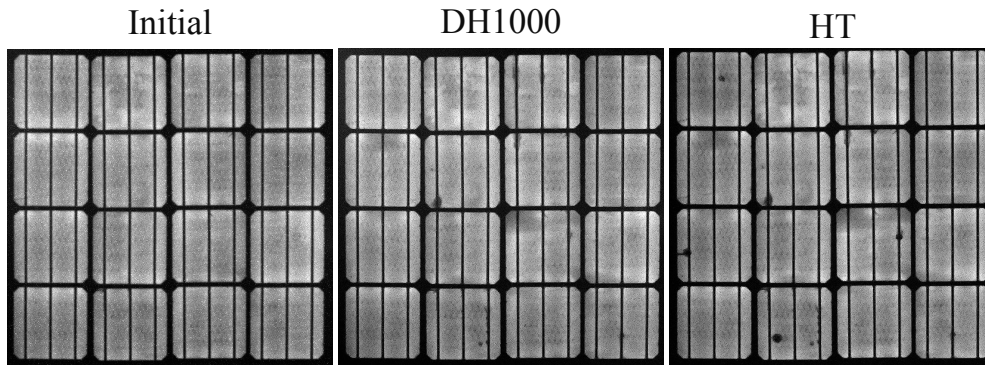
Figure 6.12 – Electroluminescence imaging of lightweight PV modules subjected to 1000 h of damp heat testing followed by hail test, which correspond to *Sequence E* from the qualification standard *IEC 61215-2:2016* [66].

small loss (-1.5%). After the preconditioning test, we introduced the same samples to thermal cycling for 50 cycles and later to humidity freeze. No degradation is observed after the thermal cycling test. However, after humidity freeze we observe a further decrease of -3%, mainly due to an increase in R_s and consequently a loss in *FF*.

The modules subjected to Sequence D show a power loss of -2.4% after 200 thermal cycles. This loss comes mainly from the equivalent loss in *FF*. No changes are detected from the EL images or from the visual inspection.

From Sequence E, modules show a power loss of around -1.8% after the damp heat test, mainly due to the decrease in I_{sc}. Again, this loss comes mainly from the yellowing and hazing observed on the materials in front of the solar cells (EVA) (see explanation for haze effect in section 6.3.3). After the damp heat test, we tested two modules under the hail test and other two in the static mechanical load test. The hail did not increase the power degradation, instead we see that the power slightly increased: the water droplets created after removal from the damp heat test will slowly disappear [197]. (It can take several weeks, depending on whether the configuration is glass/glass or glass/backsheet.) Since the hail test was performed a few days after the removal from the damp heat chamber, the percentage of moisture inside the module was already lower, thus increasing the I_{sc} and consequently the P_{max}. However, as can be seen in the EL images (figure 6.12), in all the spots where the ice ball hit the module we observe a cracked area (similarly to what we saw with commercial lightweight PV modules). Regarding the mechanical load test, we measure a reduced power loss (-1%) after the test, without any visual changes after the test. How to improve mechanical resistance under impact or uniform loads will be discussed in detail in Chapter 7.

These results show that after each sequence we observed degradation below the -5% pass/fail criteria present in *IEC 61215*. Moreover, the wet leakage test performed with our sixteen-cell modules showed that the insulation of this design under wet operation conditions is satisfactory, showing an insulation resistance higher than the pass/fail criterion of 40 MΩ·cm^2.

6.4 Conclusions

This chapter showed that thermoplastic adhesives (ionomers and polyolefins) are suitable to produce a composite sandwich structure with excellent mechanical properties (stiffness), not only at room temperature but also after aging tests, such as thermal cycling and damp heat. However, when the composite sandwiches were mechanically loaded at 80°C, a significant decrease in sandwich bending stiffness was observed, especially with the ionomer. From the rheology measurements, we identified a strong reduction of the storage modulus of the ionomer at high temperatures. This loss had a direct impact on the final sandwich bending stiffness. In contrast, the polyolefin adhesive showed a high rigidity, not only at room temperature but also at temperatures above 80°C. Rheology measurements showed that polyolefin has a melting point of 110°C, which is below the manufacturing process temperature, providing this polymer a high storage modulus at the module operating temperature. Combining this adhesive with an aluminum honeycomb core, we obtained a sandwich with a Young's modulus of 17.6 GPa. The bending stiffness of the composite sandwich backsheet structures produced with polyolefin showed no degradation after thermal cycling and Damp heat, and a reduction similar to what was observed with the epoxy adhesive reference at 80°C.

Further, using this backsheet design (polyolefin and aluminum honeycomb core), we showed that it is possible to produce a lightweight PV module architecture of only 6 kg/m^2 that is able to withstand the most-demanding IEC aging tests. Aging of two-cell modules led to very good results after thermal cycling and damp heat with, respectively, -3% and -2% losses in electrical performance (power). In addition, the PID tests showed that even using solar cells prone to PID in a glass-backsheet modules (close to -50% power loss), the lightweight modules did not degrade thanks to the substitution of the front cover glass with a thin polymer ETFE foil. We further demonstrated the scalability of these results by fabricating sixteen-cell modules which successfully passed Sequence C, Sequence D and Sequence E of the IEC qualification tests.

However, when subjecting the proposed devices to a hail test, we observed cracked solar cells near the impact spots, as we previously observed with the commercial modules (see Chapter 3). To further demonstrate the performance of our lightweight module structure, Chapter 7 examines how the frontsheet can be redesigned to mitigate the impact of hail. Additionally, a complete study of the mechanical stability is presented as well.

7 Mechanical stability of lightweight PV modules

Summary

This chapter shows that a balance between frontsheet design and backsheet stiffness has to be found in order to maximize hail resistance and mechanical rigidity while minimizing the module's weight. Hail resistance is achieved by correct material selection: (i) the frontsheet must have a complex modulus between 350 and 450 MPa to ensure that the impact energy is dissipated locally on the module's surface, and (ii) the backsheet must have a maximum equivalent Young's modulus of 17.4 GPa to allow for global energy dissipation during the impact. Furthermore, we show that the use of a stiff frontsheet does not reduce the reliability of the lightweight PV module under a thermal stress test (2000 h in damp heat, 500 cycles in thermal cycling and 100 cycles in humidity freeze). Using finite element modeling we evaluate the module's behavior under a static mechanical load. We conclude that this equivalent Young's modulus provides a curvature radius higher than the minimum threshold value solar cells can sustain without cracking. We scale up this design to a sixteen-cell module, which shows good stability under static mechanical load tests with no power loss or cracks in the solar cells.

The results presented in this chapter are part of a publication entitled *"Robust glass-free lightweight photovoltaic modules with improved resistance to mechanical loads and impact"* (see ref [89]).

7.1 Introduction

PV modules are laminates composed of many layers with different mechanical properties. These layers (usually a glass cover as the front layer) are responsible for protecting the panels

from a wide variety of forces that might compromise the mechanical stability or integrity of the module during its service life. In response to mechanical stress, modules may bend and show cracks in the solar cells, fatigue of interconnections, permanent deformations or delaminations between components. These forces can occur during handling, shipping or installation or in the field (rain, wind, snow). The reader is referred to [199–201] for an overview of mechanical issues affecting the durability and performance of PV modules.

Mechanical stability is one of the challenges in lightweight PV design [202, 203]. From one side, the polymer frontsheet that substitutes for the front glass may not completely protect the solar cells against the effect of impacts. On the other side, the decrease in module stiffness and mechanical stability, due to the absence of glass, might make the module unable to survive heavy mechanical stress. Different studies about the mechanical resistance of standard PV modules can be found in the literature [201, 204–209]. However, little work has been done on the mechanical resistance of lightweight PV modules. In 1978 [210], for the first time, it was shown that PV modules without a glass frontsheet could pass the hail test without visual changes or significant power loss. Nevertheless, at that time, it was not possible to use electroluminescence (EL), which reveals crack patterns (not visible to the human eye), and correlate the carcks with power loss. Other authors [201, 211] showed the importance of including the real mounting system and the stiffness of the substrate when performing the hail test. However, any correlation between the backsheet and frontsheet stiffness was not yet studied. In other fields, the problem of impacts on the composite sandwich structures for other applications was already extensively investigated [212–214]. Most of these studies concern problems in marine or aerospace applications, which require impact testing with high velocities. In our case, we aim to design composite structures with soft polymeric materials that can protect a very thin (180 μm) and brittle element (i.e. the solar cells).

The goal of the present capter is to investigate the resistance of lightweight PV modules to mechanical stress, such as impacts and static loads. To do so, different types of frontsheet and backsheet are selected and their mechanical properties characterized using different test methods.

7.2 Experimental procedure

7.2.1 Lightweight module design and production

Glass-free lightweight PV modules were manufactured according to the design in figure 6.1. These modules can be divided into two main parts: a composite sandwich backsheet structure (in this chapter we use only on the aluminum honeycomb core) and a frontsheet. Three different sandwich adhesives are studied: epoxy (reference condition), EVA and polyolefin (PO). The manufacturing process of a lightweight PV module depends on the choice of sandwich adhesive, following the guidelines presented in table 5.2. Three types of modules were produced:

- Two-cell module (20 cm × 40 cm) – to study the influence of the frontsheet and backsheet design on resistance to the hail test.

- Twelve-cell module (81 cm × 81 cm) – to evaluate the resistance of the ideal fronstheet and backsheet at larger sizes under the hail test.

- Sixteen-cell module (81 cm × 81 cm) – to study whether the proposed sandwich is rigid enough to pass the static mechanical load test.

All fabricated modules were composed of conventional mono-crystalline silicon solar cells with three or four busbars encapsulated with different encapsulant foils and covered by a thin tetrafluoroethylene layer (ETFE). For the frontsheet study, different grades of glass scrim ($17/30/100$ g/m^2) were added to increase frontsheet rigidity. Table 7.1 shows the frontsheet layups developed for the hail test study. For the static mechanical load test, a standard frontsheet (ETFE/EVA) is used.

Table 7.1 – Summary of the frontsheet structures developed for the hail test and DMA.

	Layer 1 [mm]	Layer 2 [mm]	Layer 3 [g/m^2]	Layer 4 [mm]
Type 1	ETFE (0.1–0.2)	EVA (0.45–2.7)	-	-
Type 2	ETFE (0.1–0.2)	IO/PO (0.45–2.7)	-	-
Type 3	ETFE (0.1–0.2)	EVA/IO (0.45–2.7)	glass scrim (17/30/100)	EVA/IO (0.45)

7.2.2 Frontsheet and backsheet characterization

The bending stiffness (D) of the different composite sandwich structures presented here are taken from the four-point bending test performed in Chapters 5 and 6. For this study we selected: (i) EVA-based backsheet (BS$_1$), (ii) polyolefin-based backsheet (BS$_2$) and (iii) epoxy-based backsheet (BS$_3$). A sample made of glass/EVA/glass was also measured as a control for the static mechanical load test, and its D was calculated according to [215]. The bending stiffness measured from the four-point bending test was used to calculate the equivalent Young's modulus (E_{eq}) according to equation 6.2. Dynamic mechanical analysis (DMA) was used to obtain the storage modulus (E') and the loss modulus (E''), used later to calculate the complex modulus (E^*). DMA is performed according to description given in section 2.2.3. A set of three different samples for each type were tested according to table 7.1.

7.2.3 PV module testing methods

Hail test

The hail test study was performed on two-cell modules according to section 2.4.6. Two different studies were performed:

- The influence of the backsheet on the resistance to hail impacts. A constant frontsheet made of 0.1 mm ETFE and 0.9 mm EVA foil was used and the backsheet was changed to have different E_{eq}. One sample for which the backsheet was a bare glass (3.2 mm) was also tested and used as a reference.

- The influence of the frontsheet rigidity on the resistance to hail impacts. A composite backsheet with an E_{eq} of 13.9 GPa was used and the frontsheet structure was changed using single or multi-stack layers, as described in table 7.1.

Once the ideal frontsheet and backsheet structures were identified, the optimal combination was used to upscale the size of the device to a twelve-cell module, in order to validate the results obtained on two-cell modules. The lightweight module was then hit with hail stones on seven relevant locations, as indicated in *IEC 61215* and represented in figure 7.1. The relevant locations were a corner of the module, the edge of the module, the edge of the circuit (individual cells), close to the mounting structure, any two points vulnerable to hail, and a point farthest from the above-selected points. The quality of the modules was controlled before and after the test by means of I-V curve performance measurements and EL imaging as described in sections 2.3.1 and 2.3.2, respectively.
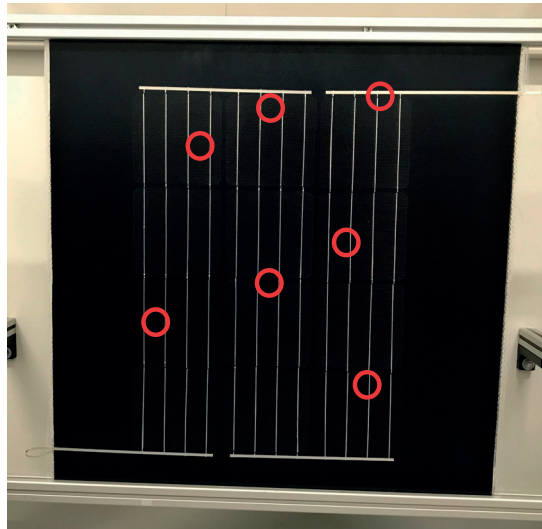
Figure 7.1 – Hail test setup. Red circles indicate the impact locations.

Static mechanical load test

The static mechanical load tests were performed according to procedure given in section 2.4.7. Three different types of PV modules were manufactured and tested by applying 2400 Pa in three cycles of pressure and suction: a glass-glass module with E_{eq} of 54.3 GPa (reference), composite backsheets with low (13.9 GPa) and high (17.4 GPa) equivalent Young's modulus.

Thermal stress tests

The use of a stiff frontsheet is not the preferred solution for PV developments. A significant increase in encapsulant stiffness not only increases the probability of delamination, but also reduces the ability to withstand mismatches in thermal expansion. These problems can lead to solar cell or interconnection cracking, strongly affecting module performances [216]. In order to evaluate the effect of a stiff frontsheet on module performance, we produced two-cell modules with two different frontsheets: a high-stiffness frontsheet (ionomer) and a low-stiffness frontsheet (EVA). A backsheet with an equivalent Young's modulus of 17.4 GPa was selected for this study. After the two-cell modules were characterized by EL and I-V measurements they were introduced to extended aging tests: 2000 h in damp heat, 500 cycles in thermal cycling and 100 cycles in humidity freeze.

7.2.4 Finite element modeling simulations

Finite Element Modeling (FEM) was used to study the required backsheet stiffness to maximize the module curvature radius under load. This model aims at providing fast feedback about the mechanical stability of new composite lightweight designs. We developed a 3D model created using ComsolMultiphysics which includes:

- A plate of 81 cm× 81 cm (no frame), fixed in a four-clamp aluminum mount (8 cm long) installed at each corner (figure 7.2). Between the aluminum clamp and the plate surface there is a thin ethylene propylene diene monomer (EPDM) rubber used to protect the modules, which is also considered in our design. The properties of aluminum and EPDM were obtained from the data-sheet provided by the producer.

- No solar cells or frontsheet are considered in this model (for simplicity). Our goal was to simulate the behavior of the structure under load. In our case, the rigidity is given only by the composite sandwich structure.

- All materials are considered isotropic and fully elastic (no visco-elasticity or temperature dependence is included).
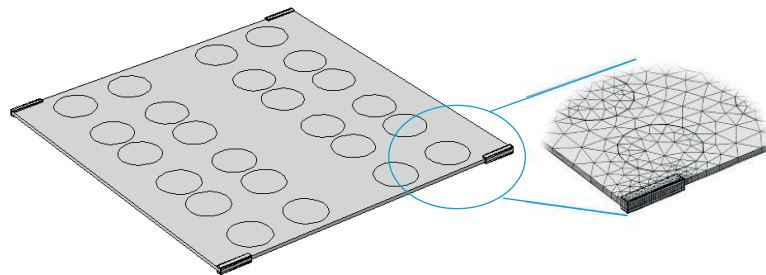
Figure 7.2 – Basic setup, mesh and boundary conditions of loads and support for the study of composite structure behavior.

- The model assumes a stress-free state at the beginning of the simulation.

We selected three different types of structure: (i) Plate 1 with a high stiffness (54 GPa), (ii) Plate 2 with an intermediate stiffness (17 GPa), and (iii) Plate 3 with a low stiffness (14 GPa). We used 24 vacuum cups distributed over the plate surface, exactly in the same position as in the static mechanical load test. Table 7.2 shows the material properties used in the model. The simulation was run with a load step of 100 N over the load interval of interest ($\pm$2400 Pa). The output of the simulation is the module deflection over the width of the PV module.

Table 7.2 – Material properties used for modeling.

Material	Young's modulus, E [GPa]	Poisson's ratio, v [-]	Density, ρ [kg/m^3]
Plate 1	54	0.2	2500
Plate 2	17	0.4	466
Plate 3	14	0.4	466
Al clamps	70.0	0.35	2700
EPDM	0.0006	0.5	930

7.3   Results

7.3.1   Impact resistance of lightweight modules

Influence of the backsheet stiffness

From results obtained in Chapters 5 and 6, we calculate the equivalent Young's modulus (E_{eq}) shown in figure 7.3, together with the reference condition composed of a single glass layer. The results show the importance of the sandwich adhesive selection and its impact on the final sandwich stiffness. BS$_1$ is fabricated using EVA, a viscoelastic adhesive with a reduced storage modulus at room temperature (0.31 MPa) [88]. This low rigidity makes the composite sandwich more compliant. BS$_2$ uses a thermoplastic polyolefin adhesive that has a higher storage modulus (18.77 MPa) than EVA, thus a higher E_{eq}. BS$_3$ uses a thermoset adhesive (epoxy) with a high storage modulus at room temperature (1242 MPa). This high rigidity ensures a better stress transfer from the skins to the core, providing the sandwich with an even higher E_{eq}. From the visual inspection of the modules after the hail test, none of the modules show any visible damage (no cracks are visible to the naked eye). The results clearly indicate that the power loss increases with increasing backsheet stiffness, with the maximum acceptable power loss of -5% (threshold kept for diagnosis) being reached for a backsheet stiffness of 17.4 GPa (see figure 7.3). Moreover, there is a change in damage patterns in the EL images between BS$_1$, for which the cracking area stays localized below the impact point, and the BS$_2$, for which the damaged zone extends far away from the impact points (figure 7.4).

Generally, in standard glass-baclsheet PV modules, increasing the stiffness of the modules tends to reduce the amount of deflection of the full structure for a given front side load and thus lowers cracking within the modules [217]. However, in our configuration, this stiffness is located at the back of the solar cells and not at the front, as with standard PV modules. The solar cells are protected by only a viscoelastic polymer layer. Thus during a hailstone impact, the complex frontsheet/solar cell structure will bend until any additional deformation is hindered by the stiff composite sandwich structure. When a high-stiffness backsheet is used, the solar cells are deformed until the backsheet is reached. Any additional impact energy from the ice balls beyond this point will consequently crack the solar cells, since further mechanical deformation will be hindered. When a lower-stiffness backsheet is used, the impact energy is used to bend not only the complex frontsheet/solar cells but also the backsheet structure. In conclusion, reducing the backsheet bending stiffness will enhance the resistance to hail of our lightweight PV module. However, it may not always be the ideal solution as it may lead to
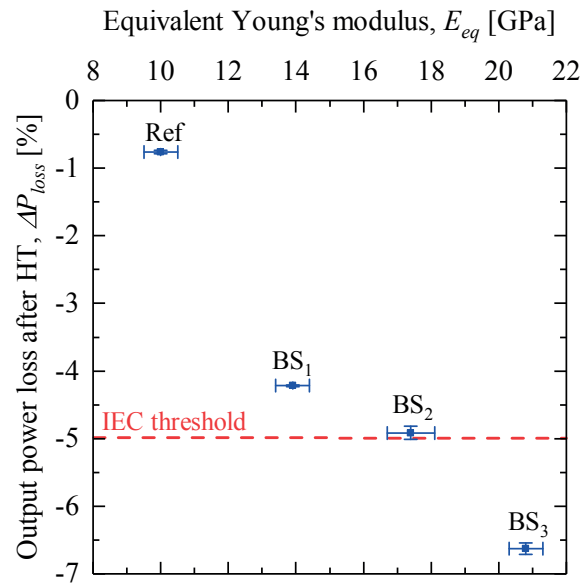
Figure 7.3 – Power loss after a hail test of two-cell modules manufactured with backsheets having different equivalent Young's modulus (E_{eq}).
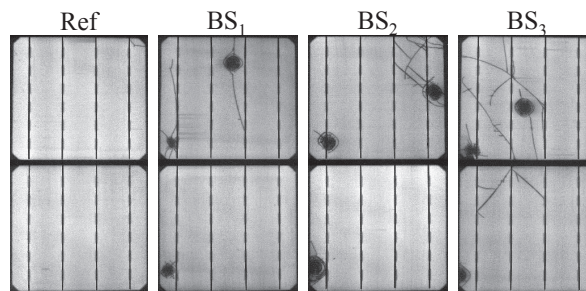
Figure 7.4 – EL images of the different modules presented in figure 7.3 after the hail test.

the need for a stronger support structure depending on the module size and load conditions (snow/wind load) experienced during the modules's service life. Therefore, it is important to evaluate the potential to reduce hail damage through energy dissipation in the frontsheet.

Influence of the frontsheet properties

Figure 7.5 shows the correlation between the power loss of a two-cell module with different frontsheets and an identical backsheet after a hail test and the mechanical properties of the frontsheet as measured by DMA. The results allow us to discriminate between three main groups of frontsheets, based on their mechanical properties:

- Group (a) – frontsheets with a low complex modulus ($E^* \approx 66$–87 MPa) produced with encapsulants with low rigidity.

- Group (b) – frontsheets with a high complex modulus ($E^* \approx 350$–550 MPa) composed of a polymer with high rigidity.

- Group (c) – samples composed of a medium/high complex modulus ($E^* \approx 200$–390 MPa) dominated by a frontsheet made with polymer with low rigidity but reinforced with a glass scrim.
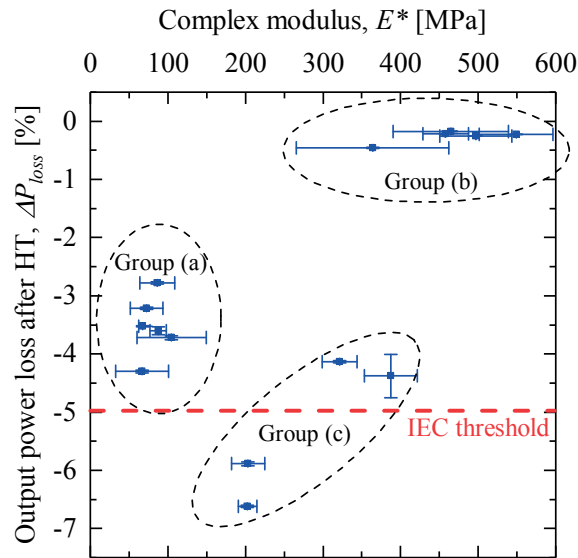
Figure 7.5 – Output power loss measured after a hail test, represented as a function of complex modules (E^*) of the different frontsheet structures composed of group (a) a low-rigidity polymer, group (b) a high-rigidity polymer and group (c) a low-rigidity polymer reinforced with a glass scrim. E^* is measured at 20°C using DMA.
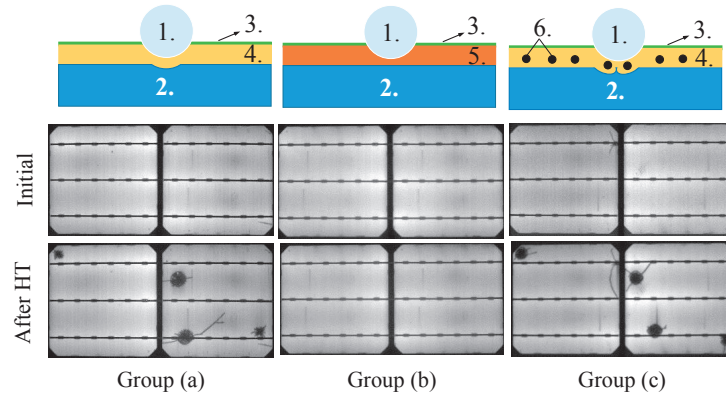
Figure 7.6 – EL images obtained after the hail test for samples composed by a backsheet type BS$_1$ and the frontsheet presented in table 7.1: type 1, type 2, and type 3. Numbers at the top sketch represent: 1. ice ball; 2. solar cell; 3. ETFE; 4. EVA; 5. IO or PO, and 6. glass scrim.

Frontsheets from group (b) show a low power loss (-0.2%) thanks to the **high-rigidity** polymer. During the test, the impact energy is dissipated on the surface and is not transferred to the solar cells. This effect is similar to what happens when a glass cover is used as the frontsheet due to the high rigidity of glass. This frontsheet category does not show evidence of cracks after the hail test, as can be seen in the EL images in figure 7.6. Although its mechanical properties are similar to those of ionomer, the polyolefin used in this work shows a disadvantage with regard to the ionomer: due to the slow cooling step after the lamination process, this thermoplastic
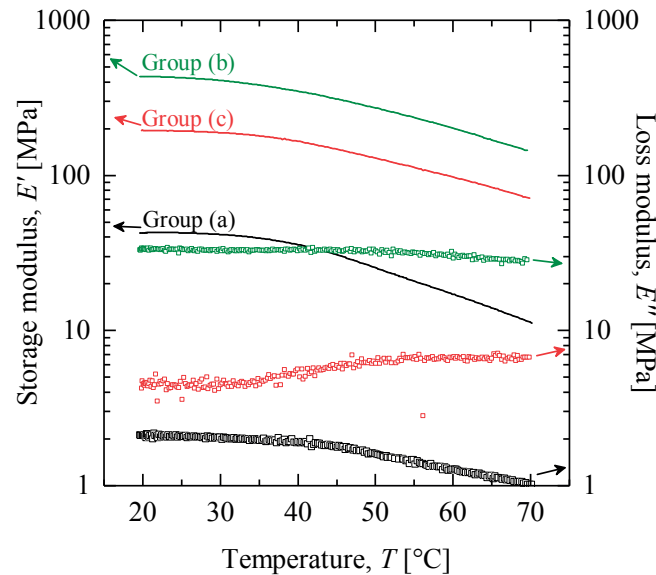
Figure 7.7 – Storage (E') and loss (E'') modulus of the different frontsheet types measured with DMA: group (a) low-rigidity polymer, group (b) high-rigidity polymer and group (c) low-rigidity polymer reinforced with a glass scrim.

creates crystalline areas that make the polymer appear milky. This partly reduces the light impacting the solar cells and, consequently, the short-circuit current. For samples in group (a) the **low rigidity** of the polymer allows for a transfer of the impact energy from the ice balls to the solar cells, resulting in a higher power loss (in the range of -3 to -4.3%).

Even if the frontsheet from group (c) shows a relatively high E^*, a strong power loss is measured ($\geq$ -4.4%). The use of a **low-rigidity polymer reinforced with thin stiff fibers** in front of the solar cells induces presumably a localized pressure in proximity of the fiber itself during the hail impact, consequently transmitting an increased portion of the impact energy to the solar cell, generating more defects or cracks. However, we tested modules manufactured with frontsheets composed of a glass scrim embedded in a high-rigidity polymer (ionomer) and after the hail test, no cracks or defects could be detected. In figure 7.5, these results are aggregated in frontsheet group (b) reinforcing the evidence for the proposed model. Figure 7.7 shows the viscoelastic properties of the different frontsheet types used during the hail test.

The samples from group (b) show the highest storage modulus of all the samples, and almost no power loss was detected during the hail test. In contrast, the samples from group (a) show the lowest storage modulus and consequently a higher power loss was detected.

Impact resistance using the predicted frontsheet/backsheet properties

With the help of DMA and the four-point bending test, it is possible to quantitatively estimate the mechanical properties of the frontsheet and backsheet, and to use these properties to qual-

	Isc	Voc	FF	Pmax
Initial	9.1	7.9	77.3	55.7
After HT	9	7.9	77.8	55.7

(a) EL images before and after HT. (b) I-V curves before and after HT.
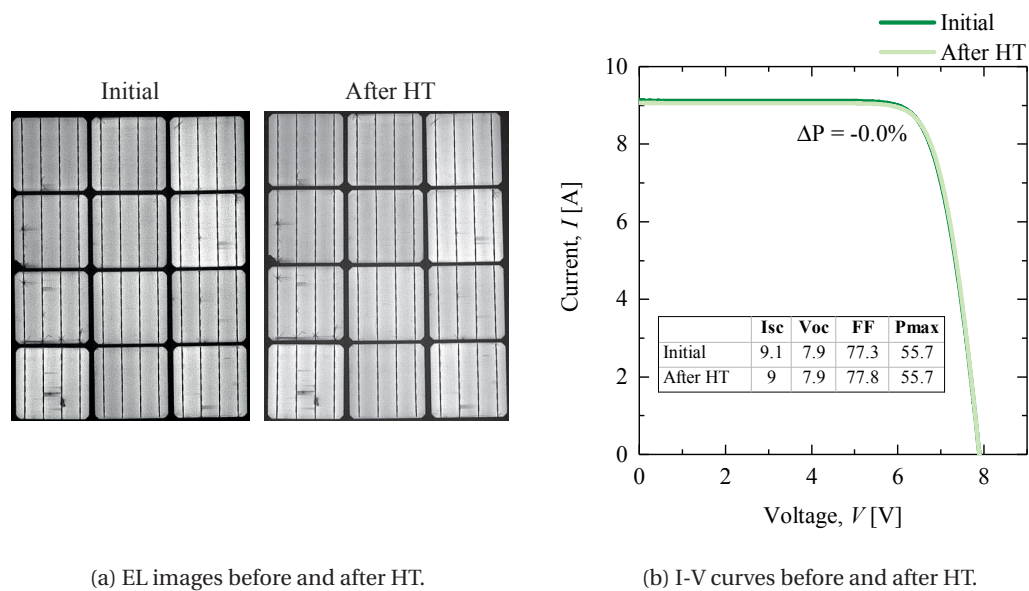
Figure 7.8 – EL image and I-V curve of a twelve-cell module manufactured using the optimal combination of frontsheet and backsheet before and after the hail test.

itatively predict the response of a new module design to hail impacts. Ideally, the frontsheet of the lightweight PV module must have a complex modulus between 350 and 450 MPa and a backsheet with an equivalent Young's modulus lower than 17.4 GPa. In order to demonstrate that we are able to scale up the size of our test devices and to show that this combination of properties is satisfactory to successfully pass the IEC hail test, we manufactured a twelve-cell module based on this material combination. Figure 7.8a shows EL images before and after the hail test. After the impacts, no cracks or any other major defect created by the ice balls is observed, indicating that the proposed combination of backsheet and frontsheet is optimal to successfully pass the *IEC 61215* hail impact test. From the I-V measurement shown in figure 7.8b we do not detect any power loss after the test.

7.3.2 Environmental stability with improved frontsheet

Figure 7.9 shows the main electrical properties of lightweight PV modules composed of frontsheets with different rigidity, after different aging tests. As a general conclusion, in all tests the two-cell modules with an ionomer frontsheet present the lowest ΔP_{max}. This is especially notable after damp heat and thermal cycling, where we measure a power loss
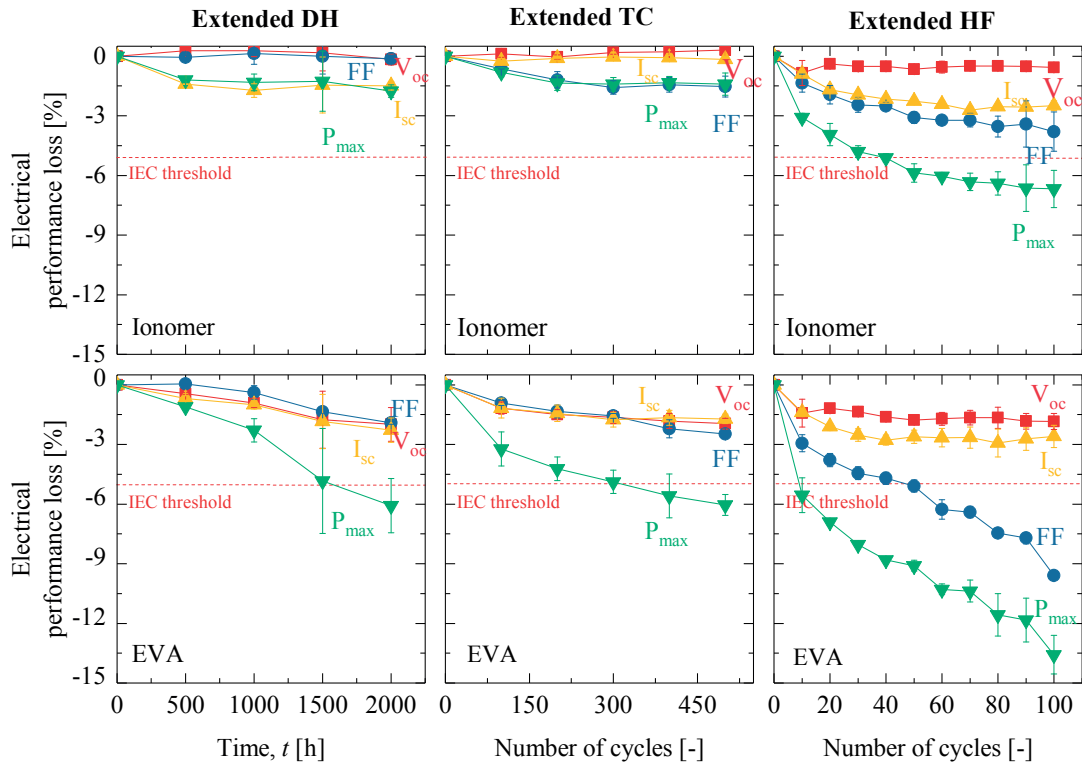
Figure 7.9 – Electrical performance loss measured during extended accelerated-aging tests (2000 h damp heat, 500 thermal cycles and 100 humidity freeze cycles) of lightweight PV modules with an ionomer or EVA front encapsulant.

of -1.8 and -1.4%, respectively, for the modules made with an ionomer frontsheet. In the same tests, the two-cell modules with an EVA frontsheet have a power loss of around -6.1 and -5.9% after damp heat and thermal cycling, respectively. This stronger loss is due mainly to a more pronounced yellowing of the EVA, a decrease in *FF* and a slight decrease in V_{oc}. Regarding humidity freeze, we observed a power loss of -6.3 and -13.5% for the ionomer and EVA frontsheet, respectively. These losses are due mainly to a decrease in I_{sc} and *FF*, more pronounced in the case of EVA. These results show that a stiffer frontsheet (ionomer) does not change the stability of the lightweight PV module under thermal aging test.

7.3.3 Mechanical stability under load

During the design of lightweight PV modules, there are two guidelines that must be followed in terms of mechanical stability:

1. Modules must retain dimensional stability at a maximum load of ±2400 Pa, as required by *IEC 61215*. To successfully pass this test, modules should not present cracked cells, power loss or any visual defect. To avoid cracked solar cells, the module curvature should not be less than the minimum curvature radius (*R*) solar cells can sustain (*R* is inversely proportional to deflection, thus we want to maximize the *R* in order to minimize deflection). The critical *R* is defined by the curvature when the first occurrence of cracks is detected during a static mechanical load test. Obviously, its value depends on the module design, i.e. dimensions, framing and encapsulation material used. From practical experiments, we know that for our module size, mounting system and type of solar cells selected, the *R* without cracked cells should be higher than 275 cm;

2. A 1.6 m × 1 m plate fixed over two rail bars should not exceed a deflection of 1 cm as stated in *DIN 18008 - Design and construction rules* [218]. To meet this standard, the lightweight PV module must have a minimum bending stiffness of around 370 N·m^2.

Combining FEM and test of small coupons under four-point bending test, we can define a sequence that will provide a fast and reliable method to select the most promising composite structures for the development of lightweight PV modules. This sequence consists of: **(a) quantifying the plate's Young's modulus by FEM**, which will provide a curvature radius higher than the value the solar cells can sustain without cracks; **(b) designing a sandwich structure** and using a four-point bending test to identify solutions in which E_{eq} is close to the *E*-threshold given by FEM and **(c) scaling up a promising composite structure** to a large PV module and testing it under the static mechanical load test for pre-qualification, according to *IEC 61215*.

A. FEM simulation

Figure 7.10 shows the maximum deflection simulated and measured for the different case studies (the maximum deflection measured will be discussed later in section 7.3.3). The reader
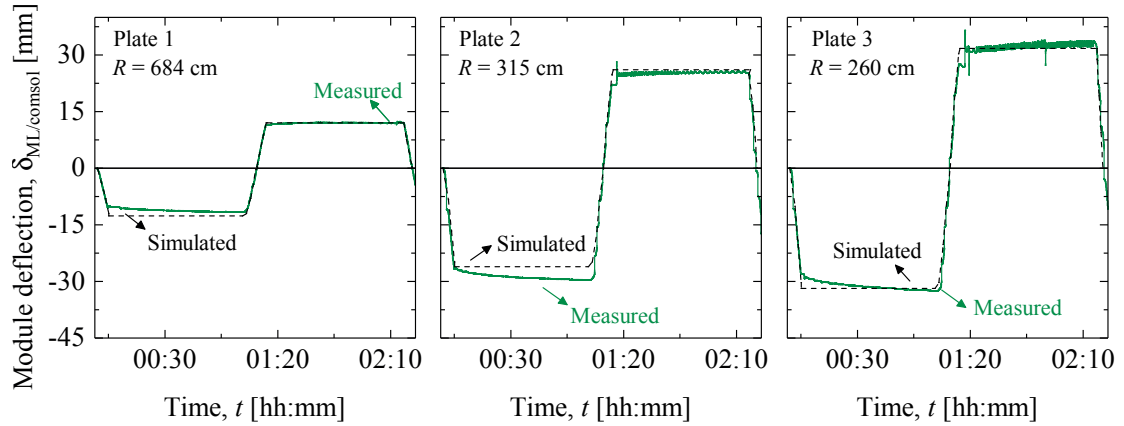
Figure 7.10 – Modules deflections under ±2400 Pa obtained by (i) FEM (black dot lines) and (ii) static mechanical load test (green full lines). R-values are calculated for the deflection simulated using FEM.

may refer to table 7.2 for details about the plate properties used in these simulations. For each maximum deflection at the center position of the module, we calculated the corresponding module curvature radius. We found that the sandwich structure will require a Young's modulus of ≥17 GPa to successfully pass the static mechanical load test. With this Young's modulus we calculate a curvature radius of 315 cm (higher than the minimum curvature solar cells can sustain without cracking). We then used the four-point bending test to identify the composite structure that matches the Young's modulus threshold identified by the FEM.

B. Identify sandwich structures with equivalent Young's modulus (E_{eq})

We manufactured three different structures that represent the different E values used in the FEM model: (i) a glass-glass structure with an E_{eq} of 54.3 GPa (equivalent to plate 1), (ii) a polyolefin-based sandwich structure with an E_{eq} of 17.4 GPa (similar to plate 2) and (iii) an EVA-based sandwich structure with an E_{eq} of 13.9 GPa (close to E of plate 3). These results suggest that a sandwich structure manufactured with polyolefin adhesive and an aluminum honeycomb core has the rigidity required to successfully pass the static mechanical load test without solar cell cracks. We further validated these results by performing a static mechanical load test.

C. Static mechanical load test – FEM model validation

Figure 7.11 shows the deflection of the different backsheet types over time, where three loading and suction cycles are applied, as described in [66]. Due to the double **glass-glass structure** of plate 1 the final equivalent Young's modulus is very high (54.3 GPa). When a 2400 Pa load is applied, this module shows a curvature radius of 672 cm, much higher than the threshold (275 cm) until where no solar cells cracks are expected. After the test, no power loss or solar

105
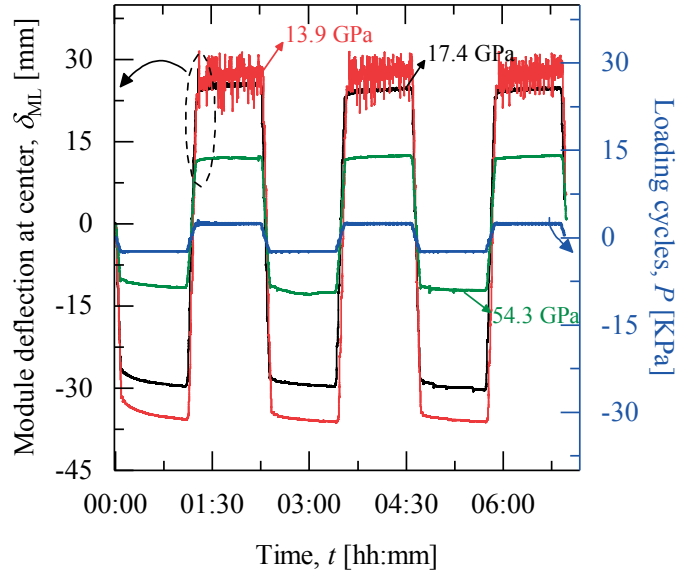
Figure 7.11 – Measured module deflection obtained during a static mechanical load test for the lightweight PV module manufactured with different equivalent Young's modulus: (1) EVA-based sandwich (13.9GPa), (2) PO-based sandwich (17.4GPa), and (3) a reference glass-glass structure (54.3GPa).

cell cracks are detected as can be seen in the EL images (figure 7.12). Regarding the **EVA-** (plate 2) and **polyolefin-based sandwich structure** (plate 3), we observe a curvature radius of 244 and 302 cm, respectively. The noise present on the deflection measurement in the case of the low-rigidity backsheet came from the difficulty of the vacuum cups to keep the vacuum on the module due to the roughness of the frontsheet surface. The EL images show that the module produced with a backsheet with an E_{eq} close to 17 GPa, as predicted by the FEM model, does not have any solar cell cracks or damages, showing only -1% maximum output power loss.
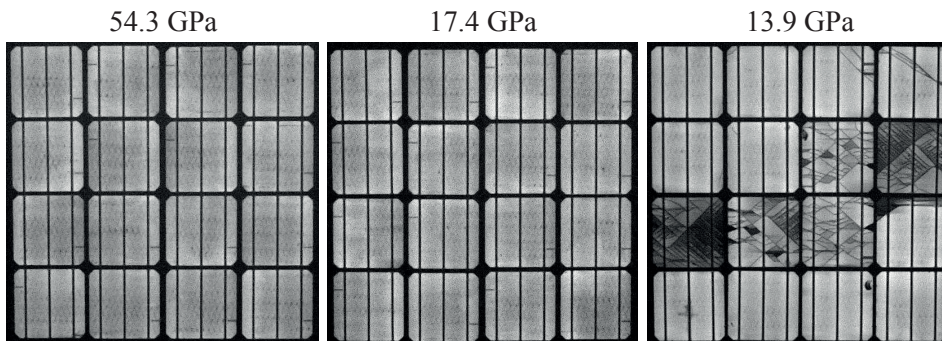
Figure 7.12 – EL images, obtained for a static mechanical load test, of lightweight PV modules with different E_{eq} values: an EVA-based sandwich (13.9GPa), a PO-based sandwich (17.4GPa) and a glass-glass structure (54.3GPa).
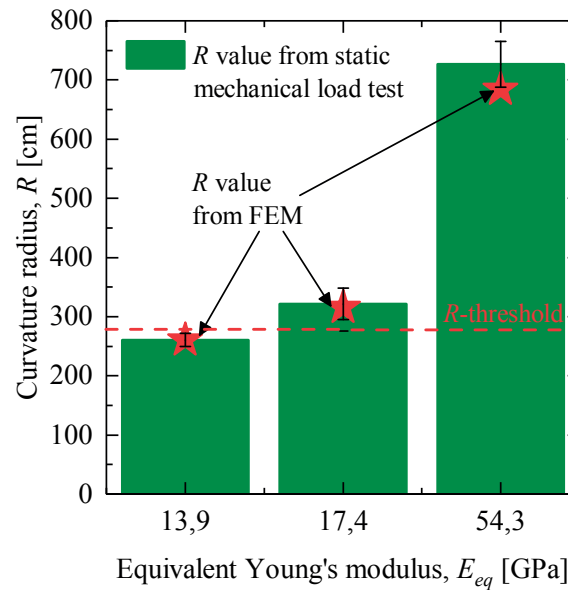
Figure 7.13 – Summary of the curvature radius calculated from the maximal deflection obtained from a static mechanical load test for plates with different rigidity. Red symbols represent the curvature radius calculated from the deflections simulated in FEM. The R-threshold represents the minimum curvature radius solar cells can sustain without cracking.

However, the solar cells of the module produced with an EVA-based sandwich (13.9 GPa) show many cracks and a power loss of -3%. In fact, the curvature radius of this structure is lower than the curvature radius threshold, inducing solar cell to crack once the R-threshold value is crossed. Comparing the deflections simulated in FEM and the static mechanical load test presented previously (see figure 7.10), we realize that simulated deflections are slightly higher than the measured deflections during the loading phase (+2400 Pa). However, the simulated deflections fit well with the results during the suction phase of the static mechanical load test (-2400 Pa). This is due to the fact that the values obtained during positive loading are slightly different from the those obtained during negative loading. These results suggest that there are some effects that occur during the test (asymmetry of mounting, position of sensors) that are not being considered in the simulations or inhomogeneous pressure or suction is applied during the experimental test. Still, if we compare the R-values calculated from the static mechanical load test and R-values obtained from the FEM model, they match very well (see figure 7.13).

Another reason for discrepancies between the simulations and the experimental test is that we do not consider the viscoelasticity of the composite sandwich structure. This explains why our simulated deflection is constant over time. The viscoelasticity behavior is time-dependent [219] so, at the moment 2400 Pa is reached for the first time, the curvature depends only on the elasticity of the plate. Over time, this curvature will slightly increase due to the viscoelastic component of the plate. However, it is important to note that, once the load is removed, the plate returns to its original state, meaning that besides the deflection, the plastic

regime is not reached. Additionally, considering our polyolefin/aluminum-based lightweight

PV module, the stiffness of a 1.6 m × 1 m module is around 389 N·m^2, enough to be installed on a building without the need of an extra mounting system, as required by *DIN 18008*. This standard defines that a plate installed in a façade should be fixed in two rail bars separated by ≈ 60–80 cm. For such configuration, in order to have a bending depth (C_d) of less than 1 cm (C_d=L/100), the plate must have a minimum bending stiffness of around 370 N·m^2. This value can easily increase by changing the core thickness without significantly affecting the final module weight.

Influence of the PV mounting structure

The four-clamp mounting used in the static mechanical load test is not a conventional mounting system for conventional opaque façade cladding panels. Usually, these panels are fixed to two separated rail bars with a distance of around 60 cm [220, 221]. For this reason, the static mechanical load test is repeated with a mounting system that mimics the use of rail bars: the lightweight PV module is glued to two aluminum bars using a structural adhesive glue. After the installation, we applied one loading cycle of 2400 Pa. The curvature radius of the selected module (with an E_{eq} of 13.4 GPa), which previously showed a curvature radius of 244 cm, increased to 1323 cm. This result shows that, besides the importance of backsheet rigidity previously discussed, the PV mounting structure is another key factor limiting the mechanical stress to a safe level. Different mounting systems are currently being investigated
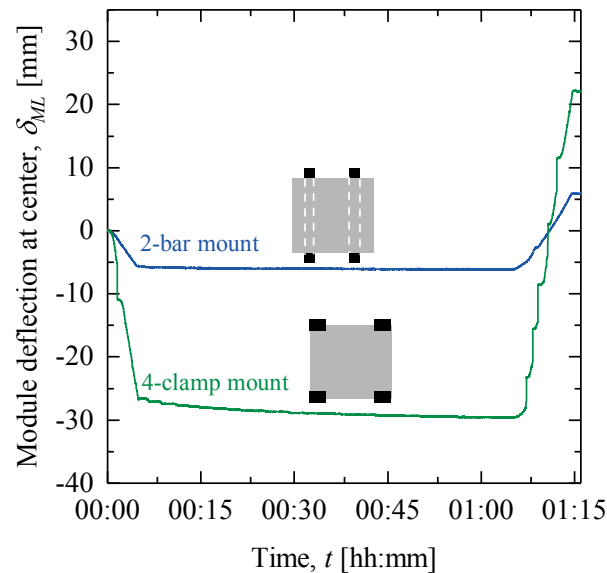
Figure 7.14 – Module deflection of lightweight PV module under a static mechanical load test with two different mounting systems: a four-clamp mount and a two-bar mount.

(more details can be found in Chapter 8).

7.4 Conclusions

This work demonstrates the production of a reliable glass-free rigid lightweight PV modules that are resistant to both hail and mechanical loads, thanks to a balanced trade-off between frontsheet rigidity and backsheet stiffness.

To pass the hail test designed for the qualification of solar panels, the lightweight modules require: (i) a low-stiffness backsheet (not always the preferred solution because it might reduce the maximum load a module can support), and (ii) a high-rigidity frontsheet ($G^* \geq 350$ MPa). We further demonstrated that durability of lightweight modules is not affected by the use of a stiff frontsheet. In fact, the modules with an ionomer-based frontsheet showed a better performance than EVA-based frontsheet under extended cycles. By using the DMA and four-point bending to analyze frontsheet and backsheet properties, we were able to reduce the number of tests and cost and, most importantly, obtain faster feedback on the proposed module design.

Additionally, we developed a method that provides a fast and low-cost feedback about sandwich design that might survive the static mechanical load test. This sequence consists of simulating in FEM the required plate stiffness (E) to maximize the curvature radius to a safe level (from our work we found that R >> 275 cm for Al-BSF c-Si solar cells) and manufacturing structures and calculating the equivalent mechanical properties (namely E_{eq}) by a four-point bending test that match the E needed. This method was validated by experimental tests where we demonstrated that a lightweight module (81 cm × 81 cm^2) with an equivalent Young's modulus of 17.4 GPa successfully passed ±2400 Pa without any cracked solar cells.

8 Special requirements for PV modules in the built environment

Summary

The development of lightweight PV modules for BIPV application requires that modules comply not only with PV standards but also with building safety standards. In this chapter we show that our designs successfully pass the demanding tests in the following regulations: (1) special requirements for building products (*ISO 12543*), (2) fire requirements (*CEN/TS 1187*), and (3) requirements to pass the static mechanical load test with a minimized mounting system (*Velcro*). This chapter also gives an overview of the cell and module operating temperatures for our proposed modules with a low- or a high-thermal-conductivity core. The use of an aluminum core is an advantage that facilitates the processing, and also prevents excessive heating of the cell.

8.1 Introduction

Integration of PV into the skins of buildings is a steadily growing market. Europe currently leads the worldwide BIPV market with 41% of total installations, followed by the USA (27%) [222]. This market penetration is mainly due to the increasingly demanding legislation related to energy performance in buildings [19]. Nevertheless, the BIPV market growth is still moderated and faces barriers to its adoption such as questionable flexibility in design, long-term reliability of the technology, compliance with all building norms, and cost-effectiveness.

BIPV components must simultaneously satisfy electro-technical requirements as well as regulations regarding construction products. The *EN 50583* standard aims to bridge this gap and sets, for the first time, relatively clear requirements, at least for the European market. However, many blocks in the requirement table refer to other building construction norms,

e.g. glass in buildings, building design, curtain walls, fire classification or sustainability. The main standards used for PV module certification related to construction sector are

- Glass standards: *EN 1279*, *EN 15434*, *EN 13022* (insulated glazing), *EN 14449* or *ISO 12543* (laminated glass) and *ISO 11485* (curved glass)

- Curtain wall standards: *EN 13830*

- Ventilated façades: *ETAG 034*

- Safety in case of fire: *EN 13501* (Fire classification: external fire exposure to roofs tests) and *CEN/TS 1187* (Test methods for external fire exposure to roofs)

- Roof coverings: *EN 14963* (Classification, requirements and test method)

- Other standards: *EN 1873*, *EN 13501*, *EN 410*, *EN 673*, *EN ISO 6946* and *EN 12600*

From these standards, *ISO 12543 — Glass in buildings: Laminated glass and laminated safety glass* [223] proposes a set of durability tests that aim to analyze the influence of temperature, humidity and irradiation on building elements and *EN 13501 / CEN/TS 1187 — Fire classification: external fire exposure* proposes test methods to evaluate the fire performance requirements applied to roof covering materials. We use the two standards to evaluate the stability of our lightweight PV module under different building requirements.

Additionally, an electrical fire within the module or array can be caused by a localized overheating that might occur due to, e.g., partial shadowing, which is particularly critical in façade installations. A high module operating temperature, which can still be even higher for BIPV applications, can accelerate module failure. We consider different inclination angles with different back insulation structures and different module designs to further study the influence of temperature on our lightweight PV modules.

8.2 Durability tests required by the construction sector: *ISO 12543*

In the building sector, when there is no perfect matching norm to the product under development, designers often adopt glass norms for other components that are well standardized. Thus, despite the fact that our lightweight modules are not transparent or made out of glass, this standard can still provide a set of durability tests that allow us to evaluate our modules against thermo-mechanical stability set by building requirements. This standard suggests to use samples sizes representative of the final product. However, we observed that from the PV accelerated-aging tests the performance of small modules were equivalent to the large modules we decided to perform this study with two-cell module. In this standard, there are three main tests to evaluate the durability of building elements.

8.2.1 Test methods to evaluate the durability of components

For the **high-temperature test** we manufactured a set of three lightweight two-cell modules (40 cm × 20 cm). These samples are composed of an ETFE frontsheet, solar cells (c-Si Al-BSF with three busbars) protected by EVA and an EVA-based sandwich structure backsheet. Samples were introduced into an oven at 100°C and, after 30 minutes of stabilization, the samples were left inside for 16 hours. During the test, the samples were placed vertically, as building façade elements.

The same samples used for the high-temperature test were further tested under the **humidity test**. Samples were placed in a vertical position over a closed water bath in a reservoir for two weeks. The reservoir was kept at 50°C ± 5°C and 100% RH. To pass both tests the samples should not show delamination larger than 20 mm from the borders. The I-V curves and the EL images are recorded after the test.

An **irradiation test** is also included in this standard and consists of exposing samples to an AM1.5 spectrum for 2000 h (spectrum shown in figure 8.1). During the test, the temperature of the samples should be ≈45°C ± 5°C. To pass this test the samples should not have more than 15 mm delamination from the edge and the transmittance after the test should not change more than 3% from the initial transmittance value. We were unable to perform this test at that time due to equipment limitation. Thus, we performed a weathering degradation using Xenon arc lamps which present a similar spectrum to an AM1.5 between 300 and 400 nm (see figure 8.1). The samples were degraded at 65°C/20% RH with an irradiance of 0.8 W/(m^2·nm) at 340 nm. This test was realized according to *IEC TS 62788-7-2* [224]. In our case, the degradation due to UV is the most critical consideration, since polymers are relatively sensitive to this
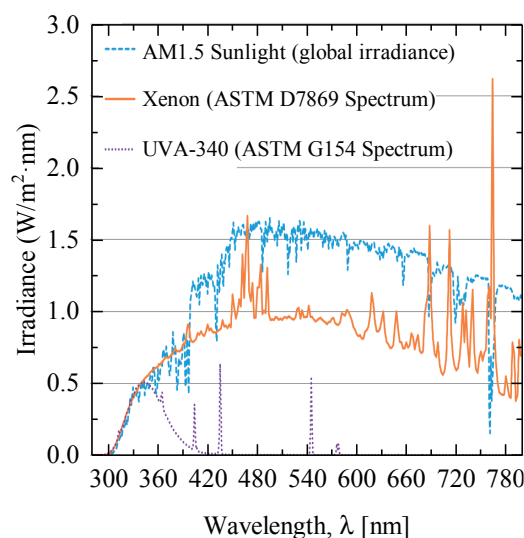
Figure 8.1 – Spectral irradiance power distributions of solar (AM1.5), xenon arc and fluorescent UV light sources (image adapted from [224]).

Table 8.1 – Summary of all sample configurations prepared for irradiation testing from *IEC TS 62788-7-2*.

Sample ID	Frontsheet	Encapsulant	Backsheet
A (reference)	Glass	EVA	Glass
B (reference)	Glass	Ionomer	Glass
C	ETFE	EVA	Glass
D	ETFE	Ionomer	Glass

part of the spectrum. For this test, we produced a 5 cm × 5 cm sample based on a glass-glass and ETFE-glass configuration, as represented in table 8.1. Samples were introduced into the chamber and analyzed at regular intervals using a spectrophotometer as described in Chapter 2.2.8. The transmittance results were used to calculate the yellowness index and the relative color change (increase in YI normalized by the initial value).

8.2.2   Results and discussion

Figure 8.2 shows an example of the results obtained after the high-temperature and high-humidity test. All two-cell modules successfully passed the tests without any power loss, as can be seen in figure 8.2a. From the EL images (figure 8.2b) we observe that no changes in the solar cells are detected after both tests. Moreover, no delamination or bubbles are

(a) I-V curves

(b) EL images
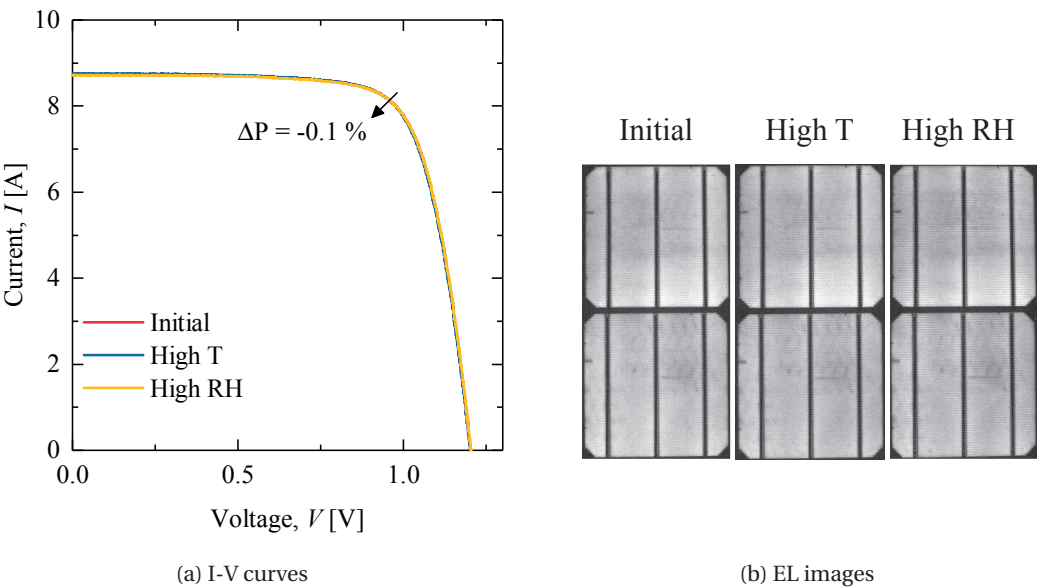
Figure 8.2 – I-V curves and EL imaging of lightweight PV modules after subjected them to different durability tests present on the *ISO 12543*: high temperature test and high humidity test.

present. The optical measurements (figure 8.3) performed after an accelerated-aging test show a higher increase in YI for the glass-EVA-glass configuration compared to the ETFE-EVA-glass configuration. In fact, discoloration of the EVA occurs due to the UV-induced color formation of the additives in EVA combined with oxygen bleaching from the UV damage. However, when two impermeable layers are used, the yellowing process overwhelms the oxygen bleaching mechanism. These mechanisms are already reported in literature [225, 226] where, in some cases, we can find a yellow area concentrated at the center of the solar cells with a photo-bleached perimeter all around the cell, where oxygen diffusion was effective. For the ETFE-EVA-glass configuration, the YI does not change significantly because the oxygen migration from all area surface (ETFE side) avoid the UV damage. This yellowing is not observed with the ionomer. Moreover, the increase of *YI* after weathering aging is lower than 10% after 3200h.
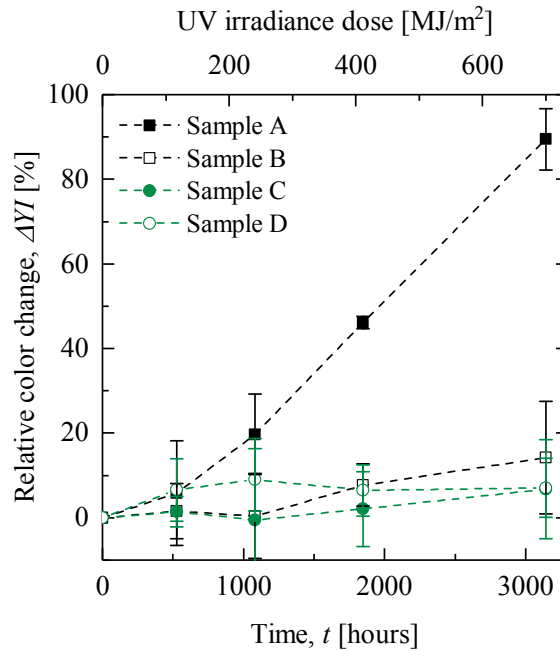
Figure 8.3 – Yellowing index change with accelerated weathering test of samples made of: glass/EVA/Glass (sample A), Glass/ionomer/glass (sample B) ETFE/EVA/glass (sample C) and ETFE/ionomer/glass (sample d). More details in table 8.1.

In conclusion, our glass-free lightweight PV modules passed successfully the tests required for safety glass without critical defects.

8.3 Fire resistance tests: *CEN/TS 1187*

From the *CEN/TS 1187* standard, four different test methods can be selected, depending on the type of activator element and test conditions:

1. Method 1: with burning brands (presented in figure 8.4).
2. Method 2: with burning brands and wind.
3. Method 3: with burning brands, wind and supplementary radiant heat.
4. Method 4: a two-stages method incorporating burning brands, wind and supplementary radiant heat.

8.3.1 Test method procedure: Method 1

For a preliminary test we select the method with burning brands (Method 1). This method consists of filling a basket with approximately 600 g ± 10 g of wood wool; the filled basket is then positioned parallel to the nominal slope (45° tilt) at 10 mm from the surface of the specimen so that this position is maintained throughout the test. The fire is set to the brands from the bottom side. We used 0.81×0.81 m^2 sixteen-cell modules with a polyolefin/aluminum-based backsheet and an ETFE/EVA-based frontsheet. We performed the test on the front side of the module to represent a fire ignited outside the building (Position 1), on the back side of the module to represent a fire ignited from within the building (Position 2), and in between two modules placed side-by-side (Position 3). To pass the test, no glowing or burning part of the PV modules may fall from the test rig, the flame should auto-extinguish and flame may not spread more than the maximum allowed for the different class rating.

Position 1   Position 2   Position 3

Figure 8.4 – The test setup to evaluate the fire resistance include a wood support, a lightweight module and a basket with brands, in accordance with *CEN/TS 1187* (Method 1).

8.3.2 Results and discussion

Figure 8.5 shows the modules after the fire test. In Position 1 and Position 2 we observe that the burned area stays localized at the center of the module where the burning brands had been. Moreover, the fire auto-extinguished. However, during the test, we observed some materials dropping from the burning area in Position 1: the polymer present in front of the cells started to melt and, due to the vertical position, the melted materials started to drip. In Position 2, the ETFE stayed intact and only small delamination between the cells and ETFE is observed, without any material dropping. When the fire was placed between the modules (Position 3), it

spread easily inside the modules and started to consume the materials. In this case, human intervention was needed to stop the fire. As can be seen in figure 8.4, the modules used in this test were frameless; thus the fire could easily spread inside the backsheet and consume the sandwich adhesive and matrix skin.

Position 1	Position 2	Position 3
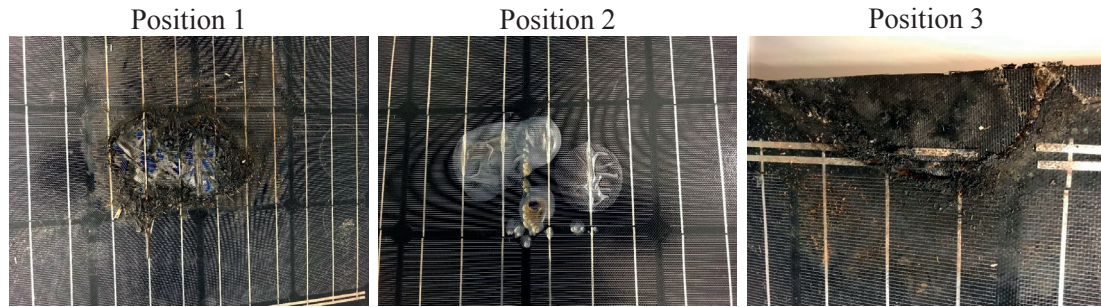
Figure 8.5 – Results obtained from the fire test using Method 1 from *CEN/TS 1187*. When the fire was started on the frontsheet (Position 1), the frontsheet melted and some materials start to drip but no human intervention was needed to extinguish it. When the fire was started on the backsheet (Position 2), only small delamination of the frontsheet occurred. When the fire was started in between two modules (Position 3) the fire spread inside the module and started consuming it. In this case, human intervention was needed to extinguish fire.

The results of this preliminary investigation are encouraging and show that our lightweight PV modules may resist a fire and be compliant with *CEN/TS 1187*. This design will be the subject of further investigations with regard to the final product and configurations, e.g. frame, junction box, etc.

8.4 Innovative mounting system: Velcro

The four-clamp mounting system — commonly used with ground-mounted field installations — is not conventional used for BIPV. To complement the reduced weight of lightweight modules we propose the use of a mounting system that allows for a simple and fast installation process: *Velcro*. This binding material is not used in the built environment. Nevertheless, we tested it because it may provide considerable advantages in combination with our lightweight solar modules: it will reduce the labor and installation time, it is a simple and clean mounting system, it is easy to remove (in case of needed PV or roof or façade maintenance), and it can resist high loads (average tensile disengagement of 207 KPa).

8.4.1 Methods to evaluate new mounting system

To study the maximum force needed to open the two *Velcro* bands, an adhesion test using tensile test equipment was performed. For this test, coupons of 5 cm × 2.5 cm were cut from a *Velcro* strip and glued over two compressive plates installed in a tensile tester shown in figure 8.6. A load cell of 20 kN and a speed test of 5 mm/min were used for this measurement.

The same sample was loaded until rupture 15 times to evaluate the loss in adherence between the two *Velcro* bands.

From the adherence test, the correct quantity of *Velcro* was calculated and used in a static mechanical load test. For security reasons, a *Velcro* area of 0.1 m^2 was used (safety factor of 2) to support a plate of 0.81 × 0.81 m^2. This amount of *Velcro* was installed and used to bond the back of the module to a metal support. A standard mechanical load test was performed (details in Chapter 2).
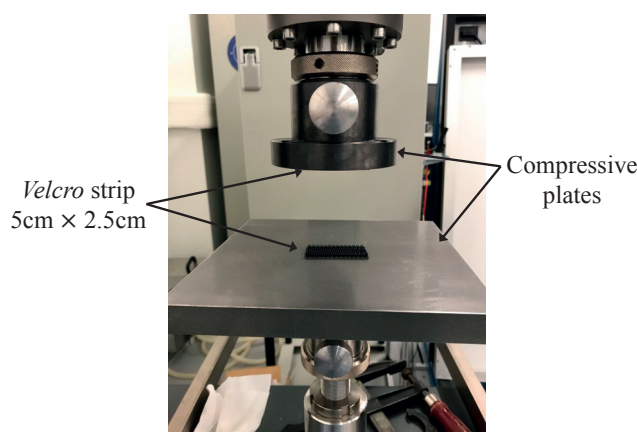
Figure 8.6 – Tensile adhesion test setup used to quantify the adherence between two *Velcro* bands. Photography show the two compressive plates in which the *Velcro* strip of 5 cm × 2.5 cm are glued on.

8.4.2   Results and discussion

Figure 8.7 shows the *Velcro* adherence strength measured with the two configurations where a strong difference is observed. In a tensile configuration, the small pins are pulled until a plateau load is reached ($\approx$1.7 N/cm^2). This plateau corresponds to the alignment of all pins. After this value, the load increases until the two *Velcro* bands are completely debonded ($\approx$19.8 N/m^2). The repetition of this test 15 times showed that the value of the plateau is kept constant but the maximum load is reduced by approximately 40% (between test 1 and test 15). Thus, in order to have confidence in the *Velcro*'s ability to function as a mounting system, we decided to consider the value of the plateau as the minimum required adherence strength to support the 2400 Pa. This means that in our 0.81 × 0.81 m^2 plate a minimum *Velcro* area of 0.05 m^2 is needed.

In order to validate these results, the mechanical load test was performed: *Velcro* was used to glue the back side of the module in a square/cross configuration to an aluminum plate (see the inset in figure 8.7b). A total *Velcro* area of 0.1 m^2 is used (security factor of 2). Figure 8.7b shows the load cycles applied to the module affixed with *Velcro*. Note that this configuration survived the mechanical load test without debonding. The noise present during the suction phase (+2400 Pa) is due to the difficulty to keep a constant vacuum when the module frontsheet has

(a) Adherence study.

(b) Mechanical load test.
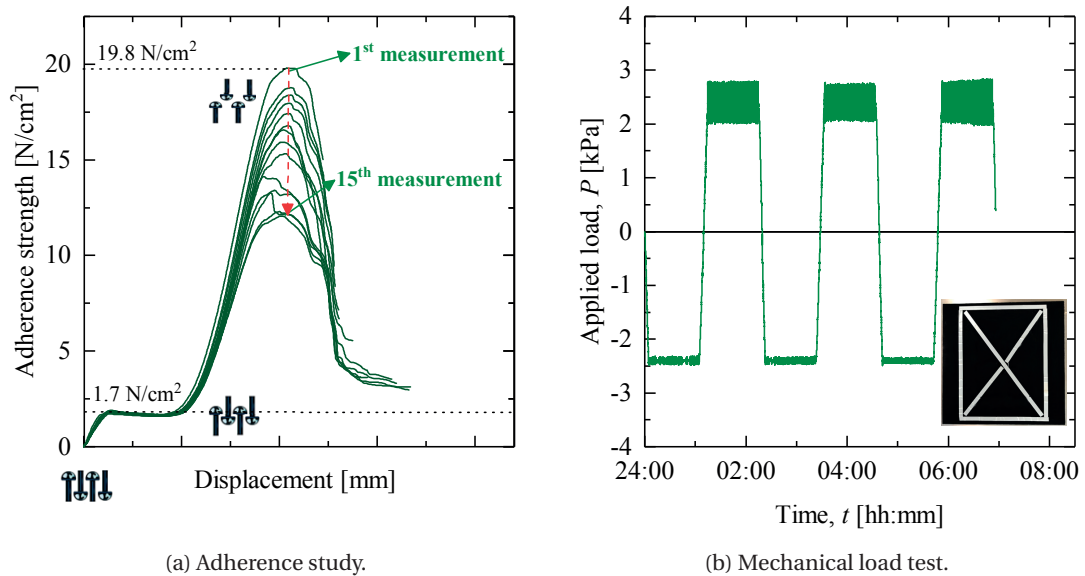
Figure 8.7 – (a) Adherence strength of *Velcro* in a uniform tensile load test; (b) mechanical load test using *Velcro* with an area of 0.1 m^2.

a textured surface.

Preliminary results indicate that covering only 7.6% of the back surface area with *Velcro* is enough to pass a standard static mechanical load test (±2400 Pa).

8.5 Monitoring of outdoor operation temperature (OT)

Table 8.2 and figure 8.8 shows the setup built to study the influence of the operating temperature as a function of the design, incidence angle and insulation system. Six one-cell modules (PERC solar cells with five busbars) of the following module types were manufactured: (i) glass-glass configuration (reference sample), (ii) polyolefin/aluminum-based and

Table 8.2 – Installations used for outdoor temperature monitoring. All three module configurations were installed following the same guidelines.

Configuration	Angle of installation (°)	Insulation
	0	yes
	0	no
PO/Al-based	45	yes
lightweight module	45	no
	90	yes
	90	no

119

Figure 8.8 – Mock-up installation for monitoring the cell and module operating temperature. Three different module designs are analyzed: glass-glass configuration, PO/Al-based and PO/aramid-based lightweight module. This installation simulates two different types of integration: a well-ventilate installation and a non-ventilated installation.

(iii) polyolefin/aramid-based lightweight module. All modules were laminated with one thermocouple at the back of the solar cell (to monitor the cell temperature, T_{cell}) and another at the back of the composite sandwich structure (to monitor module temperature, T_{module}). Temperatures were monitored in V_{oc} conditions. After manufacturing, modules were installed at one of three angles (0°, the optimum 45°, or 90°), and with one of two insulation systems (an air gap or complete insulation on the back side), as seen in table 8.2. A rigid 3-cm-thick insulation panel in polystyrene foam especially developed for external thermal insulation of buildings was used to fully insulate the PV modules.

8.5.1   Results and discussion

Figures 8.9 and 8.10 show, respectively, the irradiance at different tilts and the operating temperature of the samples installed on the outdoor monitoring station (on the roof). From these results we can state that:

- For all module designs, the module temperatures (T_{mod}) obtained at 0° and 45° are similar. However, a significant decrease in temperature is observed at 90°. This decrease is due mainly to the decrease in the irradiance at this angle (a maximum of 522 W/m^2 which corresponds to only 52% of the irradiance on modules installed at the optimum tilt). This is especially noticeable because the measurements were performed
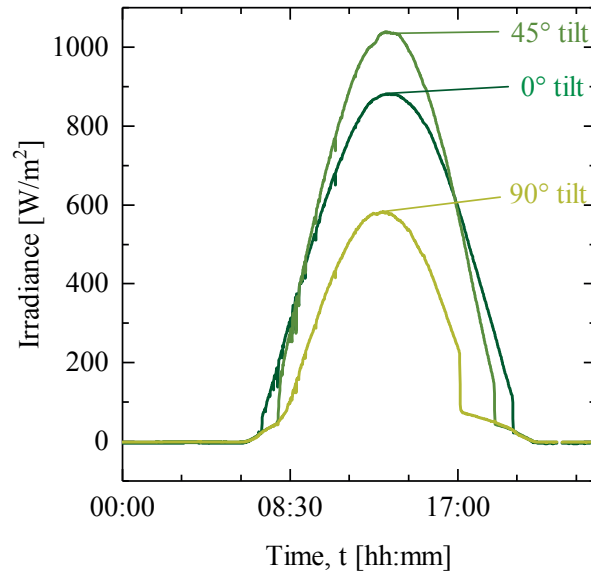
Figure 8.9 – Irradiance measured for the different tilt angles.

in summertime.

- The operating temperatures of the module were higher when they were insulated on the back side. A maximum ΔT of 13°C is observed between the insulated and non-insulated modules.

- The maximum T_{module} of the aluminum-based lightweight module is similar to the maximum T_{module} reached by the glass-glass configuration. Moreover, a very small difference between T_{cell} and T_{module} is measured (a maximum ΔT of 3°C). The aluminum-based lightweight module shows good heat dissipation from the cell towards the module outside.

- The T_{module} of the aramid-based lightweight module is similar to the T_{module} of the other two configurations (only 1°C higher). However, due to poor heat transfer in the backsheet the T_{cell} is higher than for the previous cases (+5–7°C).

- The temperature difference between T_{cell} and T_{module} of the aramid-based module is also much higher: in some cases (optimum tilt) a ΔT of 14°C is observed. Due to the low thermal conductivity of the aramid core, the heat is not dissipated through the backsheet causing a higher T_{cell}.

These results show the importance of the correct module design to optimize the energy production of the PV module. The use of an aluminum core is an advantage not only for processing and cost, as explained in the previous chapters, but also prevents excessive operating temperatures within the cell, which will otherwise be penalized in terms of performance by the use of a thick backsheet structure.
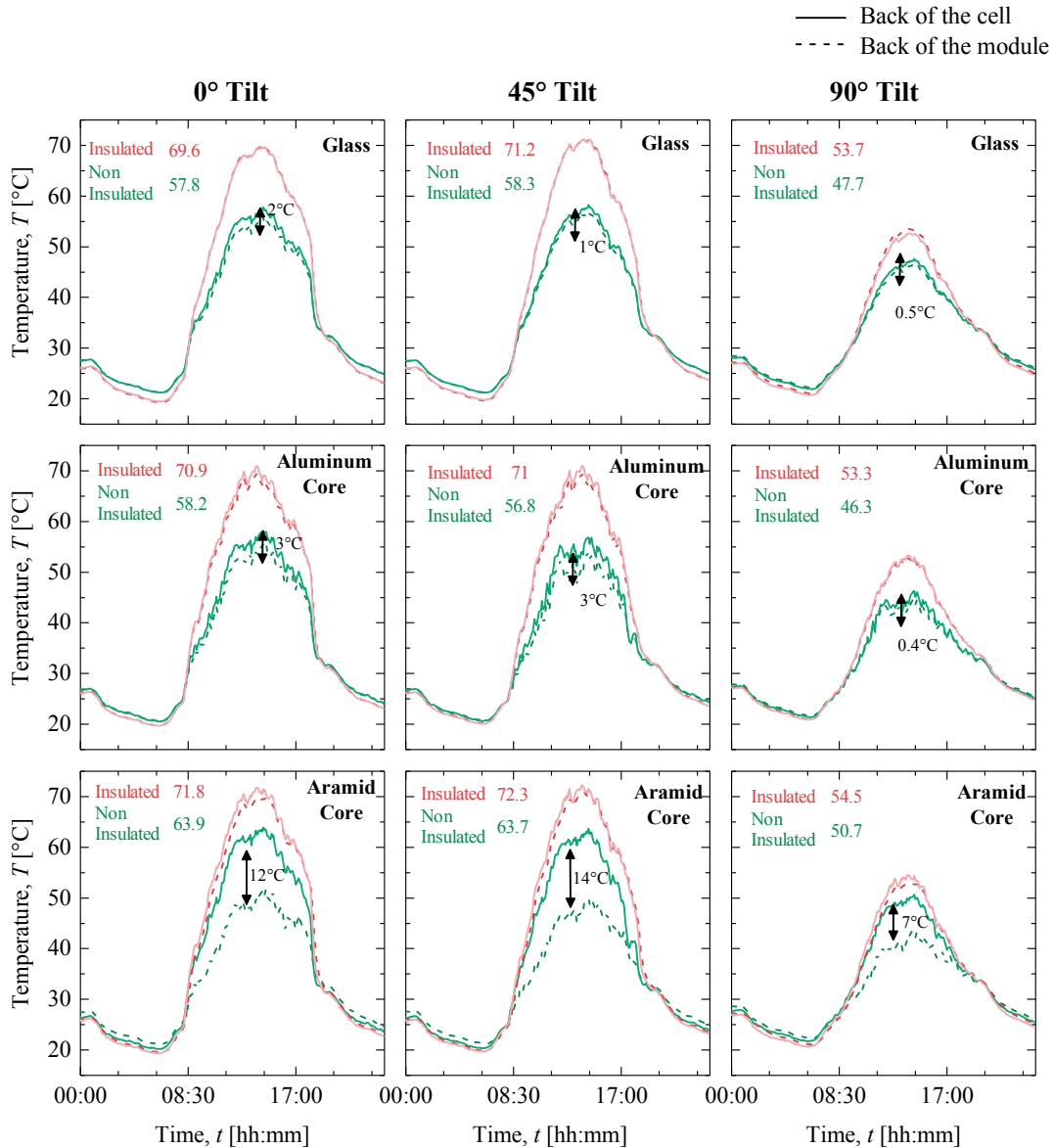
Figure 8.10 – Temperature monitoring of the different installations (0°/45°/90°) for a typical cloudless summer day. The cell temperature is represented in red and the module temperature in green. ΔT represents the difference in the cell temperature between modules with full insulation (BIPV) and those with a well-ventilated rear.

8.6   Improvement of aesthetics

Our focus has been to improve the thermo-mechanical stability, reliability and performance, rather than the aesthetics, of lightweight PV modules. However, to meet the expectations of architects and designers, the visual appearance of these devices can easily be modified and improved in order to increase their acceptance for integration into the built environment.

These modules can be optimized to have a completely black matte appearance (by using back-contacted solar cells, attractive for roof installation) or a uniform white appearance by using a white film from *Solaxess* [227] (attractive for façade installations). With these novel solutions, we reach a final weight of 6–6.5 kg/m^2 (including a frame).

Figure 8.11 – Improvement of aesthetics of our glass-free lightweight PV module for BIPV applications. This photography compares black matte and uniform white lightweight PV modules with a standard glass-glass c-Si module.

8.7 Conclusions

This chapter demonstrates that our lightweight PV module can pass certain durability and safety tests required by the building construction industry:

- **Durability tests** – Two-cell modules were tested under high temperature and high humidity. The modules passed both tests with negligible power loss (-0.1%). From the visual inspection no delamination or bubbles were identified. The weathering test induced a significant color change in the glass-EVA-glass configuration mainly due to the degradation of EVA under UV light. However, the ideal lightweight PV module frontsheet (ETFE/ionomer) did not show a critical color change (≈7%) after 3200 h.

- **Fire tests** – The glass-free lightweight PV modules showed good resistance to fire. The frontsheet and backsheet structures self-extinguished the fire itself. Nevertheless, some material was observed to drop from the burning area. These results suggest the need for further developments in the design of the lightweight modules: (i) the test must be performed using an ideal frontsheet (ionomer) to possibly avoid dropping material from the burning area, and (ii) the test must be repeated using a lightweight module with a frame to reduce risk of fire spreading inside the module.

Finally, temperature monitoring under real operating conditions shows that in a ventilated mounting configuration, an aluminum core is preferred to aramid core, and can lead to a lower cell operating temperature than a glass-glass configuration. Temperature monitoring also showed that, in an insulating mounting configuration, there is no difference between the two tested cores. However, the aluminum core is still preferred over aramid thanks to the short manufacturing process, higher shear stiffness and lower price.

9 General conclusions and perspectives

9.1 General conclusions

9.1.1 Failure modes of commercially available lightweight modules

The commercial lightweight solutions bought for this study showed a significant degradation under accelerated-aging tests. These results indicated that the tested lightweight designs do not meet expectations, especially in the case of the certified products. This observation of their weak thermo-mechanical behavior, motivated us to start our own development of glass-free PV modules. We developed a rigid solution because rigid modules seem to have higher stability under high stress, which is essential to pass relevant PV qualification tests.

9.1.2 Design, manufacturing and properties of the lightweight modules

Standard glass/glass BIPV modules have a weight in the range of 15–20 kg/m^2. In this thesis, we demonstrated that a glass-free rigid lightweight PV module ($\leq$6 kg/m^2), can be processed following standard PV lamination guidelines in a relatively short manufacturing process. The proposed design is compliant with the most-demanding tests in *IEC 61215*, thanks to the selection of a rigid and stable composite sandwich structure backsheet. Additionally, we showed how our composite sandwich backsheet and a full solar module stack can be manufactured simultaneously with conventional processes (lamination) used in the solar industry. This sandwich structure is composed of:

- **Symmetric and balanced skins** — this design reduces bending and twisting of the structure when subjected to high temperature and humidity.

- **Polyolefin foil as the sandwich adhesive** — its high stiffness and melting point that is low enough to ensure a good viscosity during manufacturing provide good adhesion and stress transfer between the sandwich components when subjected to high stress.

- **Aluminum honeycomb core** — its high thermal conductivity ensures a simplified man- ufacturing process, and a lower operating cell temperature, even in the presence of a

thick backsheet. Its good thermal properties together with its low price and high shear mechanical properties make this material the ideal core for our modules.

We also demonstrated that other types of adhesive materials (EVA and ionomer) can be used with an aluminum honeycomb core and still be processed following standard lamination guidelines. However, due to their low intrinsic mechanical properties or low melting temperature, such sandwich structures showed lower bending stiffness, or bending under thermal stress. Finally, we showed that the use of an aramid honeycomb core also allows for the manufacture of a composite sandwich structure using lamination guidelines, while keeping good mechanical properties. The disadvantage of these structures is that, due to their low thermal conductivity, aramid-based sandwiches require a double lamination process to enssure that both adhesive layers have similar properties.

9.1.3 Durability of lightweight modules

In Chapter 6, we demonstrated that two-cell modules based on a polyolefin/aluminum sandwich structure have a remarkably low power loss after thermal cycling, damp heat, humidity freeze, and PID test, even when using solar cells prone to PID. These promising results motivated us to scale up the two-cell module to a sixteen-cell module. These modules were subjected to a different test sequence predefined by *IEC 61215* (Sequence C, Sequence D and Sequence E), after which we identified a reduced power loss ($\leq$-5%) and no major visual changes. These results showed the potential of our design to successfully comply with relevant PV qualification standards.

Despite the fact that our solutions passed the hail test, small cracks were detected by EL imaging. In Chapter 7, we demonstrated that cracks due to impact can be avoided by tuning the backsheet and frontsheet rigidity. We demonstrated that by selecting a sandwich backsheet with an equivalent Young's modulus of 17.4 GPa and a frontsheet with a high rigidity ($E^* \geq 350$ MPa), the modules were able to pass the mechanical stress tests (hail and static mechanical load test) without significant power loss, cracked cells or other major visual defects.

The testing of new designs under a static mechanical load requires big modules (ideally 1.6 m^2) and many samples (minimum three modules per design to have representative results). To accelerate the pre-qualification of lightweight PV modules under mechanical stress, we developed an FEM and proposed a multi-step sequence that provides reliable, cheap and fast feedback about backsheet structure designs.

9.1.4 Special requirements for PV modules in the building industry

The development of PV modules for building integration requires compliance with electrical performance standards (*IEC 61215* for solar modules) and building and safety regulations.

Our lightweight modules were subjected to different safety tests, such as a fire test (*CEN/TS 1187*). Preliminary results were satisfactory and provided useful indications on how to further optimize the design of the modules. These results showed that, by including a protective frame, the spread of a flame inside the module can be reduced.

Finally, carefully monitoring the outdoor operating temperature of different module configurations and for different typologies of installation (ventilated and fully integrated), we observed that the cell temperature of the lightweight module with a high-thermal-conductivity honeycomb core is very close to the temperature of a reference glass-glass module, in both the insulated and ventilated configurations. Additionally, no significant difference between the cell and module temperature was noticed: despite the use of a thick backsheet, the high-thermal-conductivity core allows for an efficient heat dissipation from the solar cells towards the back side of the module. In contrast, the aramid-based sandwich structure showed a ΔT of 14°C between cell and module temperature, which further reinforce the choice of the aluminum core.

9.2 Perspectives

9.2.1 Design and manufacturing process

During this thesis, the composite skins were manufactured, before being laminated, in a wet lay-up technique, requiring approximately two days for the full manufacturing process. The use of *Prepregs* could save more than 80% of the time spent on material preparation: they could be cured and post-cured at the same time as the lamination process. Additionally, these *Prepregs* could be used as the adhesive between the core and the skin. The potential of this new material should be validated by studying the stability of its sandwich mechanical properties (stiffness, composite failure modes, adhesive meniscus area, etc.) after processing and after the accelerated-aging test.

In view of a commercial exploitation, there are still few steps at the module design level, such as: (1) scaling up the size to large-area modules (1×1.6 m^2) (the structural design must be verified for large composite structure sizes), (2) defining the application and optimizing the mounting structure, and (3) designing the junction box, frames and diodes. We recommend the direct inclusion of the junction box inside the core of the sandwich composite structure. This will allow for easier module mounting, which is very important in BIPV installations.

9.2.2 Compliance with relevant PV norms

It would be interesting to perform Sequence A and Sequence B from *IEC 61215*. From these sequences, the only test that might be critical is the hot spots test (Sequence B). Hot spots failures might create a local overheating that can induce melting and deterioration of the module materials. From the results of this thesis, we expect no critical defects with the other

tests in these sequences because most of them do not depend on the module design but, instead, on the cell technology.

After scaling up the proposed design to standard module size, we suggest that the design be evaluated under all required building directives, such as: (1) PV qualification standards (*IEC 61215* for module design qualification and IEC 61730 for safety qualification), (2) *Construction Products Regulation EU No 305/2011*, (3) *Low Voltage Directive 2006/95/EC* and (4) *Electronic Electromagnetic Compatibility Directive 2014/30/EU*. From the results of this thesis, we expect that the most-demanding tests are included in the PV qualification standards, which we proved our design could handle.

9.2.3 Modeling of mechanical behavior and module lifetime

The FEM model developed in Chapter 7 could be further improved by studying different module sizes, studying different mounting systems (e.g. *Velcro*), including viscoelasticity of the polymer materials, and including the solar cells and module frontsheet. We have already taken the first promising steps in this direction.

With the goal of predicting the effect of the higher operating temperatures of BIPV installations (up to 30°C higher than a well-ventilated installation) on the lightweight module performance, it would be useful to develop a model to simulate its lifetime as function of operating temperature. The development of an outdoor installation could help to identify the failure mechanisms induced by such high temperatures. Once identified, we could try to reproduce this failure in an indoor stress test and, based on the activation energy and degradation rates identified, propose mathematical models to simulate intrinsic property losses (e.g. loss in output power). Figure 9.1 proposes a basic sequence to follow during the development of a predictive model.

9.2.4 Improvements for building integration

In view of building-integration applications, our lightweight module design could be further improved by:

- The use of **transparent** or **translucent** backsheets — these structures are especially attractive for applications where diffusion of daylight is required (e.g. translucent building envelopes) [148, 228–230]. The possibility to develop translucent structures that could be laminated in standard lamination guidelines using c-Si solar cells will strongly boost the acceptance of lightweight PV elements over standard glass-glass modules.

- The development of **colored** lightweight modules – This could be achieved by using a colored PV encapsulant or by including a printed colored foil in our lightweight PV module.

Identify outdoor PV operational conditions
Installation type, temperature exposure

Identify potential PV failure mechanisms
De-adhesion, discoloration, corrosion, fatigue, PID, interconnection breakage

Determine the effect of high temperature
on the observed failure

Indoor testing under accelerated stress tests
Perform accelerated stress tests at different stress levels

Extract the activation energy and
degradation rates of the failure mechanism

Model aging response
Determine a mathematical model that correlates the outdoor failure mechanism with indoor accelerated stress tests

Validation with real-time field data
(use thermal profiles of modules under
different operational conditions, and
different climates)

Long-term performance prediction
Predict module performance as a function of operating temperatures and define lifetime tests for specific installations

Figure 9.1 – Proposed sequence to develop predictive model for long-term performance of lightweight PV modules according to module operating temperature.

- The **reliability of modules with improved aesthetics** – The presence of extra layers (a white film or color layers) on our design introduces a change in the symmetry, which can create a higher coupling of forces and bending moments. Changing the design of our structure, by adding new layers, will require validation under accelerated-aging tests.

- Validation of the **mounting structure** – the *Velcro* mounting structure proposed in this thesis must be tested under accelerated-aging tests to evaluate its stability under high stress. The adhesion strength between the *Velcro* and the module backsheet should be evaluated after each aging test.

- **Fire resistance** – repeat the fire test by including a frame or improve the design by adding flame retardants to the polymers formulations. These components will prevent fire ignition and flame spread and will reduce the amount of smoke released during the fire.

This thesis has addressed the challenges of designing and manufacturing stable glass-free lightweight PV modules, addressing the importance of material and manufacturing selection. Based on the knowledge acquired during this thesis, we predict that forthcoming efforts towards optimization and scalability can be successfully achieved.

A Composite Mechanics Theory

A.1 Micro-mechanics models

A **lamina** is a thin orthotropic layer defined as the smallest element of a macroscopic level. Its properties depend on the combination of two constituents: a reinforcement (fibers) and a matrix (resin) [160], but also depends on fiber arrangement since it can be made of unidirectional, bi-directional or random layers of reinforcement [161].

Rule of Mixtures
For unidirectional composite materials, a reasonable estimate of the composite lamina properties can be obtained using the Rule of Mixtures [159]. Considering the volume fraction of fibers *(V$_{fibers}$)* and matrix *(V$_{matrix}$)*, the respective Young's modulus for fibers *(E$_{fibers}$)* and the matrix *(E$_{matrix}$)* and finally the Poisson's ratio as *(v$_{fibers}$)* and *(v$_{matrix}$)*, the mechanical properties can be calculated as

Longitudinal properties[1]

$$E_L \quad = \quad E_1 = E_{fibers}V_{fibers} + E_{matrix}(1 - V_{fibers}) \tag{A.1a}$$

$$\nu_{LT} \quad = \quad \nu_{12} = \nu_{fibers}V_{fibers} + \nu_{matrix}V_{matrix} \tag{A.1b}$$

Transverse properties[2]

$$E_T \quad = \quad E_2 = \frac{E_{matrix}E_{fibers}}{E_{matrix}V_{fibers} + E_{fibers}V_{matrix})} \tag{A.2a}$$

$$\nu_{TL} \quad = \quad \nu_{21} = \frac{\nu_{12}}{E_1}E_2 \tag{A.2b}$$

---

[1] Properties in the fiber direction of a unidirectional (UD) composite lamina.
[2] Properties in the transverse direction to the fibers.

Shear properties

$$G \quad = \quad \frac{E}{2(1-v)} \tag{A.3a}$$

$$G_{21} \quad = \quad \frac{G_{fibers}G_{matrix}}{G_{matrix}V_{fibers} + G_{fibers}(1-V_{fibers})} \tag{A.3b}$$

with the stress-strain relation of each lamina given be the Hooke's law

$$\begin{pmatrix} \sigma_1 \\ \sigma_2 \\ \tau_{12} \end{pmatrix} = \begin{bmatrix} Q_{11} & Q_{12} & 0 \\ Q_{12} & Q_{22} & 0 \\ 0 & 0 & Q_{66} \end{bmatrix} \begin{pmatrix} \epsilon_1 \\ \epsilon_2 \\ \gamma_{12} \end{pmatrix} \tag{A.4}$$

where σ stands for stress, ϵ stands for strain and Q represents the stiffness matrix given by

$$Q_{11} \quad = \quad \frac{E_1}{1-v_{12}v_{21}}; \tag{A.5a}$$

$$Q_{22} \quad = \quad \frac{E_2}{1-v_{12}v_{21}}; \tag{A.5b}$$

$$Q_{12} \quad = \quad \frac{v_{12}E_2}{1-v_{12}v_{21}} = \frac{v_{21}E_1}{1-v_{12}v_{21}}; \tag{A.5c}$$

$$Q_{66} \quad = \quad G_{12} \tag{A.5d}$$

A.2 Macro-mechanics models

A laminate or skin is composed of several laminae staked in a certain orientation regarding the laminate coordinate system (x-y-z). Thus, in order to describe the laminate behavior, the stiffness matrix of each lamina in its local coordinate system (*1*, *2* and *3*, as defined in section A.1) must be transferred to the laminate coordinate system, as represented in figure A.1. The stiffness of the lamina in the system x-y-z is found by using a transformation matrix which consists in rotating the system *1-2-3* by an angle θ. The transformation matrix is written as

$$\begin{pmatrix} \sigma_1 \\ \sigma_2 \\ \tau_{12} \end{pmatrix} = \begin{bmatrix} c^2 & s^2 & 2sc \\ s^2 & c^2 & -2sc \\ -sc & sc & c^2-s^2 \end{bmatrix} \begin{pmatrix} \sigma_x \\ \sigma_y \\ \tau_{xy} \end{pmatrix} \tag{A.6}$$

from where $c = cos\,\theta$ and $s = sin\,\theta$.

Hence, the stress-strain relation of each lamina in the global coordinate system can be written as $\sigma_{xy} = \overline{Q}_{xy}\,\epsilon_{xy}$, where $\overline{Q}_{xy}$ is the transformed material stiffness matrix given by

$$\overline{Q}_{11} = Q_{11}c^4 + 2(Q_{12} + 2Q_{66})c^2s^2 + Q_{22}s^4 \tag{A.7a}$$

$$\overline{Q}_{21} = \overline{Q}_{12} = (Q_{11} + Q_{22} - 4Q_{66})c^2s^2 + Q_{12}(c^4 + s^4) \tag{A.7b}$$

$$\overline{Q}_{22} = Q_{11}s^4 + 2(Q_{12} + 2Q_{66}c^2s^2 + Q_{22}c^2 \tag{A.7c}$$

$$\overline{Q}_{16} = (Q_{11} - Q_{12} - 2Q_{66})sc^3 + (Q_{12} - Q_{22} + 2Q_{66})s^3c \tag{A.7d}$$

$$\overline{Q}_{26} = (Q_{11} - Q_{12} - 2Q_{66})cs^3 + (Q_{12} - Q_{22} + 2Q_{66})cs^3 \tag{A.7e}$$

$$\overline{Q}_{66} = (Q_{11} - Q_{12} - 2Q_{12} - 2Q_{66})s^2c^2 + Q_{66}(s^4 + c^4) \tag{A.7f}$$

Once the transformed stiffness matrix of each lamina is known, the stiffness matrix of the laminate can be calculated by considering the thickness and position of each lamina in the stack. The laminate extends in the Z-direction from $-h/2$ to $+h/2$. The location of the layer interfaces are denoted by a subscript z: the first layer is bounded by locations z_0 and z_1 and the Nth layer by z_{N-1} and z_N. Knowing that the laminate has now a flexural rigidity, the relation between forces and bending moments to strains and curvatures can be written as

$$\left\{ \begin{array}{c} N \\ M \end{array} \right\} = \left[\begin{array}{cc} A & B \\ B & D \end{array} \right] \left\{ \begin{array}{c} \epsilon^0 \\ k \end{array} \right\} \tag{A.8}$$

where N and M are the external stress and moments resultant and ϵ_0 and k_0 are the mid-plane strains and curvature, respectively. The matrix ABD represents the stiffness matrix of the full
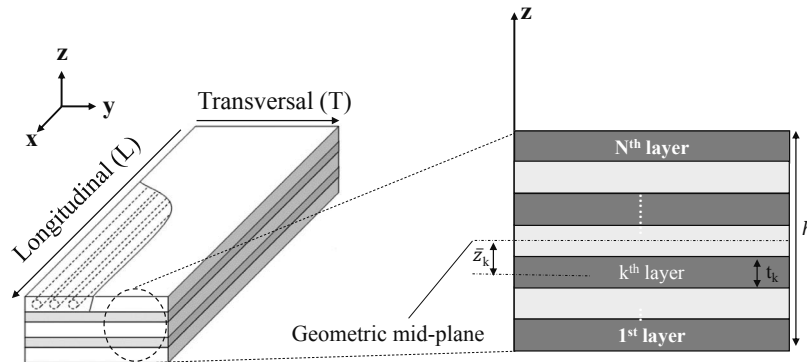
Figure A.1 – Global coordinate system considered within the laminate (left) and scheme of the laminate uses notation (adapted from [160]).

laminate where A is the extensional stiffness matrix, B the bending stretching coupling matrix and D the flexural stiffness matrix. It can be calculated according to

$$A_{ij} \quad = \quad \sum_{k=1}^{N} (\overline{Q}_{ij})_k (z_k - z_{k-1}) \tag{A.9a}$$

$$B_{ij} \quad = \quad \frac{1}{2} \sum_{k=1}^{N} (\overline{Q}_{ij})_k (z_k^2 - z_{k-1}^2) \tag{A.9b}$$

$$D_{ij} \quad = \quad \frac{1}{3} \sum_{k=1}^{N} (\overline{Q}_{ij})_k (z_k^3 - z_{k-1}^3) \tag{A.9c}$$

The laminate properties can be estimated based on the equations presented here, which are used to estimate the engineering constants of the full laminate (E_L, E_T, G_{LT}, ν_L) [160, 231]. Often, the stacking sequence of a laminate is designed to be symmetric to avoid unpredictable warp deflections. For a symmetric laminate, the elements of B matrix are zero and the engineering constants of the whole laminate are found to be

Longitudinal properties:

$$E_L = \frac{A_{11} A_{22} - A_{12}^2}{h A_{22}} \tag{A.10}$$

Tansversal properties:

$$E_T = \frac{A_{11} A_{22} - A_{12}^2}{h A_{11}} \tag{A.11}$$

Shear properties:

$$G_{LT} = \frac{A_{66}}{h} \tag{A.12}$$

Bibliography

[1] International Energy Agency (IEA), "Global Energy & CO_2 Status Report," in *World Energy Outlook*, 2018.

[2] United Nations - Climate changes, "The Paris Agreement." [Online] Available at: https://unfccc.int/, (Date last accessed 2018-05-06).

[3] P. E. Glaser, "Power from the sun: Its future," *Science*, vol. 162, no. 3856, pp. 857–861, 1968.

[4] W. A. Hermann, "Quantifying global exergy resources," *Energy*, vol. 31, no. 12, pp. 1685 – 1702, 2006.

[5] M. Fischer, "International Technology Road map for Photovoltaics (ITRPV) 9th edition - Report relase and key findings," in *Oral Presentation at PV CellTech Conference*, Malaysia, 2018.

[6] C. Molpeceres, D. Canteli, Y. Chen, D. Muñoz, M. Morales, J. J. Garrcia-Ballesteros, and S. Lauzurica, "Laser based processes for product customization in Building Integrated Photovoltaic," in *Proceedings of the CLEO:2016 Conference*, pp. 1–5, Optical Society of America, 2016.

[7] P. R. Defaix, W. G. J. H. M. van Sark, E. Worrell, and E. de Visser, "Technical potential for photovoltaics on buildings in the EU-27," *Solar Energy*, vol. 86, no. 9, pp. 2644–2653, 2012.

[8] G. Verbene, P. Bonomo, F. Frontini, M. Van den Donker, A. Chatzipanagi, K. Sinapis, and W. Folkerts, "BIPV products for facades and roofs: a market analysis," in *Proceedings of the 29th European Photovoltaic Solar Energy Conference and Exhibition*, pp. 3630–3636, Amsterdam, The Netherlands, 2014.

[9] L.-E. Perret-Aebi, "New approaches for BIPV elements: from thin film terra-cotta to crystalline white modules," in *Oral Presentation at 13th National Photovoltaic Congress - Swissolar*, Basel, Switzerland, 2015.

[10] ISSOL, "Photovoltaic solutions for traditional and contenporany architecture - where tradition meets today," 2016. [Online] Available at: http://issol.ch/solarterra/,(Date last accessed 2018-05-08).

Bibliography

[11] C. S. P. López and F. Frontini, "Energy efficiency and renewable solar energy integration in heritage historic buildings," *Energy Procedia*, vol. 48, pp. 1493–1502, 2014.

[12] SolarReviews, "Solar Reviews news," 2018. [Online] Available at: https://www.solarreviews.com/, (Date last accessed 2018-10-06).

[13] N. Jolissaint, R. Hanbali, J.-C. Hadorn, and A. Schüler, "Colored solar façades for buildings," *Energy Procedia*, vol. 122, pp. 175–180, 2017.

[14] T. Söderström, P. Papet, and J. Ufheil, "Smart wire connection technology," in *Proceedings of the 28th European Photovoltaic Solar Energy Conference and Exhibition*, pp. 495–499, Villepinte, France, 2013.

[15] C. Ballif, L.-E. Perret-Aebi, S. Lufkin, and E. Rey, "Integrated thinking for photovoltaics in buildings," *Nature Energy*, vol. 3, no. 6, p. 438, 2018.

[16] T. James, A. Goodrich, M. Woodhouse, R. Margolis, and S. Ong, "Building-Integrated Photovoltaics (BIPV) in the residential sector: an analysis of installed rooftop system prices," tech. rep., NREL, 2011.

[17] V. H. Le Caer and A. Schuler, "Laminated glazing with coloured reflection and high solar transmittance suitable for solar energy systems," Sept. 3 2015. Patent number: US 20150249424A1.

[18] KALEO Project, "Un avenir solaire," 2017. [Online] Available at: http://www.kaleo-solar.ch/fr/, (Date last accessed 2018-10-04).

[19] European Parliament, "Directive 2010/31/EU of the European Parliament and of the Council of 19 May 2010 on the energy performance of buildings," *Official Journal of the European Union*, vol. 18, no. 06, 2010.

[20] A. Chatzipanagi, F. Frontini, and A. Virtuani, "BIPV-temp: A demonstrative Building Integrated Photovoltaic installation," *Applied Energy*, vol. 173, pp. 1–12, 2016.

[21] SwissINSO, "Kromatix – The elegant BIPV solution for coloured solar power facades.," 2017. [Online] Available at: https://www.swissinso.com/, (Date last accessed 2018-10-06).

[22] EN 50583, "Photovoltaic in buildings – Part 1: BIPV modules," *European Comission for Electrotechnical Standardization*, 2016.

[23] P. Heinstein, C. Ballif, and L.-E. Perret-Aebi, "Building integrated photovoltaics (BIPV): review, potentials, barriers and myths," *Green*, vol. 3, no. 2, pp. 125–156, 2013.

[24] H. Nussbaumer, M. Klenk, and N. Keller, "Small unit compond module: A new approach for light weight PV modules," in *Proceedings of the 32nd European Photovoltaic Solar Energy Conference and Exhibition*, Munich, Gerany, 2016.

[25] T. Kajisa, H. Miyauchi, K. Mizuhara, K. Hayashi, T. Tokimitsu, M. Inoue, K. Hara, and A. Masuda, "Novel lighter weight crystalline silicon photovoltaic module using acrylic-film as a cover sheet," *Japanese Journal of Applied Physics*, vol. 53, no. 9, pp. 092302(1–7), 2014.

[26] L'Écho du Solaire, "Le CSEM équipe son site de Neuchâtel d'une façade photo-voltaïque." [Online] Available at: http://www.lechodusolaire.fr/le-csem-equipe-son-site-de-neuchatel-dune-facade-photovoltaique/, (Date last accessed 2018-07-02).

[27] F. Zhang, H. Deng, R. Margolis, and J. Su, "Analysis of distributed-generation photo-voltaic deployment, installation time and cost, market barriers, and policies in china," *Energy Policy*, vol. 81, pp. 43–55, 2015.

[28] R. J. Yang, "Overcoming technical barriers and risks in the application of building integrated photovoltaics (BIPV): hardware and software strategies," *Automation in Construction*, vol. 51, pp. 92–102, 2015.

[29] C. R. Osterwald and T. J. McMahon, "History of accelerated and qualification testing of terrestrial photovoltaic modules: A literature review," *Progress in Photovoltaics: Research and Applications*, vol. 17, no. 1, pp. 11–33, 2009.

[30] P.-J. Ribeyron, "Crystalline silicon solar cells: Better than ever," *Nature Energy*, vol. 2, no. 5, pp. 17067(1–2), 2017.

[31] U. Eitner, *Thermomechanics of photovoltaic modules*. PhD thesis, Universitäts-und Landesbibliothek Sachsen-Anhalt, Diss., 2011.

[32] C. Battaglia, A. Cuevas, and S. De Wolf, "High-efficiency crystalline silicon solar cells: status and perspectives," *Energy & Environmental Science*, vol. 9, no. 5, pp. 1552–1576, 2016.

[33] H. Tian, F. Mancilla-David, K. Ellis, E. Muljadi, and P. Jenkins, "A cell-to-module-to-array detailed model for photovoltaic panels," *Solar energy*, vol. 86, no. 9, pp. 2695–2706, 2012.

[34] R. Miles, "Photovoltaic solar cells: Choice of materials and production methods," *Vacuum*, vol. 80, no. 10, pp. 1090–1097, 2006.

[35] D. King, M. Quintana, J. Kratochvil, D. Ellibee, and B. Hansen, "Photovoltaic module performance and durability following long-term field exposure," *Progress in Photovoltaics: research and applications*, vol. 8, no. 2, pp. 241–256, 2000.

[36] J. Pern, "Module encapsulation materials, processing and testing," in *Oral Presentation at the APP International PV reliability workshop*, Shanghai, China, 2008.

[37] A. Czanderna and F. Pern, "Encapsulation of PV modules using ethylene-vinyl acetate copolymer as a pottant: A critical review," *Solar energy materials and solar cells*, vol. 43, no. 2, pp. 101–181, 1996.

Bibliography

[38] C. Hemmerle, "Solar PV Building Skins: structural requirements and environmental benefits," *Journal of Facade Design and Engineering*, vol. 5, no. 1, pp. 93–105, 2017.

[39] R. Domjan, "PlanetSolar, le premier tour du monde à l'énergie solaire.," 2015. [Online] Available at: http://www.raphaeldomjan.com/projets/planetsolar/, (Date last accessed 2017-01-17).

[40] S. R. Wenham, M. A. Green, M. E. Watt, R. Corkish, and A. Sproul, *Applied photovoltaics*. Routledge, 2013.

[41] B. Fufa, C. Zhao-Bo, and M. Wensheng, "Modeling and simulation of satellite solar panel deployment and locking," *Information Technology Journal*, vol. 9, no. 3, pp. 600–604, 2010.

[42] D. Sigler, "Solarstratos construction to begin in January," 2014. [Online] Available at: http://sustainableskies.org/solarstratos-construction-begin-january/, (Date last accessed 2016-02-01).

[43] H. Ross, "Fly around the world with a solar powered airplane," in *Prooceedings of the 26th Congress of International Council of the Aeronautical Sciences (ICAS)*, vol. 8825, pp. 8954(1–11), American Institute of Aeronautics and Astronautics, 2008.

[44] N. Baldock and M. Mokhtarzadeh-Dehghan, "A study of solar-powered, high-altitude unmanned aerial vehicles," *Aircraft Engineering and Aerospace Technology*, vol. 78, no. 3, pp. 187–193, 2006.

[45] H. Funke, "Development of the ultralight aircraft silence: aeronautics," *JEC composites*, no. 10, pp. 52–54, 2004.

[46] O. Rozant, P.-E. Bourban, and J.-A. Manson, "Manufacturing of three dimensional sandwich parts by direct thermoforming," *Elsevier*, vol. 32, no. 11, pp. 1593–1601, 2001.

[47] A. Baker, S. Dutton, and D. Kelly, *Composite Materials for Aircraft Structures*. American Institute of aeronautics and astronautics (AIAA), 2004.

[48] J. M. Davies, *Lightweight sandwich construction*. John Wiley & Sons, 2008.

[49] M. S. A. Balla-Goddard, A. F. Denny, and P. G. Harrison, "Building panel and buildings made therefrom," Apr. 28 1998. Patent number: US 5743056.

[50] D. Thomas, S. C. Mantell, J. H. Davidson, L. F. Goldberg, and J. Carmody, "Analysis of sandwich panels for an energy efficient and self-supporting residential roof," *Journal of solar energy engineering*, vol. 128, no. 3, pp. 338–348, 2006.

[51] Light Joule module datasheet from AGC Glass, "Ultra-lightweight photovoltaic module." [Online] Available at: http://www.lightjoule.com/english/leoflex.html, (Date last accessed 2017-06-20).

138

[52] L. Yujie, W. Shiyuan, and Z. Yunyun, "Thechnology capable of taking glass fiber honeycomb material as battery sheet packaging bottom lining substrate and photovoltaic assembly," Mar. 25 2011. Patent number: CN 102218853A.

[53] L. Yujie, W. Shiyuan, and Z. Yunyun, "Photovoltaic component adopting glass fiber honeycomb material as cell packaging bottom-lining based board," Mar. 25 2011. Patent number: CN 202088535U.

[54] Z. Fujia, L. Xinhua, H. Yuewen, T. Rong, and Z. Zhong, "Substrate of flexible solar photovoltaic assembly," Sept. 23 2014. Patent number: CN 104183662A.

[55] Y. Fei, C. Xiaoqing, and Z. Xue, "Novel photovoltaic component with substrate of honeycomb," Sept. 6 2013. Patent number: CN 202839683U.

[56] H. Ehbing, G. Stollwerck, D. Wegener, J. Krause, E. Springer, H. Schmidt, and F. Schauseil, "Light, rigid, self-supporting solar module and method for the production thereof," June 12 2009. Patent number: WO 2009149850A2.

[57] G. Oreski, A. Halm, V. Schenk, W. Krumlacher, and H. Nussbaumer, "Investigation of effects due to encapsulation thickness reduction in lightweight modules," in *Proceedings of 33rd European Photovoltaic Solar Energy Conference and Exhibition*, Amsterdam, The Netherlands, 2017.

[58] J. Gaume, P. Lefiliantre, G. Goaer, N. L. Quang, and S. Williatte, "Lightweight photovoltaic module including a front layer made from glass or polymer and a rear layer comprising raised portions," Mar. 26 2017. Patent number: WO 2017085021A1.

[59] A. Boulanger, J. Gaume, F. Quesnel, P. Ruols, and F. Rouby, "Operasol: A light photovoltaic panel with integrated connectors," in *Oral Presentation at 33rd European Photovoltaic Solar Energy Conference and Exhibition*, Amsterdam, The Netherlands, 2017.

[60] J. Gaume, F. Quesnel, S. Guillerez, N. Le Quang, S. Williatte, and G. G., "Solight®: A new lightweight PV module complying IEC standards," in *Poster Presentation at 33rd European Photovoltaic Solar Energy Conference and Exhibition*, Amsterdam, The Netherlands, 2017.

[61] S. Schulze, M. Pander, S. Mueller, C. Ehrich, and M. Ebert, "Influence of vacuum lamination process on laminate properties – simulation and test results," in *Proceedings of the 24th European Photovoltaic Solar Energy Conference and Exhibition*, pp. 21–25, Hamburg, Germany, 2009.

[62] R. B. Sraisth, "Achieving faster lamination process for crystalline photovoltaic modules by using latest lamination technologies," in *Proceedings of the 33rd European Photovoltaic Solar Energy Conference and Exhibition*, pp. 992–997, Amsterdam, The Netherlands, 2017.

Bibliography

[63] Z. Campeau, M. Anderson, E. Hasselbrink, D. Kavulak, Y.-C. Shen, R. Lacerda, A. Terao, S. Caldwel, Z. Defreitas, L. Leonard, M. Mikofski, D. DeGraaff, and A. Budiman, "Module degradation rate," tech. rep., Sunpower, 2013.

[64] M. Schweiger, J. Bonilla, W. Herrmann, A. Gerber, and U. Rau, "Performance stability of photovoltaic modules in different climates," *Progress in Photovoltaics: research and applications*, vol. 25, no. 12, pp. 968–981, 2017.

[65] M. Schweiger and W. Herrmann, "Comparison of energy yield data of fifteen PV module technologies operating in four different climates," in *Proceedings of the 42nd IEEE Photovoltaic Specialists Conference*, pp. 1–6, New Orleans, USA, 2015.

[66] IEC 61215, "Terrestrial photovoltaic (PV) modules - Design qualification and type approval - Part 2: Test procedures," *International Electrotechnical Commission*, 2016.

[67] IEC 61730, "Photovoltaic (PV) module safety qualification - Part 1: Requirements for construction," *International Electrotechnical Commission*, 2016.

[68] D. C. Jordan, T. J. Silverman, J. H. Wohlgemuth, S. R. Kurtz, and K. T. VanSant, "Photovoltaic failure and degradation modes," *Progress in Photovoltaics: Research and Applications*, vol. 25, no. 4, pp. 318–326, 2017.

[69] H. Häberlin, L. Borgna, D. Gfeller, and P. Schärf, "BIPV: Aesthetics alone are not sufficient – Long-term energy yield and safety are equally important," in *Proceedings of the 26th European Photovoltaic Solar Energy Conference and Exhibition*, Hamburg, Germany, 2011.

[70] N. Aste, C. Del Pero, and F. Leonforte, "The first Italian BIPV project: case study and long-term performance analysis," *Solar Energy*, vol. 134, pp. 340–352, 2016.

[71] T. Nordmann and L. Clavadetscher, "Understanding temperature effects on PV system performance," in *Proceedings of the 3rd World Conference on Photovoltaic Energy Conversion*, pp. 2243–2246, Osaka, Japan, 2003.

[72] T. Sample and A. Virtuani, "Modification to the standard reference enviroment (SER) for nominal operating cell temperature (NOCT) to account for building integration," in *Proceedings of the 24th European Photovoltaic Solar Energy Conference and Exhibition*, Hamburg, Germany, 2009.

[73] G. Gan, "Effect of air gap on the performance of building-integrated photovoltaics," *Energy*, vol. 34, no. 7, pp. 913–921, 2009.

[74] N. Martín-Chivelet, J. Gutiérrez, M. Alonso-Abella, F. Chenlo, and J. Cuenca, "Building retrofit with photovoltaics: Construction and performance of a BIPV ventilated façade," *Energies*, vol. 11, no. 7, p. 1719, 2018.

[75] IEC 60050, "International electrotechnical vocabulary: Dependability and quality of servicedependability and quality of service (ch: 191)," *International Electrotechnical Commission*, 1990.

[76] J. H. Wohlgemuth, D. W. Cunningham, P. Monus, J. Miller, and A. Nguyen, "Long term reliability of photovoltaic modules," in *Proceedings of the 4th World Conference on Photovoltaic Energy Conversion*, vol. 2, pp. 2050–2053, Hawaii, USA, 2006.

[77] D. C. Jordan, J. H. Wohlgemuth, and S. R. Kurtz, "Technology and climate trends in PV module degradation," tech. rep., NREL, 2012.

[78] W. Herrmann, N. Bogdanski, F. Reil, M. Köhl, K.-A. Weiss, M. Assmus, and M. Heck, "PV module degradation caused by thermomechanical stress: real impacts of outdoor weathering versus accelerated testing in the laboratory," in *Reliability of Photovoltaic Cells, Modules, Components, and Systems III*, vol. 7773, p. 77730I, International Society for Optics and Photonics, 2010.

[79] W. Herrmann and N. Bogdanski, "Outdoor weathering of PV modules – effects of various climates and comparison with accelerated laboratory testing," in *Proceedings of the 37th IEEE Photovoltaic Specialists Conference*, pp. 2305–2311, Washinton, USA, 2011.

[80] IEC 62804, "Photovoltaic (PV) modules – Test methods for the detection of potential-induced degradation – Part 1: Crystalline silicon," *International Electrotechnical Commission*, 2015.

[81] J. H. Wohlgemuth and S. Kurtz, "Using accelerated testing to predict module reliability," in *Proceeding of the 37th IEEE Photovoltaic Specialists Conference*, pp. 3601–3605, Washington, USA, 2011.

[82] E. L. Meyer and E. E. Van Dyk, "Assessing the reliability and degradation of photovoltaic module performance parameters," *IEEE Transactions on reliability*, vol. 53, no. 1, pp. 83–92, 2004.

[83] V. Sharma and S. Chandel, "Performance and degradation analysis for long term reliability of solar photovoltaic systems: a review," *Renewable and Sustainable Energy Reviews*, vol. 27, pp. 753–767, 2013.

[84] P. Hacke, K. Terwilliger, R. Smith, S. Glick, J. Pankow, M. Kempe, S. K. I. Bennett, and M. Kloos, "System voltage potential-induced degradation mechanisms in PV modules and methods for test," in *Proceedings of the 37th IEEE Photovoltaic Specialists Conference*, pp. 814–820, Washington, USA, 2011.

[85] F. Pern, "Ethylene-vinyl acetate (EVA) encapsulants for photovoltaic modules: Degradation and discoloration mechanisms and formulation modifications for improved photostability," *Macromolecular Materials and Engineering*, vol. 252, no. 1, pp. 195–216, 1997.

Bibliography

[86] E. Annigoni, "Reliability of photovoltaic modules: from indoor testing to long-term performance prediction," *PhD thesis, Ecole Polythectine Federal de lausanne (EPFL)*, 2018.

[87] A. C. Martins, V. Chapuis, F. Sculati-Meillaud, A. Virtuani, and C. Ballif, "Light and durable: Composite structures for building-integrated photovoltaic modules," *Progress in Photovoltaics: Research and Applications*, vol. 26, no. 9, pp. 718–729, 2018.

[88] A. C. Martins, V. Chapuis, A. Virtuani, H.-Y. Li, L.-E. Perret-Aebi, and C. Ballif, "Thermo-mechanical stability of lightweight glass-free photovoltaic modules based on a composite substrate," *Solar Energy Materials and Solar Cells*, vol. 187, pp. 82–90, 2018.

[89] A. C. Martins, V. Chapuis, A. Virtuani, and C. Ballif, "Robust glass-free lightweight photovoltaic modules with improved resistance to mechanical loads and impact," *IEEE Journal of Photovoltaic*, accepted, 2018.

[90] Plascore, "Engineered honeycomb solutions and services – honeycomb panels," tech. rep., Plascore, 2018.

[91] C. Hirschl, M. Biebl–Rydlo, M. DeBiasio, W. Mühleisen, L. Neumaier, W. Scherf, G. Oreski, G. Eder, B. Chernev, and W. Schwab, "Determining the degree of crosslinking of ethylene-vinyl acetate photovoltaic module encapsulants – A comparative study," *Solar Energy Materials and Solar Cells*, vol. 116, pp. 203–218, 2013.

[92] W. Stark and M. Jaunich, "Investigation of ethylene-vinyl acetate copolymer (EVA) by thermal analysis DSC and DMA," *Polymer Testing*, vol. 30, no. 2, pp. 236 – 242, 2011.

[93] R. Popli and L. Mandelkern, "The transition in ethylene copolymers: the β-transition," *Polymer bulletin*, vol. 9, no. 6-7, pp. 260–267, 1983.

[94] M. Brogly, M. Nardin, and J. Schultz, "Effect of vinylacetate content on crystallinity and second-order transitions in ethylene – vinylacetate copolymers," *Journal of Applied Polymer Science*, vol. 64, no. 10, pp. 1903–1912, 1997.

[95] M. D. Kempe, "Rheological and mechanical considerations for photovoltaic encapsulants," in *Proceedings of the DOE Solar Energy Technologies workshop*, Colorado, USA, 2005.

[96] P. R. Dluzneski, "Peroxide vulcanization of elastomers," *Rubber chemistry and technology*, vol. 74, no. 3, pp. 451–492, 2001.

[97] G. Oreski, A. Rauschenbach, C. Hirschl, M. Kraft, G. Eder, and G. Pinter, "Crosslinking and post-crosslinking of ethylene vinyl acetate in photovoltaic modules," *Journal of Applied Polymer Science*, vol. 134, no. 23, 2017.

[98] J. Aho, "Rheological characterization of polymer melts in shear and extension: measurement reliability and data for practical processing," *PhD thesis, Tampere University of Technology*, 2011.

[99]   A. F. Bower, *Applied mechanics of solids*. CRC press, 2009.

[100] W. Sun, A. P. Vassilopoulos, and T. Keller, "Effect of thermal lag on glass transition temperature of polymers measured by DMA," *International Journal of Adhesion and Adhesives*, vol. 52, pp. 31–39, 2014.

[101] M. Savvilotidou, A. Vassilopoulos, M. Frigione, and T. Keller, "Effects of aging in dry environment on physical and mechanical properties of a cold-curing structural epoxy adhesive for bridge construction," *Construction and Building Materials*, vol. 140, pp. 552–561, 2017.

[102] CUR commission C124, "Recommendation 96: Fibre-reinforced polymers in civil load-bearing structures," *CUR Gouda*, 2003.

[103] I. Georgiou, H. Hadavinia, A. Ivankovic, A. Kinloch, V. Tropsa, and J. Williams, "Cohesive zone models and the plastically deforming peel test," *The Journal of adhesion*, vol. 79, no. 3, pp. 239–265, 2003.

[104] G. Jorgensen, K. Terwilliger, J. DelCueto, S. Glick, M. Kempe, J. Pankow, F. Pern, and T. McMahon, "Moisture transport, adhesion, and corrosion protection of PV module packaging materials," *Solar Energy Materials and Solar Cells*, vol. 90, no. 16, pp. 2739–2775, 2006.

[105] F. D. Novoa, D. C. Miller, and R. H. Dauskardt, "Environmental mechanisms of debonding in photovoltaic backsheets," *Solar Energy Materials and Solar Cells*, vol. 120, pp. 87–93, 2014.

[106] I. Kim, Y.-H. Min, C.-H. Kim, E.-H. Lee, and D.-S. Kim, "Reliability analysis of photovoltaic modules by contact states between interconnector ribbon and AG electrode," in *Proceedings of the 33rd European Photovoltaic Solar Energy Conference and Exhibition*, pp. 1751–1753, Amsterdam, The Netherlands, 2017.

[107] S. Hoffmann, T. Geipel, M. Meinert, and A. Kraft, "Analysis of peel and shear forces after temperature cycle tests for electrical conductive adhesives," in *Proceedings of the 33rd European Photovoltaic Solar Energy Conference and Exhibition*, pp. 183–186, Amsterdam, The Netherlands, 2017.

[108] D. R. Moore, "An introduction to the special issue on peel testing," *International Journal of Adhesion and Adhesives*, vol. 28, no. 4, pp. 153–157, 2008.

[109] E. Hart, "Theory of the tensile test," *Acta metallurgica*, vol. 15, no. 2, pp. 351–355, 1967.

[110] ASTM Standard D3039, "Tensile properties of polymer matrix composite materials," in *Annual Book of ASTM Standards*, West Conshohocken, PA, 2014.

[111] ASTM Standard C393-00, "Standard test methods for flexural properties of sandwich constructions," in *Annual Book of ASTM Standards*, West Conshohocken, PA, 2000.

[112] F. Arias, P. J. Kenis, B. Xu, T. Deng, O. J. Schueller, G. M. Whitesides, Y. Sugimura, and A. G. Evans, "Fabrication and characterization of microscale sandwich beams," *Journal of Materials Research*, vol. 16, no. 2, pp. 597–605, 2001.

[113] ASTM Standard C313-10, "Practice for calculating yellowness and whiteness indices from instrumentally measured color coordinates," in *Annual Book of ASTM Standards*, West Conshohocken, PA, 2015.

[114] D. C. Miller, J. Bengoechea, J. G. Bokria, M. Köhl, N. E. Powell, M. E. Smith, M. D. White, H. R. Wilson, and J. H. Wohlgemuth, "Examination of an optical transmittance test for photovoltaic encapsulation materials," in *Proceedings of the SPIE Optics & Photonics Conference*, vol. 8825, pp. 882509(1–13), International Society for Optics and Photonics, California, USA, 2013.

[115] P. Blum, *Physical properties handbook: a guide to the shipboard measurement of physical properties of deep-sea cores.* Texas A& M University, 1997.

[116] C. Peike, P. Hülsmann, M. Blüml, P. Schmid, K.-A. Weiß, and M. Köhl, "Impact of permeation properties and backsheet-encapsulant interactions on the reliability of PV modules," *ISRN Renewable Energy*, vol. 2012, pp. 1–5, 2012.

[117] G. Lamour, A. Hamraoui, A. Buvailo, Y. Xing, S. Keuleyan, V. Prakash, A. Eftekhari-Bafrooei, and E. Borguet, "Contact angle measurements using a simplified experimental setup," *Journal of chemical education*, vol. 87, no. 12, pp. 1403–1407, 2010.

[118] M. Köntges, S. Kurtz, C. Packard, U. Jahn, K. Berger, K. Kato, T. Friesen, H. Liu, and M. Van Iseghem, "Review of failures of photovoltaic modules," *IEA PVPS Task*, vol. 13, 2014.

[119] IEC 60904-3:2016, "Measurement principles for terrestrial photovoltaic (PV) solar devices with reference spectral irradiance data," *International Electrotechnical Commission*, 2016.

[120] S. Hoffmann and M. Koehl, "Effect of humidity and temperature on the potential-induced degradation," *Progress in Photovoltaics: Research and Applications*, vol. 22, no. 2, pp. 173–179, 2014.

[121] DAS Energy GmbH, "The flexible modules." [Online] Available at: http://www.das-energy.com/de/, (Date last accessed 2018-04-11).

[122] Flisom, "Ultra-thin, lightweight and flexible solar panels – building and mobility." [Online] Available at: https://flisom.com/, (Date last accessed 2018-04-11).

[123] Sunpower, "Flexible lightweight panels," 2018. [Online] Available at: https://us.sunpower.com/, (Date last accessed 2018-04-11).

[124] X. Xu, K. Lord, G. Pietka, F. Liu, K. Beernink, B. Yan, C. Worrel, G. DeMaggio, A. Banerjee, J. Yang, *et al.*, "High efficiency ultra lightweight a-si: H/a-sige: H/a-sige: H triple-junction solar cells on polymer substrate using roll-to-roll technology," in *Proceedings of the 33rd IEEE Photovoltaic Specialists Conference*, pp. 1–6, California, USA, 2008.

[125] A. Takano and T. Kamoshita, "Light-weight and large-area solar cell production technology," *Japanese journal of applied physics*, vol. 43, no. 12, pp. 7976–7983, 2004.

[126] W. Soppe, B. Van Aken, M. Dörenkämper, C. Devilee, M. Heijna, and J. Löffler, "Roll to roll fabrication process of thin-film silicon solar cells on steel foil," *ECN Solar Energy*, vol. 4, 2004.

[127] J. Rath, M. Brinza, Y. Liu, A. Borreman, and R. Schropp, "Fabrication of thin film silicon solar cells on plastic substrate by very high frequency PECVD," *Solar Energy Materials and Solar Cells*, vol. 94, no. 9, pp. 1534–1541, 2010.

[128] M. Knausz, G. Oreski, M. Schmidt, P. Guttmann, K. Berger, Y. Voronko, G. Eder, T. Koch, and G. Pinter, "Thermal expansion behavior of solar cell encapsulation materials," *Polymer Testing*, vol. 44, pp. 160–167, 2015.

[129] Plexiglas datasheet from Evonik Industries AG, "Plexiglas Solar 0Z023," 2011. [Online] Available at: http://corporate.evonik.com/en, (Date last accessed 2018-04-11).

[130] R. M. Wang, S. R. Zheng, and Y. P. Zheng, *Polymer Matrix Composites and Technology (Chapter 11)*. Woodhead Publishing (Science Press), Cambridge, UK, 2011.

[131] O. Ogbomo, E. Amalu, N. Ekere, and P. Olagbegi, "Effect of coefficient of thermal expansion (cte) mismatch of solder joint materials in photovoltaic (PV) modules operating in elevated temperature climate on the joint's damage," *Procedia Manufacturing*, vol. 11, pp. 1145–1152, 2017.

[132] H.-Y. Li, Y. Luo, C. Ballif, and L.-E. Perret-Aebi, "Effect of cooling press on the optical transmission through photovoltaic encapsulants," *Polymer-Plastics Technology and Engineering*, vol. 54, no. 4, pp. 416–424, 2015.

[133] G. Meszlényi and G. Körtvélyessy, "Direct determination of vinyl acetate content of ethylene-vinyl acetate copolymers in thick films by infrared spectroscopy," *Polymer testing*, vol. 18, no. 7, pp. 551–557, 1999.

[134] E. Wang, H. E. Yang, J. Yen, S. Chi, and C. Wang, "Failure modes evaluation of PV module via materials degradation approach," *Energy Procedia*, vol. 33, pp. 256–264, 2013.

[135] M. C. Costache, D. D. Jiang, and C. A. Wilkie, "Thermal degradation of ethylene–vinyl acetate coplymer nanocomposites," *Polymer*, vol. 46, no. 18, pp. 6947–6958, 2005.

[136] J. L. White and D. D. Choi, "Polyolefins: Processing," *Structure Development and properties*, vol. 1, p. 18, 2005.

Bibliography

[137] M. Djebara, J. Stoquert, M. Abdesselam, D. Muller, and A. Chami, "FTIR analysis of polyethylene terephthalate irradiated by MeV He+," *Nuclear Instruments and Methods in Physics Research Section B: Beam Interactions with Materials and Atoms*, vol. 274, pp. 70–77, 2012.

[138] K. C. Cole, A. Ajji, and E. Pellerin, "New insights into the development of ordered structure in poly(ethylene terephthalate): Results from external reflection infrared spectroscopy," *Macromolecules*, vol. 35, no. 3, pp. 770–784, 2002.

[139] S. Krimm, "Infrared spectra of high polymers," in *Fortschritte der Hochpolymeren-Forschung*, pp. 51–172, Springer, 1960.

[140] Z. Zhu and M. J. Kelley, "IR spectroscopic investigation of the effect of deep UV irradiation on PET films," *Polymer*, vol. 46, no. 20, pp. 8883–8891, 2005.

[141] G. Duan, C. Zhang, A. Li, X. Yang, L. Lu, and X. Wang, "Preparation and characterization of mesoporous zirconia made by using a poly(methyl methacrylate) template," *Nanoscale research letters*, vol. 3, no. 3, p. 118, 2008.

[142] N. Kim, H. Kang, K.-J. Hwang, C. Han, W. S. Hong, D. Kim, E. Lyu, and H. Kim, "Study on the degradation of different types of backsheets used in PV module under accelerated conditions," *Solar Energy Materials and Solar Cells*, vol. 120, pp. 543–548, 2014.

[143] L. Lundquist, Y. Leterrier, P. Sunderland, and J.-A. E. Månson, *Life cycle engineering of plastics: technology, economy and environment.* Elsevier, 2001.

[144] G. Oreski, "Accelerated indoor durability testing of polymeric photovoltaic encapsulation materials," in *Reliability of Photovoltaic Cells, Modules, Components, and Systems III*, vol. 7773, p. 77730D, International Society for Optics and Photonics, 2010.

[145] W. Fairbairn, *An Account of the Construction of the Britannia and Conway Tubular Bridges*, vol. 59. John Weale, 1849.

[146] D. Zenkert, *An introduction to sandwich construction.* Engineering materials advisory services, 1995.

[147] T. Keller, "Recent all-composite and hybrid fibre-reinforced polymer bridges and buildings," *Progress in Structural Engineering and Materials*, vol. 3, no. 2, pp. 132–140, 2001.

[148] T. Keller, "New bridges and buildings constructed from translucent GFRP sandwich panels and glued GFRP elements," in *Proceedings of the 3rd International Conference on Advanced Composite Materials in Bridges and Structures*, pp. 785–732, Ottawa, Canada, 2002.

[149] D. V. Beaver, "Sandwich top construction for office furniture," June 16 1970. Patent number: US 3676279A.

146

[150] J. Rion, "Ultra-light photovoltaic composite sandwich structures," *PhD thesis, Ecole Polythectine Federal de lausanne (EPFL)*, 2008.

[151] Hexcel Composite, "Technical manual: honeycomb sandwich design technology," 2004. [Online] Available at: http//:www.hexcelcomposite.com, (Date last accessed 2018-03-20).

[152] J. Kindinger, "Lightweight structural cores," *ASM Handbook*, vol. 21, pp. 180–183, 2001.

[153] G. A. Howard, *Analysis and design of structural sandwich panels*. Oxford: Pergamon Press, 1969.

[154] G. Eckold, *Design and manufacture of composite structures*. Elsevier, 1994.

[155] D. Zenkert, "Strength of sandwich beams with interface debondings," *Composite Structures*, vol. 17, no. 4, pp. 331–350, 1991.

[156] M. Banea and L. F. da Silva, "Adhesively bonded joints in composite materials: an overview," *Journal of Materials: Design and Applications*, vol. 223, no. 1, pp. 1–18, 2009.

[157] W. S. Burton and A. Noor, "Structural analysis of the adhesive bond in a honeycomb core sandwich panel," *Finite Elements in analysis and design*, vol. 26, no. 3, pp. 213–227, 1997.

[158] L. P. Kollár and G. S. Springer, *Mechanics of composite structures*. Cambridge university press, 2003.

[159] M. Sudheer, K. Pradyoth, and S. Somayaji, "Analytical and numerical validation of epoxy/glass structural composites for elastic models," *American Journal of Materials Science*, vol. 5, no. 3C, pp. 162–168, 2015.

[160] P.-E. Bourban, *Matériaux composites à matrice organique: constituants, procédés, propriétés*, vol. 15. PPUR presses polytechniques, 2004.

[161] R. M. Jones, *Mechanics of composite materials*, vol. 193. Scripta Book Company Washington, DC, 1975.

[162] A. K. Kaw, *Mechanics of composite materials*. CRC press, 2005.

[163] I. Daniel, "Failure of composite materials," *Strain journal*, vol. 43, no. 1, pp. 4–12, 2007.

[164] I. Daniel, E. Gdoutos, K.-A. Wang, and J. Abot, "Failure modes of composite sandwich beams," *International journal of damage mechanics*, vol. 11, no. 4, pp. 309–334, 2002.

[165] C. Kassapoglou, S. C. Fantle, and J. C. Chou, "Wrinkling of composite sandwich structures under compression," *Journal of Composites, Technology and Research*, vol. 17, no. 4, pp. 308–316, 1995.

Bibliography

[166] A. S. Benson and J. Mayers, "General instability and face wrinkling of sandwich plates-unified theory and applications.," *AIAA journal*, vol. 5, no. 4, pp. 729–739, 1967.

[167] W. K. Vonach and F. G. Rammerstorfer, "The effects of in-plane core stiffness on the wrinkling behavior of thick sandwiches," *Acta mechanica*, vol. 141, no. 1-2, pp. 1–10, 2000.

[168] A. Petras and M. Sutcliffe, "Failure mode maps for honeycomb sandwich panels," *Composite Structures*, vol. 44, no. 4, pp. 237–252, 1999.

[169] C. B. Norris, *Short-column compressive strength of sandwich constructions as affected by size of cells of honeycomb core materials*, vol. 26. US Dept. of Agriculture, Forest Service, Forest Products Laboratory, 1964.

[170] O. T. Thomsen and W. M. Banks, "An improved model for the prediction of intra-cell buckling in CFRP sandwich panels under in-plane compressive loading," *Composite structures*, vol. 65, no. 3-4, pp. 259–268, 2004.

[171] A. Petras and M. Sutcliffe, "Indentation failure analysis of sandwich beams," *Composite Structures*, vol. 50, no. 3, pp. 311–318, 2000.

[172] P. Carey, R. Aceves, N. Colella, K. Williams, R. Sinton, and G. Glenn, "A solar module fabrication process for hale solar electric uavs," in *Proceedings of the 1st World Conference on Photovoltaic Energy Conversion*, vol. 2, pp. 1963–1969, Hawaii, USA, 1994.

[173] T. Keller, A. P. Vassilopoulos, and B. D. Manshadi, "Thermomechanical behavior of multifunctional GFRP sandwich structures with encapsulated photovoltaic cells," *Journal of composites for construction*, vol. 14, no. 4, pp. 470–478, 2010.

[174] T. Keller, C. Haas, and T. Vallée, "Structural concept, design, and experimental verification of a glass fiber-reinforced polymer sandwich roof structure," *Journal of composites for construction*, vol. 12, no. 4, pp. 454–468, 2008.

[175] L. Zhang, L. J. Yao, J. S. Wang, B. Li, and X. Y. Tong, "Ultra-light photovoltaic embedded structures for solar-powered aircrafts," in *Advanced Materials Research*, vol. 311, pp. 15–19, Trans Tech Publ, 2011.

[176] A. P. Mouritz, E. Gellert, P. Burchill, and K. Challis, "Review of advanced composite structures for naval ships and submarines," *Composite structures*, vol. 53, no. 1, pp. 21–42, 2001.

[177] C. E. Bakis, L. C. Bank, V. Brown, E. Cosenza, J. Davalos, J. Lesko, A. Machida, S. Rizkalla, and T. Triantafillou, "Fiber-reinforced polymer composites for construction – state-of-the-art review," *Journal of composites for construction*, vol. 6, no. 2, pp. 73–87, 2002.

[178] R. Okada and M. Kortschot, "The role of the resin fillet in the delamination of honeycomb sandwich structures," *Composites Science and Technology*, vol. 62, no. 14, pp. 1811–1819, 2002.

[179] S. Grove, E. Popham, and M. Miles, "An investigation of the skin/core bond in honeycomb sandwich structures using statistical experimentation techniques," *Composites Part A: Applied Science and Manufacturing*, vol. 37, no. 5, pp. 804–812, 2006.

[180] B. S. Hayes, J. C. Seferis, and R. R. Edwards, "Self-adhesive honeycomb prepreg systems for secondary structural applications," *Polymer Composites*, vol. 19, no. 1, pp. 54–64, 1998.

[181] J. Rion, Y. Leterrier, and J.-A. E. Månson, "Prediction of the adhesive fillet size for skin to honeycomb core bonding in ultra-light sandwich structures," *Composites Part A: Applied Science and Manufacturing*, vol. 39, no. 9, pp. 1547–1555, 2008.

[182] A. Virtuani and D. Strepparava, "Modelling the performance of amorphous and crystalline silicon in different typologies of building-integrated photovoltaic (BIPV) conditions," *Solar Energy*, vol. 146, pp. 113–118, 2017.

[183] L. Fanni, A. Virtuani, and D. Chianese, "A detailed analysis of gains and losses of a fully-integrated flat roof amorphous silicon photovoltaic plant," *Solar Energy*, vol. 85, no. 9, pp. 2360 – 2373, 2011.

[184] J. Kurnik, M. Jankovec, K. Brecl, and M. Topic, "Outdoor testing of PV module temperature and performance under different mounting and operational conditions," *Solar Energy Materials and Solar Cells*, vol. 95, pp. 373–376, Jan. 2011.

[185] S. Kurtz, K. Whitfield, G. TamizhMani, M. Koehl, D. Miller, J. Joyce, J. Wohlgemuth, N. Bosco, M. Kempe, and T. Zgonena, "Evaluation of high-temperature exposure of photovoltaic modules," *Progress in Photovoltaics: Research and Applications*, vol. 19, no. 8, pp. 954–965, 2011.

[186] ETAG002 – European Organization for Thecnical Approvals, "Guidelines for european technical approval for structural sealant glazing system," *European Organization for Thecnical Approvals*, 2005.

[187] D. C. Jordan, T. J. Silverman, B. Sekulic, and S. R. Kurtz, "PV degradation curves: nonlinearities and failure modes," *Progress in Photovoltaics: Research and Applications*, vol. 25, no. 7, pp. 583–591, 2017.

[188] J. Berghold, S. Koch, A. Böttcher, A. Ukar, M. Leers, and P. Grunow, "Potential-induced degradation (PID) and its correlation with experience in the field," *Photovoltaics International*, vol. 19, pp. 85–92, 2013.

[189] J. Bauer, V. Naumann, S. Großer, C. Hagendorf, M. Schütze, and O. Breitenstein, "On the mechanism of potential-induced degradation in crystalline silicon solar cells," *Physica status solidi (RRL) – Rapid Research Letters*, vol. 6, no. 8, pp. 331–333, 2012.

[190] S. Pingel, O. Frank, M. Winkler, S. Daryan, T. Geipel, H. Hoehne, and J. Berghold, "Potential induced degradation of solar cells and panels," in *Proceedings of the 35th IEEE Photovoltaic Specialists Conference*, Hawaii, USA, 2010.

Bibliography

[191] P. Hacke, M. Kempe, K. Terwilliger, S. Glick, N. Call, S. Johnston, and S. Kurtz, "Characterization of multicrystalline silicon modules with system bias voltage applied in damp heat," tech. rep., NREL, 2011.

[192] J. C. Gerdeen, R. A. Rorrer, and H. W. Lord, *Engineering design with polymers and composites*, vol. 30. CRC Press, 2011.

[193] M. P. Sepe, *Dynamic Mechanical Analysis for Plastics Engineering*. William Andrew, 1998.

[194] A. Eisenberg and M. Rinaudo, "Polyelectrolytes and ionomers," *Polymer bulletin*, vol. 24, no. 6, pp. 671–671, 1990.

[195] R. J. Varley and S. van der Zwaag, "Towards an understanding of thermally activated self-healing of an ionomer system during ballistic penetration," *Acta Materialia*, vol. 56, no. 19, pp. 5737–5750, 2008.

[196] M. Santarsiero, C. Louter, and A. Nussbaumer, "The mechanical behaviour of SentryGlas ionomer and TSSA silicon bulk materials at different temperatures and strain rates under uniaxial tensile stress state," *Glass Structures & Engineering*, vol. 1, no. 2, pp. 395–415, 2016.

[197] K. R. McIntosh, N. E. Powell, A. W. Norris, J. N. Cotsell, and B. M. Ketola, "The effect of damp-heat and UV aging tests on the optical properties of silicone and EVA encapsulants," *Progress in Photovoltaics: Research and Applications*, vol. 19, no. 3, pp. 294–300, 2011.

[198] G. Oreski, A. Mihaljevic, Y. Voronko, and G. C. Eder, "Acetic acid permeation through photovoltaic backsheets: Influence of the composition on the permeation rate," *Polymer Testing*, vol. 60, pp. 374–380, 2017.

[199] M. Paggi, I. Berardone, A. Infuso, and M. Corrado, "Fatigue degradation and electric recovery in silicon solar cells embedded in photovoltaic modules," *Scientific Reports*, vol. 4, pp. 4506(1–7), 2014.

[200] M. Paggi, M. Corrado, and M. A. Rodriguez, "A multi-physics and multi-scale numerical approach to microcracking and power-loss in photovoltaic modules," *Composite Structures*, vol. 95, pp. 630–638, 2013.

[201] M. Corrado, A. Infuso, and M. Paggi, "Simulated hail impacts on flexible photovoltaic laminates: testing and modelling," *Meccanica*, vol. 52, no. 6, pp. 1425–1439, 2017.

[202] N. G. Dhere, "Flexible packaging for PV modules," in *Proceedings of the Reliability of Photovoltaic Cells, Modules, Components, and Systems*, vol. 7048, pp. 70480R(1–10), International Society for Optics and Photonics, 2008.

[203] A. Wright and E. J. Lee, "Impact resistant lightweight photovoltaic modules," Nov. 23 2017. Patent number: US 15525513.

[204] M. Aßmus, S. Bergmann, K. Naumenko, and H. Altenbach, "Mechanical behaviour of photovoltaic composite structures: A parameter study on the influence of geometric dimensions and material properties under static loading," *Composites Communications*, vol. 5, pp. 23–26, 2017.

[205] A. M. Gabor, R. Janoch, A. Anselmo, J. L. Lincoln, H. Seigneur, and C. Honeker, "Mechanical load testing of solar panels – beyond certification testing," in *Proceedings of the 44th IEEE Photovoltaic Specialists Conference*, pp. 1–6, Washington, USA, 2017.

[206] E. H. Amalu, D. J. Hughes, F. Nabhani, and J. Winter, "Thermo-mechanical deformation degradation of crystalline silicon photovoltaic (c-Si PV) module in operation," *Engineering Failure Analysis*, vol. 84, pp. 229–246, 2018.

[207] M. Sander, S. Dietrich, M. Pander, M. Ebert, and J. Bagdahn, "Systematic investigation of cracks in encapsulated solar cells after mechanical loading," *Solar Energy Materials and Solar Cells*, vol. 111, pp. 82–89, 2013.

[208] M. Anghileri, L.-M. Castelletti, F. Invernizzi, and M. Mascheroni, "A survey of numerical models for hail impact analysis using explicit finite element codes," *International Journal of Impact Engineering*, vol. 31, no. 8, pp. 929–944, 2005.

[209] G. Mathiak, J. Sommer, W. Herrmann, N. Bogdanski, J. Althaus, and F. Reil, "PV module damages caused by hail impact and non-uniform snow load," in *Proceedings of the 32nd European Photovoltaic Solar Energy Conference and Exhibition*, pp. 1692–1696, Munich, Germany, 2016.

[210] D. Moore, A. Wilson, and R. Ross, "Simulated hail impact testing of photovoltaic solar panels," in *Combined Environments: Technology Interrelations*, pp. 419–430, 1978.

[211] M. Brown, M. W. Rowell, S. J. Coughlin, and W. H. Duncan, "Hail impact testing on crystalline silicon modules with flexible packaging," in *Proceedings of the Photovoltaic Module Reliability Workshop*, Colorado, USA, 2013.

[212] S. Abrate, "Modeling of impacts on composite structures," *Composite structures*, vol. 51, no. 2, pp. 129–138, 2001.

[213] T.-W. Shyr and Y.-H. Pan, "Impact resistance and damage characteristics of composite laminates," *Composite structures*, vol. 62, no. 2, pp. 193–203, 2003.

[214] I. Ivañez and S. Sanchez-Saez, "Numerical modelling of the low-velocity impact response of composite sandwich beams with honeycomb core," *Composite Structures*, vol. 106, pp. 716–723, 2013.

[215] K. Pankhardt, "Temperature dependent flexural stiffness of load bearing laminated glass panes," *Periodica Polytechnica Civil Engineering*, vol. 54, no. 2, pp. 117–126, 2010.

[216] G. Oreski and G. M. Wallner, "Damp heat induced physical aging of PV encapsulation materials," in *Proocesings of the 12th IEEE Intersociety Conference on Thermal and Thermomechanical Phenomena in Electronic Systems*, pp. 1–6, Nevada, USA, 2010.

[217] A. M. Gabor, R. Janoch, A. Anselmo, and H. Field, "Solar panel design factors to reduce the impact of cracked cells and the tendency for crack propagation," in *Proceedings of the NREL PV Module Reliability Workshop*, pp. 1–11, 2015. Colorado, USA.

[218] DIN 18008, "Gas im bauwesen – bemessungs- und konstruktionsgeln. (glass for buildings: design and construction rules)," *Deutsches Institut für Normung e.V.*, 2016.

[219] F. Schwarzl and A. Staverman, "Time-temperature dependence of linear viscoelastic behavior," *Journal of Applied Physics*, vol. 23, no. 8, pp. 838–843, 1952.

[220] C. Schittich, W. Lang, and R. Krippner, *Building skins.* Walter de Gruyter, 2006.

[221] C. P. Lopez, F. Frontini, P. Bonomo, and A. Scognamiglio, "PV and façade systems for the building skin. Analysis of design effectiveness and technological features," in *Proceedings of the 29th European Photovoltaic Solar Energy Conference and Exhibition*, pp. 22–25, Amsterdam, The Netherlands, 2014.

[222] M. Machado, S. Challet, I. Weiss, E. Román, J. M. Espeche, F. Noris, T. Reijenga, E. Rico, I. Huerta, Y. Assoa, F. Burgun, J. Esteban, J. Escribano, P. Alamy, and V. Nguyen, "Supporting market uptake of building-integrated photovoltaic technologies with the pvsites project," in *Proceedings of the 33rd European Photovoltaic Solar Energy Conference and Exhibition*, pp. 2882 – 2887, 2017.

[223] ISO 12543-4:2011, "Glass in building – laminated glass and laminated safety glass – part 2: Laminated safety glass," *International Organization for Standardization*, 2011.

[224] IEC/TS 62788-7-2:2017, "Measurement procedures for materials used in photovoltaic modules - part 7-2: Environmental exposures - accelerated weathering tests of polymeric materials," *International Electrotechnical Commission, TC 82 - Solar photovoltaic energy systems*, 2017.

[225] J. H. Wohlgemuth, M. D. Kempe, and D. C. Miller, "Discoloration of PV encapsulants," in *Proceedings of the 39th IEEE Photovoltaic Specialists Conference*, pp. 3260–3265, Florida, USA, 2013.

[226] C. G. Reid, J. G. Bokria, and J. T. Woods, "UV aging and outdoor exposure correlation for EVA PV encapsulants," in *Processings of the Reliability of Photovoltaic Cells, Modules, Components and Systems VI Conference*, vol. 8825, pp. 882508(1–11), International Society for Optics and Photonics, 2013.

[227] J. Escarré, H.-Y. Li, L. Sansonnens, F. Galliano, G. Cattaneo, P. Heinstein, S. Nicolay, J. Bailat, S. Eberhard, C. Ballif, *et al.*, "When PV modules are becoming real building elements: White solar module, a revolution for BIPV," in *Proceedings of the 42nd IEEE Photovoltaic Specialists Conference*, pp. 1–2, New Orleans, USA, 2015.

[228] C. Pascual, J. De Castro, A. Schueler, and T. Keller, "Integration of dye solar cells in load-bearing translucent glass fiber-reinforced polymer laminates," *Journal of Composite Materials*, vol. 51, no. 7, pp. 939–953, 2017.

[229] C. Pascual Agullo, "Translucent load-bearing GFRP envelopes for daylighting and solar cell integration in building construction," *PhD thesis, Ecole Polythectine Federal de lausanne (EPFL)*, 2014.

[230] C. Pascual, J. De Castro, A. Schueler, A. P. Vassilopoulos, and T. Keller, "Total light transmittance of glass fiber-reinforced polymer laminates for multifunctional load-bearing structures," *Journal of Composite Materials*, vol. 48, no. 29, pp. 3591–3604, 2014.

[231] I. M. Daniel, O. Ishai, I. M. Daniel, and I. Daniel, *Engineering mechanics of composite materials*, vol. 3. Oxford university press New York, 1994.

Acknowledgments

I had the chance to have worked directly with many different persons through my PhD that unconditionally supported me. I would like to start by sincerely thank my thesis director, Prof. Christophe Ballif for having given me the opportunity to realize my PhD thesis at his laboratory and let me discover the photovoltaic world. The passion and enthusiasm you transmitted me for such field have inspired me a lot during these four years. Thank you for the trust you put on me and for stimulating my research efforts with your futuristic ideas. I also have to thank the great opportunities you gave me to travel to conferences and the good memories that resulted. I specially thank Valentin Chapuis who supported me a lot through all these years. Thank you for all the things you taught me, for all your availability to discuss and for the faithful motivation you transferred me during all these years. Your guidance was a key element to the success of this thesis. I thank Dr. Alessandro Virtuani for the support and for all the knowledge of photovoltaic industry you transfer me. Thank you for your supervision and for all your availability to discuss during these last years. I am grateful to have had the chance to work with Dr. Fanny Sculati-Meillaud. I admire the strength, energy and persistence you put at your work. Thank you for the support you gave me and for always be there once I needed.

I would like to thank the president of the jury committee, Prof. Paul Muralt and the jury members, Prof. Thomas Keller, Dr. Gernot Oreski and Dr. Werner Herrmann for kindly accepting to read and evaluate my thesis, for sharing your valuable comments and for honor me with your presence at my private defense. This thesis was only possible thanks to the financial support from the Swiss National Science Foundation (SNSF), the support of the interdisciplinary Active Interfaces team and the assistance of the Doctoral School of Materials Science and Engineering (EDMX).

I have to thank Xavier not only for the incredible support you gave me with all the experimental work but also for all the french (and ski) lessons you provided me during these last years. Thank you for sharing with me your experience, for taking the time to hear me and thank you for being such a nice friend. I especially thank Aïcha for all the support, all your availability to discuss about work or personal issues. I also would like to thank my office mates: Eleonora for all your support and helpful discussions about reliability and complicated modeling equations and Lionel for your precious help during the outdoor temperature monitoring and for all your challenging question to further improve these lightweight modules.

I want to express my gratitude to all the PV-Lab team. A big thanks to all the technical team, Cedric, Aymeric and Joel. Your valuable job make my work go in a very smooth way. I thank Joel

Acknowledgments

Sunier for giving me the first composite fabrication lessons. I also would like to acknowledge Mary-Claude, Karine and Hassan for all the support at the administrative and informatics tasks. I further thank all the students that helped me, Martin, Roman, Arnaud Buxtorf, Alessia, Stefano and Arnaud.

Much of this research would not have been possible without the participation of other laboratories. I would like first to thank all my former colleagues especially Vahid, Sylvain, Gilles and Aida from CCLAB, Amäel and Anouk from LPAC and Nassima and Robin from LMAF. Thank you for the support in testing, availability to discuss and for all the brainstorming lunch time we had at EPFL. I have to thank Dr. Yves Leterrier for all your availability to discuss with me since my first year, for all the feedback and ideas to further improve this work. I also acknowledge the firefighters from Couvet, particularly Bertrand Spiller for his assistance during the fire test performed on the lightweight modules.

I would like to thank all the CSEM-PV Center team, specially Gianluca, Karin, Antonin, Jonathan and Grégory for always being available to discuss results or any equipment related issues, for sharing your knowledge and for always helping me during my journey.

I have to thank the first persons I met when I arrived at EPFL: Raffaele, Ann-Kathrin, Iva and specially Prof. Hofmann. They supported me a lot at the beginning of the PhD and I'm so grateful to had the chance to meet all of you during my time in Lausanne.

The outcome of this thesis would not have been possible without the support of all my friends. I have to especially thank Gizem and Esteban. Thank you for the great moments we spent together, all the international good food we shared, but mainly for always been present all over my journey. Thank you guys, you are the best and I have great memories from our *soirées*. I also would like to thank Camilo, Laurie-Lou (also for trusting my hairdresser skills), Jérémie, Matthias, Johannes, Jan, Jean, Yannick, Josua, Alex and Antonella for all the support and encouragements during my thesis and for all nice moments we spent outside work.

Um grande obrigada a toda a minha família em especial a vocês, Mãe e Pai. Obrigada pelo vosso apoio incondicional e por seguirem-me nesta aventura mesmo estando longe, fazendo-me sentir como se sempre estivessem aqui, ao meu lado. Agradeço também à D. Gracinda & Sr. Manuel (de Portugal) pelo suporte e coragem que me deram durante estes anos. Um obrigada à D. Gracinda & Sr. Manuel (da Suíça), por facilitarem a minha adaptação e por matarem-me as saudades de Portugal, durante todos estes anos, com a fantástica comida portuguesa da D. Gracinda.

My very special and big thank goes to my love, Alexandre. Thank you for the support you gave me during the last four years but, mainly thank you for being on my side for more than 20 years. You shared with me the load during my most difficult moments which pushed me to keep fighting. Thank you for existing in my life.

Neuchâtel, November 2018
Ana C. Martins

Publication list

Updated : 30.11.2018

Publications as first author in peer-reviewed journals

- A. C. Martins, V. Chapuis, A. Virtuani and C. Ballif, "*Robust glass-free lightweight photovoltaic modules with improved resistance to mechanical loads and impact*", accepted for publication in *IEEE J Photovolt*, (2018)

- A. C. Martins, V. Chapuis, H.-Y. Li, L.-E. Perret-Aebi, A. Virtuani and C. Ballif, "*Thermomechanical stability of lightweight glass-free photovoltaic modules based on a composite substrate*", *Sol. Energy Mater Sol. Cells*, **187**, 82 – 90 (2018)

- A. C. Martins, V. Chapuis, F. Sculati-Meillaud, A. Virtuani and C. Ballif, "*Light and durable: composite structures for building integrated photovoltaic modules*", *Prog. Photovolt.*, **26**(9), 718 – 729 (2018)

- A. C. Martins, A. Moreira, A. V. Machado, F. Vaz, C. Fonseca and J. N. Nóbrega "*Developemnt of polymer wicks for the fabrication of bio-medical sensors*", *Mater. Sci. Eng. C* **49**, 356 – 363 (2015)

Patent

- A. C. Martins, V. Chapuis, A. Virtuani and C. Ballif, "*Lightweight solar photovoltaic module*", application submitted (2017)

- C. Fonseca, P. Pedrosa, P. Fiedler, A. C. Martins and J. Haueisen, "*Injectable hydrogel-forming polymer solution for a reliable EEG monitoring and scalp cleaning*", PCT / IB2017 / 056012 (2017)

Publication as co-author in peer-reviewed journals

- P. Pedrosa, P. Fiedler P, L. Schinaia, B. Vasconcelos, A. C. Martins, M. H. Amaral, S. Comani, C. Fonseca, "*Alginate-based hydrogels as an alternative to electrolytic gels for rapid EEG monitoring and easy cleaning procedures*", *Sens. Actuators B*, **247**, 273 – 283 (2017)

- A. R. Mota, L. Duarte, D. Rodrigues, <u>A. C. Martins</u>, A. V. Machado, F. Vaz, P. Fiedler, J. Haueisen, J. N. Nóbrega and C. Fonseca, "*Development of quasi-dry electrode for EEG recording*", *Sens. Actuators A*, **199**, 310 – 317 (2013)

Conference presentations as first author

- <u>A. C. Martins</u>, V. Chapuis, A. Virtuani and C. Ballif, "*Pre-qualification of lightweight modules for building integrated photovoltaics*", Oral presentation, 35th European Photovoltaic Solar Energy Conference and Exhibition, Brussels, Belgium (2018)

- <u>A. C. Martins</u>, V. Chapuis, A. Virtuani and C. Ballif, "*Robust glass-free lightweight photovoltaic modules with improved resistance to mechanical loads and impact*, Oral presentation, 7th World Conference on Photovoltaic Energy Conversion, Hawaii, USA (2018)

- <u>A. C. Martins</u>, V. Chapuis, A. Virtuani and C. Ballif, "*Hail resistance of BIPV composite-based lightweight modules*",Poster presentation, 24th European Photovoltaic Solar Energy Conference and Exhibition, Amsterdam, Netherlands (2017)

- <u>A. C. Martins</u>, V. Chapuis, A. Virtuani, C. Ballif,"*Ultra-Lightweight PV module design for Building Integrated Photovoltaics*", Oral presentation, 44th IEEE Photovoltaic Specialist Conference, Washington, USA, (2017)

- <u>A. C. Martins</u>, J. Sunier, X. Niquille, E. Annigoni, C. Ballif, F. Sculati-Meillaud and A. Virtuani "*New composite structure design for building integrated photovoltaic elements*", Oral presentation, Duracosys - 12th International Conference on Durability of composite systems, Texas, USA, (2016)

Conferences presentations as co-author

- E. Annigoni, <u>A. C. Martins</u>, C. Ballif, and F. Sculati-Meillaud, "*Reliability of PV elements: lifetime and long-term performance prediction*", PV Symposium, Switzerland (2016)

Awards

- Best Student Award at 35th European Photovoltaic Solar Energy Conference and Exhibition during the session on *PV Module Design, Manufacture, Performance and Reliability* (2018)

- 2nd Price award at the Entrepreneurship Training – Business concept given by *Commission for Technology and Innovation* (CTI) (2017)

- Finalist for the 4th Academic-Industrial Training Camp (2017)

CURRICULUM VITAE

ANA CRISTINA MARTINS

E-Mail: ana.martins@epfl.com

Date of birth: **DECEMBER 7TH 1989**

Citizenship: **PORTUGUESE**

EDUCATION

04/2014 – present
SWISS FEDERAL INSTITUTE OF TECHNOLOGY (Lausanne, CH)
Ph.D. in Materials Science and Engineering, thesis:
"Glass-free lightweight PV elements: solutions to minimize weight and maximize durability"

09/2007 – 06/2012
UNIVERSITY OF COIMBRA (Coimbra, PT)
Master studies in Biomedical Engineering (focus on Biomaterials), thesis:
"Development of non-invasive sensors for EEG to use in newborns"

PROFESSIONAL EXPERIENCE

07/2013 – 01/2014
Department
Activity
FACULTY OF ENGINEERING OF THE UNIVERSITY OF PORTO (PORTO, PT)
Department of Metallurgical and Materials Engineering
Designing of the polymer wicks for sensors; functionalization of polymer wicks for hydrophilicity and wicking; surfaces coating; quality tests to evaluate reliability of products; In-vivo tests

07/2012 – 08/2013
Department
Activity
UNIVERSITY OF MINHO (Guimarães, PT)
Institute for polymers and Composites
Development of biosensor employing the engineering and sciences concepts (electronics, mechanics, materials, chemistry, biology, computer science), as well as several other medical and health based knowledge (human physiology, neuronal communication)

AWARDS
Best Student Award at 35th European PV Solar Energy Conference and Exhibition (2018)
2nd Price Award at the CTI Entrepreneurship Training: Business Concept (2017)
Finalist for the 4th Academic-Industrial Training Camp (2017)

LANGUAGES & COMPUTER SKILLS
Portuguese (native), English (proficient), French (proficient), Spanish (basic)
MS Office; Visual Basic for Applications (Excel); Adobe Acrobat, Illustrator and Photoshop; LaTeX; AutoCAD; SolidWorks; Comsol.

ACTIVITIES & INTERESTS
Enjoy all sports especially hiking, swimming.
Travel, photography, movies, music.